First principles simulations of the structure and incorporation of Point defects in diamond

by Mohammed Khalifa B. Atumi

A thesis submitted to Newcastle University for the degree of Doctor of Philosophy.
January 2014.

Dedicated to

Mum, Dad, My wife and Sons

Declaration

This thesis has not previously been submitted by the candidate for a degree in this or any other university.

M. K. Atumi

January 2014.

Acknowledgements

First of all I would like to thank God for giving me the strength and guidance. My special acknowledgement to the people who helped me while I am completing my PhD study. Jonathan Goss for his regular guidance, motivation, and support. Patrick Briddon for his lectures, motivation and manful development of AIMPRO. To my colleagues and friends in Newcastle University for regular discussion.

Most especial thank to my family (my wife and sons), my father, mother, sisters and brothers for their love and support all the time.

Abstract

Diamond is a radiation hard, a wide band-gap semiconductor, with high intrinsic carrier mobilities and high thermal-conductivity, allowing it to be used in extreme radiation environments, high temperatures and high power electronic devices. Additionally, based upon key defects, diamond has also recently emerged as a candidate material for a range of quantum-based applications including quantum information, single photon sources and high-sensitivity magnetometry. Importantly, the growth of diamond both in bulk and film form, has also radically improved over the past decade, so that use of high-quality diamond in a wide range of application is becoming more viable.

Diamond synthesis, especially in the context of this thesis from the gas phase via chemical vapour deposition, is only partially understood. The defects which are incorporated during synthesis are specific to the growth method, and some key defects exhibit orientational polarisation relative to the growth surface orientation. Both the structure and polarisation of these defects are key witnesses to the growth mechanisms, and therefore developing atomistic structures is a key step towards a more comprehensive growth model.

In this thesis, quantum chemical methods based upon density functional theory are used to determine the structure and incorporation mechanisms for key defect centres. It is crucial that quantum-mechanically based methods are used to provide both sufficient quantitative accuracy and to obtain the electronic properties key to compar-

ison with the relevant experimental data, such as required for electron paramagnetic resonance centres including substitutional and interstitial nitrogen, nitrogen-vacancy and nitrogen-vacancy-hydrogen, and silicon containing centres.

For the interstitial centres, it is shown that the models proposed from interpretation of the experimental data for the WAR9 and WAR10 centres are most probably incorrect, as is that of the WAR2 hydrogen-related centre. In contrast, the structures of the P1 epr centre, as well as the NV, NVH and SiV centres are not in dispute, but by simulating these centres in the upper most layers of (110), (111) and (001) diamond surfaces it is shown here that experimentally observed 100% polarisation of the N-related centres, and partial polarisation of the SiV complex can be explained for the (110) surface. The polarisation of defects can give information about how the defects incorporated during diamond growth, which in turn gives some indication of diamond growth mechanisms.

Contents

List of Figures

List of Tables

Publications and Conferences

List of Publications

1. **M. K. Atumi**, J. P. Goss, P. R. Briddon, F. E. Shrif and M. J. Rayson, Hyperfine interactions at nitrogen interstitial defects in diamond, *J.Phys. – Condens.Matter*, 25, 065802 (2013).

2. **M. K. Atumi**, J. P. Goss, P. R. Briddon and M. J. Rayson, Atomistic modeling of the polarization of nitrogen centers in diamond due to growth surface orientation, *Phys.Rev.B*, 88, 245301 (2013).

3. **M. K. Atumi**, J. P. Goss, P. R. Briddon and M. J. Rayson, Assignment of ^{13}C hyperfine interactions in the P1-centre in diamond, in preparation.

4. **M. K. Atumi**, J. P. Goss, P. R. Briddon and M. J. Rayson, Hyperfine interaction of H-divacancy in diamond, in preparation.

List of Conferences

1. **Postgraduate Research Conference 2011 (PGC-2011)**, 26 - 27 January 2011, School of Electrical, Electronic & Computer Engineering, Newcastle University, Newcastle upon Tyne, UK. **(Poster presentation)**.

2. **Nano TP theory group meeting 2011 (NanoTP WG4)**, 13 - 15 June 2011, University of Strathclyde, Glasgow, UK. **(Poster presentation)**.

3. **Annual Research Conference 2012 (ARC-2012)**, 25 - 26 January 2012, School of Electrical & Electronic Engineering, Newcastle University, Newcastle upon Tyne, UK. **(Oral presentation)**.

4. Diamond Conference 2012, 9 - 12 July, University of Warwick, Warwick, UK.

5. **Annual Research Conference 2013 (ARC-2013)**, 21 - 22 January 2013, School of Electrical & Electronic Engineering, Newcastle University, Newcastle upon Tyne, UK. **(Oral presentation)**.

6. **AIMPRO.2013**, 3 - 7 June 2013, University of Surrey, Guildford, UK. **(Poster presentation)**.

7. Diamond Conference 2013, 8 - 11 July, University of Warwick, Warwick, UK.

Chapter 1

Introduction

1.1 Properties and applications of diamond

Diamond crystal is made up of carbon atoms and it has a face-centred cubic (FCC) lattice as shown in figure 1.1, with a basis of two atoms at (0 0 0) and $(\frac{1}{4}\ \frac{1}{4}\ \frac{1}{4})$. The lattice constant of conventional unit cell which contains eight C atoms is $a_0 = 3.567\,\text{Å}$ [166], with atomic density $(8/a^3)$ which is equal to 1.76×10^{23} atom/cm^3.

All the extreme properties of diamond come from the fact that the carbon atoms are light and small relatively and they bind together with short range bonds about (1.54 Å) and the C−C−C bond angles are 109.47° forming very strong covalent bonds. These relatively short C−C bonds allow the orbitals on adjacent C atoms to overlap causing a large energy separation between the occupied bonding orbitals and the unoccupied anti-bonding orbitals which in turn gives rise to a large band gap between the valence and conduction band states in the electronic structure of bulk diamond. The indirect band gap of diamond is about 5.47 eV at 300 K [166], which is very large comparing with 1.12 and 0.66 eV for the more conventional group-IV semiconductors silicon and germanium, respectively. Diamond with this wide band gap is transparent over a range from ultraviolet to infrared which makes diamond suitable for use in optical applications such as infrared laser windows. Diamond can vibrate at unusually high frequency because the atoms in diamond are both light and strongly bonded

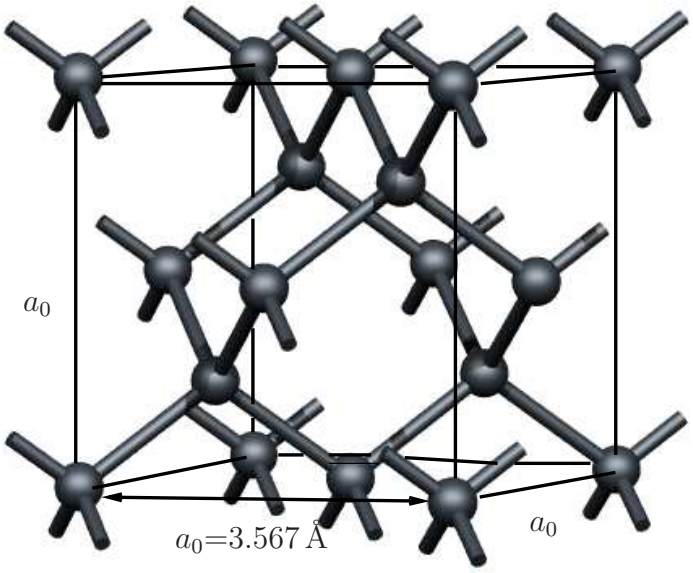

Figure 1.1: Diagram of the conventional unit cell of diamond, where a_0 is the cubic lattice parameter.

where the maximum frequency is about 40×10^{12} Hz compared with 16×10^{12} Hz of silicon. This gives rise to fast heat conduction of diamond even faster than in metals where the thermal conductivity of natural diamond has been measured to be between 900-2300 $\mathrm{Wm^{-1}\,K^{-1}}$ at 300 K and that means it is two to six times higher than of metallic copper which about 400 $\mathrm{Wm^{-1}\,K^{-1}}$ [116,180]. In addition to above properties diamond is the hardest natural material known to man, it has high intrinsic carrier mobility and large breakdown field [25], which makes diamond an interesting material for many potential applications. Also, when diamonds properties are combined, they may provide solutions that can shift performance of optical, electrical and mechanical applications to higher levels.

Due to the wide band gap 5.7 eV with large breakdown field $2 \times 10^7 V cm^{-1}$ and high

electron (hole) mobility 2400 (2100) $cm^2V^{-1}s^{-1}$, diamond is a promising material for high- power and high-frequency electronic applications such high temperature diodes, transistors that works in the microwave range, thermistors and radiation detectors [6, 17]. In addition, when the optical properties of diamond combined with thermal properties, they give a number of optical applications such as CVD diamond beam exit windows in CO_2 lasers [63]. Also, when the wear resistance is combined with high transmittance, they allow diamond to use in coating on wear-resistant windows [126], UV mirrors [131], optical transmission windows [184] and waveguides [83].

Experiments and calculations of H-terminated diamond show that the vacuum level is located below the conduction band [82, 161], i.e. such material exhibits a negative electron affinity, which allows in principle for the emission of electrons from the diamond surface to the vacuum by applying low electric fields. Due to this property, diamond may potentially be used for cold cathodes and field-emitter displays [101].

1.2 Classification of Diamond

Diamond is divided according to the concentration and type of nitrogen impurities into type-I and type-II diamonds. Type-I diamonds have sufficient concentration of nitrogen that can be detected using infra-red absorption spectroscopy, and represent the great majority of all natural diamonds. Type-II diamond does not contain significant quantities that it is not easy to detect by infrared or ultraviolet absorption measurements. Also, these two types can be divided as follows:

1. Type I: The diamond in this type contains high concentration of nitrogen atoms and divided into two types:

    - Type Ia:This type contains substitutional nitrogen impurities in an aggregated form. Approximately 98% of natural diamonds are this type. Again this type is divided into two groups :
        - ⋄ Type IaA: The nitrogen atoms are in nearest-neighbour substitutional (in A-centre form which is two substitutional nitrogen atom

adjacent each other) within the carbon lattice.

- ◇ Type IaB: This type contains also aggregated nitrogen atoms in B-centre form which is made up of vacancy surrounded by four nitrogen atoms.

- Type Ib: This type contains nitrogen as isolated substitutional impurities which are sometimes labelled C-centre. high pressure high temperature (HPHT) and chemical vapour deposition (CVD) diamonds can be counted in this type and natural diamond contains less than 0.1% of this type.

2. Type II: This type contains a very few nitrogen atoms which are undetectable and it is divided in to types:

   - Type IIa: This diamond contains no or negligible amounts of impurities ($<$ 1-2 ppm) which can be considered as the purest of the pure and it is usually colourless. 1-2% of diamond belong to this type.
   - Type IIb: There is no nitrogen atoms in this type and contain boron atoms, where Boron is known to be responsible for a blue colouration [141].

1.3 Synthetic Diamond

Although diamond may be viewed in terms of a naturally occurring gem-stone material, it is also possible to grow synthetic diamonds on an industrial scale. Diamond is manufactured via two main techniques: HPHT synthesis which mimics geological conditions, and CVD, a non-equilibrium growth from activated gas-phase species which can be used to grow both thin-film and bulk diamond. Both methods of growing diamond are summarised below.

1.3.1 HPHT diamond

The HPHT synthesis of diamond is a technique that trying to use the same conditions under which natural diamonds are formed in the earth of depths of approximately

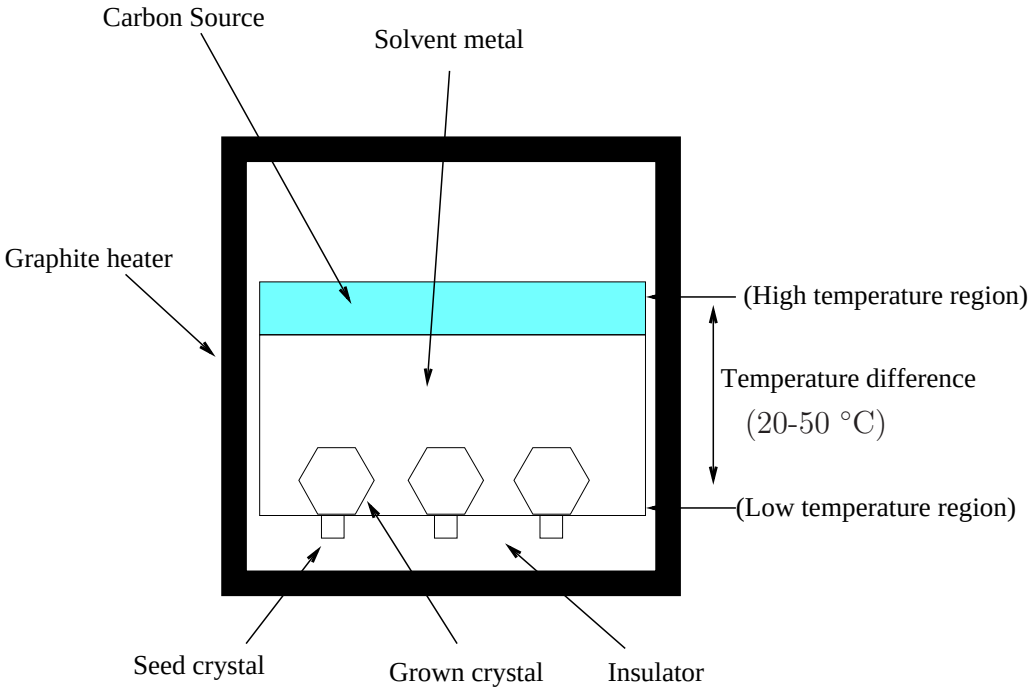

Figure 1.2: Schematic setup of a system for the production of HPHT synthetic.

200 km [157]. The first successful synthesis of diamond using this technique was in 1962 [23]. The synthetic HPHT diamond can be formed by placing an amount of graphite (or glassy carbon [57]), which is the source of carbon, into a large, ceramic, hydraulic press, and at the same time put it under pressures of a few (typically 5-6 GPa) and heat it to a few thousand degrees K (often around 2000 K). To complete the conversion a solvent catalyst such as Fe, Ni, and Co was found to be essential. This technique is the most widely used for diamond synthesis because of relative low cost and it can produce annually amount of diamond by approximately a factor of four comparing to natural diamond, where synthesis a different sizes and qualities of diamond depends on growth conditions (pressure and temperature) and time. Figure 1.2 shows a schematic design for the production of HPHT synthetic diamonds.

1.3.2 CVD diamond

The second method is that the diamond can be deposited on a substrate by chemical vapour deposition which involves a gas-phase chemical reaction occurring above a solid surface causing deposition onto that surface. In contrast to HPHT, this method is working at low pressure (approximately atmospheric pressure) and a temperature between 700-1000°C . Also, many different carbon-containing gas species have been used to create CVD diamond such as methane, aliphatic and aromatic hydrocarbons. In addition, the gas phase usually must contain etchants such as hydrogen (H_2) to prevent the formation of sp^2 bonds. The concentration of molecular hydrogen in gaseous environments during CVD growth is often more than 95% to produce pure diamond. The presence of a gas-phase non-equilibrium is important condition for diamond growth which is generated through gas-phase activation achieved by: external heating as in hot-filament, plasma activation as in plasma assisted, or a combination of chemical and thermal activation as in flame CVD. Creation of single or poly-crystal diamond depends upon the type of substrate where single crystals can be obtained when the substrate is diamond and polycrystalline diamond can be obtained when the silicon, molybdenum or tungsten are used as a substrate. Furthermore, the quality of film depends upon the growth rate and in turn depends upon area, where the quality increases with decreasing growth rate. To create less than $1\,cm^2$ the growth rate is about 1 mm per hour. It is important to note that the concentration of impurities in CVD diamond depends on the impurities in the gases which are used in the CVD growth process, and upon the speed and direction of the diamond growth. Figure 1.3 shows a schematic design for the production of CVD synthetic diamond.

1.4 Defects in diamond

In general, semiconductors and dielectrics may contain many kinds of defects which are introduced during growth and processing, and these defects play a big role in material properties. Incorporation of impurities, vacancies or interstitials, leads to the

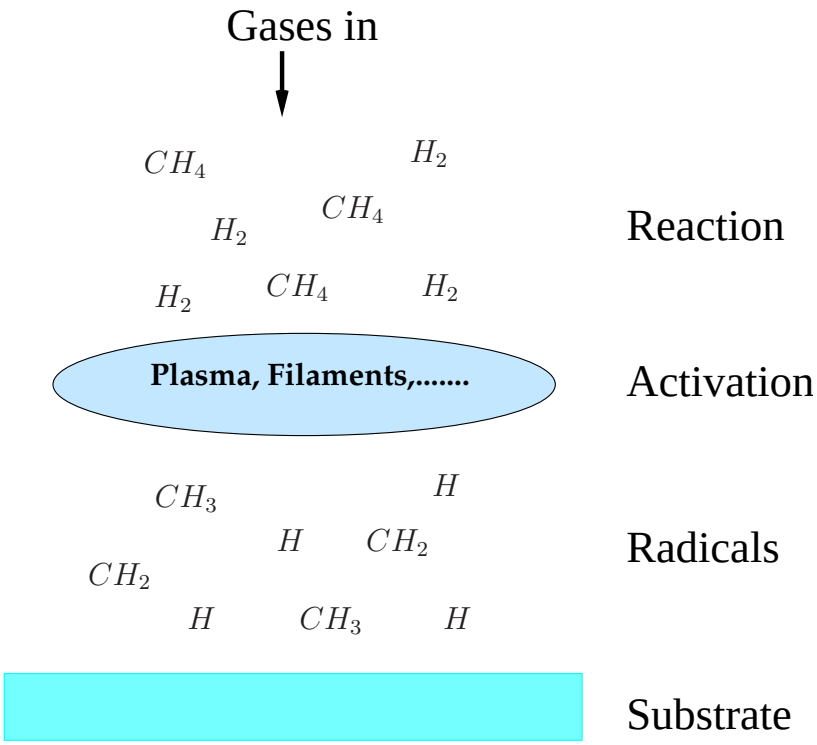

Figure 1.3: Schematic setup of a system for the production of CVD synthetic; the main chemical species are shown.

distortion of the diamond lattice, destroying the local symmetry. In bulk material, the defects can be categorised as point defects (such as impurities or vacancies), extended defects (voids, twins or dislocations) or surface defects (large vacancy disk). Also, point defects can be divided into two groups: intrinsic defects (self-interstitials and vacancies) and impurity-related, with foreign atoms occupying either substitutional and/or interstitial sites.

It is important in the context of this project to note that the concentration of impurities in CVD diamond depends on the impurities in the gases which are used in the CVD growth process, and upon the speed and direction of the diamond growth. In addition, the control of the uptake of impurities, the structures resultant from their incorporation, and the optical and electrical characteristics that they give rise to are key issues in the development of optical and electronic grade diamond materials.

Interestingly, defects are not taken up homogeneously in diamond [161]. At the simplest level, the concentrations in different growth sectors (those growing in different crystallographic directions) can differ by orders of magnitude, with the {111} growth sectors typically being the most defective. For example, experiments showed that the concentration of nitrogen can differ from one sector to another, and the uptake of nitrogen in the {111} sector is higher than {100}, then {113} and {110} sectors.

Even more intriguing is the crystallographic polarisation of the defects that are incorporated. For example, experiment has been shown that the nitrogen-vacancy (N-V) centre in diamond exhibits orientational polarisation, with only the two [111]-orientations with components parallel to the surface normal direction (i.e. pointing out of the (110)-surface) being present. The interpretation is then that it grows in as a unit.

1.5 Thesis Summary

This thesis is divided into three parts, background theory, applications and conclusions including the summary of whole thesis and future work. Each part is subdivided into chapters and a summary of the content of each is provided below, along with general references that might be helpful to the reader.

1.5.1 Part I - Theory and Method

This part is divided into two chapters where the first chapter talks about background theory and AIMPRO modelling package and the second talks about derived quantities

1.5.1.1 Chapter 2 - Fundamental theory

This chapter displays a short discussion about quantum mechanics and the many body problem for solving the Schrödinger equation of complex systems and the approximations that used to solve this equation. This includes the development of methods such as Hartree-Fock to those of density functional theory. In addition, other approxima-

tions used to solve this equation such as pseudo potentials which used to eliminate the need to simulate the core electrons that do not participate in the formation of chemical bonds, and the generalised gradient and the local density approximations for exchange-correlation term in the Hamiltonian of the Schrödinger equation.

This chapter includes also additional approximations regarding the implementation of density functional theory using the ab initio modelling program (AIMPRO) such as basis sets and the treatment of the Brillouin zone, *etc.*

1.5.1.2 Chapter 3 -Derived quantities

This chapter outlines the quantities that can be obtained from the simulations which in turn can be compared either directly or indirectly with experimental observation such as vibrational modes and electrical levels *etc.*

1.5.2 Part II - Application

This part consists of four chapters which include the results of *ab initio* calculations which have been obtained using the modelling package, `AIMPRO`. Also, they include the discussion of these results in the context of experimental observations, and the conclusions.

1.5.2.1 Chapter 4 - Structures of point defects in bulk diamond from EPR

In this chapter the hyperfine interactions of two very known electron paramagnetic resonance centres, which are substitutional nitrogen (P1-centre) and nitrogen-vacancy in bulk diamond are studied in details to investigate their structures and preparing to study their preferential alignment in different diamond surface orientations in next chapters, using `AIMPRO` density functional code.

In addition, this code has been used to to assess the assignments for the structures of WAR9, WAR10 and WAR2 defects in bulk diamond. These defects have been observed recently via electron paramagnetic resonance, where the WAR9 and WAR10

were proposed to be interstitial nitrogen related defects and WAR9 was proposed to be hydrogen-divacancy defect.

1.5.2.2 Chapter 5 - Diamond surfaces

This chapter presents the calculations the structural, properties and energies for clean and hydrogenated-(110), (111) and (001) diamond surfaces, preparing to study the preferential alignment of nitrogen-related and silicon-vacancy defects. These study includes geometry, electronic band structure, absolute surface energy. hydrogen-adsorption and electron affinity of the three surfaces.

1.5.2.3 Chapter 6 - Atomistic modelling of the polarisation of nitrogen centres in diamond due to growth surface orientation

In this chapter quantum mechanical theory has used to investigate the preferential alignment of P1, nitrogen-vacancy nitrogen-vacancy-hydrogen centres on (110), (111) and (001) diamond surfaces. In this study the defects are modelled on and below the three surfaces as a function of depth including multiple defect orientations in each case relative to the surface normal. Also, study the effect of the surface on the band gap states.

1.5.2.4 Chapter 7 - Polarisation of silicon-split defect in diamond

In this chapter quantum mechanical theory has used to study preferential alignment of silicon-split vacancy on and below just (110) diamond surface as a function of depth.

1.5.3 Part III - Conclusions

1.5.3.1 Chapter 8 - Summary

This chapter summarises the studies presented in the thesis.

1.6 Abbreviations

The following abbreviations have been used within this thesis.

Abbreviation	Definition
AIMPRO	*Ab Initio* Modelling PROgram.
DFT	Density Functional Theory.
TFD	Thomas Fermi Dirac model.
TDDFT	Time-Dependent Density Functional Theory.
HF	Hartree-Fock theory.
BZ	Brillouin Zone.
LDF	Local Density Functional.
LDA	Local Density Approximation.
GGA	Generalised Gradient Approximation.
HGH	Hartwigsen-Göedecker-Hutter.
MP	Monkhorst-Pack.
NEB	Nudged Elastic Band.
IP	Ionisation Potential.
EA	Electron Affinity.
HOMO	Highest Occupied Molecular Orbital.
LUMO	Lowest Unoccupied Molecular Orbital.
PL	Photoluminescence.
OA	Optical Absorption.
FFT	Fast Fourier Transformation.
WKB	Wentzel Kramers Brillouin approximation.
SAMs	Self Assembled Monolayers.
MEMS	Micro Electro Mechanical Systems.
STM	Scanning Tunnelling Microscope.

1.7 Notation

The following notations have been used throughout this thesis.

Notation	Definition
E_g^{ks}	Kohn-Sham Energy Gap.
E^{a}	Activation Energy For Forward Migration.
E_{GS}	Ground State Energy.
Q	Charge State.
DB	Dangling Bond.
SAMs	Self Assembled Monolayers.
Si-QD	Silicon Quantum Dot.
D	Si-QD Core Diameter.
E_{kin}	Kinetic Energy.
V_{ext}	External Potential.
E_{xc}	Exchange Correlation Energy.
U_H	Hartree Energy.
V_{eff}	Effective Potential.
T	Temperature.

Part I

Theory and Method

Chapter 2

Fundamental Theory

2.1 The many-body problem

The theoretical study of the electronic properties is one of the principal aim of condensed matter physics and quantum chemistry. The Schrödinger equation is the fundamental and the main task to describe the behaviour of the systems varying from atoms, molecules and nanostructures to more complex bulk systems. The problem is finding the solution of a many-electron system by solving the eigenvalue problem using quantum mechanics where the Schrödinger equation in general is:

$$\hat{H}\Psi = E\Psi, \tag{2.1}$$

where $\hat{H}$ is the many body Hamiltonian and Ψ is the many body wave function. The many-particle Hamiltonian for a system which consisting of N_e electrons in a field due to N_n nuclei may be written as

$$, \hat{H} = -\frac{\hbar^2}{2}\sum_{i}^{N_n}\frac{\nabla^2_{\vec{R}_i}}{M_i} - \sum_{i}^{N_e}\frac{\nabla^2_{\vec{r}_i}}{m_e} - \frac{1}{4\pi\epsilon_0}\sum_{i,j}^{N_n,N_e}\frac{e^2 Z_i}{|\vec{R}_i - \vec{r}_j|} + \frac{1}{8\pi\epsilon_0}\sum_{i\neq j}^{N_e}\frac{e^2}{|\vec{r}_i - \vec{r}_j|} + \frac{1}{8\pi\epsilon_0}\sum_{i\neq j}^{N_n}\frac{e^2 Z_i Z_j}{|\vec{R}_i - \vec{R}_j|} \tag{2.2}$$

where M_i and m_e are the nuclear and electron masses, and R_i and r_i are the positions of nuclei and electrons respectively. e is the electron charge and Z are the atomic

numbers. The first and second terms in the Hamiltonian are the kinetic energies of the nuclei and electrons, respectively. The third term describes the Coulomb interaction between electrons and nuclei, the fourth is the Coulomb interaction of the electron with each other, and the fifth is the Coulombic repulsion between the nuclei. In general, the total wavefunction Ψ in equation 2.1 as a function of the nuclear coordinates R_i, and the position of electron and spin coordinates r_i and S_i, respectively is

$$\Psi = \Psi(r_1, S_1, ..., r_{N_e}, S_{N_e}; R_1, ..., R_{N_n}) \tag{2.3}$$

This system may contain $(N + \sum_i Z_i)$ interacting particles and to describe such a system, the total wavefunction is a function of $4N + 3\sum_i Z_i$ scalar variables. In practice, it is not possible to solve the equations of motion for such a system, so that in order to make progress it is necessary to make some more assumptions and approximations. The first takes care of the relationship between the motion of the electrons and the nuclei.

2.2 The Born-Oppenheimer approximation

Because the nuclei are heavy and move more slowly than electrons, the Born - Oppenheimer approximation assumes that we can freeze the nuclei at fixed positions and the electrons to be in instantaneous equilibrium with them. The system has now $\sum Z_i$ interacting negative particles moving in an external potential of the nuclei and each other. The essential idea of the Born-Oppenheimer (adiabatic) approximation is the motion of nuclei can be separated adiabatically from the motion of electrons. Now the time-independent Hamiltonian for the electrons will take the form:

$$, \hat{H} = -\sum_{i}^{N_e} \frac{\nabla^2_{\vec{r}_i}}{m_e} - \frac{1}{4\pi\epsilon_0} \sum_{i,j}^{N_n,N_e} \frac{e^2 Z_i}{|\vec{R}_i - \vec{r}_j|} + \frac{1}{8\pi\epsilon_0} \sum_{i\neq j}^{N_e} \frac{e^2}{|\vec{r}_i - \vec{r}_j|} \tag{2.4}$$

The electrons and nuclei are considered decoupled with reducing electronic wave function as just a function of positions of electrons and electrons spins and the nuclear

positions fixed then the last equation can be written in simple form

$$, \hat{H} = \hat{T} + \hat{V} + \hat{V}_{\text{ext}} \tag{2.5}$$

where T and V include all relevant kinetic and potential terms from equation 2.2. The information about the nuclei and their positions are given entirely within $\hat{V}_{\text{ext}}$.

However, the solution of the motion of the electrons in the field of the nuclei and each other remains a formidable problem. The most commonly used techniques currently are based upon density functional theory, and this is what is used for the study presented in this thesis.

2.3 Density functional theory

Density functional theory (DFT) is a quantum mechanical theory and it is applied as a tool to solve many body problems by using the electronic charge density as the fundamental variable instead of wave functions. It has been used in computational physics and chemistry calculations to investigate electronic structure for the ground state of many-body systems. Also, the total energy of an electron gas in the presence of a background potential V_{ext} can be calculated. This method is developed by Hohenberg and Kohn [84] later developed by Kohn and Sham [112].

2.3.1 The theorems of Hohenberg and Kohn

The Hamiltonian in equation 2.4 is still impossible and it needs some simplifications to get the solution. One of this simplifications is that the number density of electrons in the material of condensed matter is so high at room temperature which guarantees high degenerated fermions of electrons and the properties related to its electronic structure are mainly determined by the ground state of the electrons. Another simplification known as Hohenberg and Kohn (H-K) theorem which is the first step to modern density functional theory of electrons [84]. Hohenberg-Kohn showed that the density might be used as the basic function uniquely characterising the system in-

stead of the many-body wave function. Also, they proved that the external field V_{ext} is a unique functional of the electron density $n(r)$ within an additive constant. The consequence of H-K is the ground state electron density $n_0(r)$ minimises the energy functional

$$E[n(r)] = F[n(r)] + \int n(r)V_{\text{ext}}(r)d^3r, \tag{2.6}$$

where $F[n(r)]$ is a universal functional, which has the formula;

$$, F[n(r)] = \langle\Psi|\hat{T} + \hat{V}|\Psi\rangle \tag{2.7}$$

$F[n(r)]$ is the same functional for all electronic structure problems and this is the second theorem of H-K.

To prove Hohenberg and Kohn theorem, consider two wave functions Ψ_a and Ψ_b come from different external potentials V_a and V_b but at the same density. The Hamiltonian for two systems and from equation 2.5

$$, \hat{H}_a = \hat{T} + \hat{V} + \hat{V}_a \tag{2.8}$$

$$\hat{H}_b = \hat{T} + \hat{V} + \hat{V}_b \tag{2.9}$$

where $\hat{T}$ and $\hat{V}$ are the kinetic and electron interaction energy operators. From the variational principle the energy for both systems are

$$, E_a = \langle\psi_a|H_a|\psi_a\rangle < \langle\psi_b|H_a|\psi_b\rangle \tag{2.10}$$

and

$$E_b = \langle\psi_b|H_b|\psi_b\rangle < \langle\psi_a|H_b|\psi_a\rangle \tag{2.11}$$

by substituting the equation 2.8 in equation 2.10

$$E_a < \langle\psi_b|\hat{T} + \hat{V} + \hat{V}_a|\psi_b\rangle \tag{2.12}$$

this equation can be written as

$$E_a < \langle\psi_b|\hat{T} + \hat{V} + \hat{V}_b|\psi_b\rangle + \langle\psi_b|\hat{V}_a - \hat{V}_b|\psi_b\rangle \tag{2.13}$$

so

$$E_a < E_b + \langle \psi_b | \hat{V}_a - \hat{V}_b | \psi_b \rangle \tag{2.14}$$

using the same way for E_b

$$E_b < E_a + \langle \psi_a | \hat{V}_b - \hat{V}_a | \psi_a \rangle \tag{2.15}$$

now the universal functional $F[n(r)]$ in equation 2.7 can be used

$$, E_a < E_b + \int n(r)(\hat{V}_a - \hat{V}_b) d^3r, \tag{2.16}$$

$$, E_b < E_a + \int n(r)(\hat{V}_b - \hat{V}_a) d^3r, \tag{2.17}$$

the result of summation of equation 2.16 and 2.17 is

$$E_a + E_b < E_b + E_a \tag{2.18}$$

That means the two systems have different density and V_a is a unique function of the density $n(r)$. However in the equation 2.7, the functional $F[n(r)]$ is not known, and for any practical system, its solution is a significant challenge.

The way forward is an additional approximation, proposed by Kohn and Sham [112].

2.3.2 Kohn-Sham equations

Kohn and Sham postulated that it is possible to deal with an exactly equivalent set of self-consistent one-particle equations instead of the many-electron problem [112]. They suggested that the functional $F[n(r)]$ in equation 2.6 could be written as

$$F[n(r)] = T_s[n(r)] + \frac{e^2}{2} \int \int \frac{n(r)n(r')}{|r - r'|} d^3r d^3r' + E_{XC}[n(r)] \tag{2.19}$$

where $T_s[n(r)]$ is the kinetic energy of non-interacting electrons of the system. The second term is the electron-electron Hartree interaction and the last term is the exchange-correlation energy. From the equations 2.6 and 2.19, the K-S Hamiltonian takes the form

$$\hat{H}_{KS} = \hat{T}_s + \hat{V}_H + \hat{V}_{xc} + \hat{V}_{\text{ext}} \tag{2.20}$$

In terms of a set of particle wavefunctions ψ_i, the electron density $n(r)$ for a non-interacting system of N electrons can be written as

$$n(r) = \sum_{i}^{N} |\psi_i(r)|^2 \tag{2.21}$$

The kinetic energy of non-interacting electrons with density $n(r)$ is

$$T_s[n(r)] = \sum_{i} -\frac{\hbar^2}{2m_e} \int \psi_i^* \nabla^2 \psi_i d^3r \tag{2.22}$$

The functional $F[n(r)]$ shows that the Hartree interaction and the exchange-correlation depend upon the density $n(r)$, which in turn depends upon ψ_i. That means this equation is dealing with a self-consistency problem.

Despite the fact that the K-S equations describe $F[n(r)]$ exactly, the exchange-correlation term is not known in general and further approximation is required. Two common approximations are based upon the exchange-correlation potential for uniform charge densities, termed the local density approximation (LDA), and functionals that take into account the rate of change of charge density in space, termed the generalised gradient approximation (GGA). The GGA is used in this project to investigate WAR9 and WAR10 centres in bulk diamond. Also, it used to model some defects on different diamond surfaces.

2.3.3 The exchange-correlation functional

In principle, density functional theory is exact, but in practice it needs an approximation for the exchange-correlation energy E_{xc}. One approximation is called local density functional theory. The exchange-correlation energy is assumed to be local and can be written by separating the exchange and correlation into two parts

$$E_{XC}[n(r)] = E_X[n(r)] + E_C[n(r)] \tag{2.23}$$

For the case of the homogeneous electron and non-spin polarised system [4], the exchange functional is known as

$$E_X[n] = -\frac{3}{2}\left(\frac{3}{8\pi}\right)^{\frac{1}{3}} n^{\frac{4}{3}} \tag{2.24}$$

For the spin polarised system [176], the exchange functional can be written

$$E_X[n_\uparrow, n_\downarrow] = -\frac{3}{2}\left(\frac{3}{4\pi}\right)^{\frac{1}{3}} [n_\uparrow^{\frac{4}{3}} + n_\downarrow^{\frac{4}{3}}] \tag{2.25}$$

The correlation term $E_C[n(r)]$ is more complicated, but a formula has been developed [137] and it has dealt with this problem numerically. The local density approximation has been found to be very useful in a wide range of solid state systems. This exchange-correlation functional has the formula

$$E_{xc}^{\mathrm{LDA}} = \int n(\vec{r})\epsilon_{xc}(n(\vec{r}))d\vec{r} \tag{2.26}$$

where ϵ_{xc} is the exchange-correlation energy per unit volume of a uniform electron gas. That means the material can be divided into very small volumes with a constant density to find the exchange-correlation energy due to a particular density $n(r)$ and each such volume contributes to the total exchange correlation energy. This method is successful when the charge density is slowly varying for inhomogeneous systems and may give reasonable results when the density changes very quickly.

An alternative method to LDA is the gradient of the density. This method is called the generalised gradient approximation. The GGA involves a first-order expansion of ϵ_{xc} in the density that includes terms in ∇n, and hence carries additional computational expense. Therefore the exchange-correlation contribution of every finite volume is not only dependent upon the local density in that volume, but on the density of volumes around it and equation 2.26 takes the form

$$E_{xc}^{GGA} = \int n(\vec{r})\epsilon_{xc}(n(\vec{r}), \nabla n(\vec{r}))d^3\vec{r} \tag{2.27}$$

In both approximations (GGA and LDA), the band-gap is underestimated. For instance, the band gap has calculated for bulk diamond using GGA to be 4.2 eV and which is underestimated comparing with the experimental value 5.4 eV. In general, The the LDA is more appropriate for the large- scale modelling of solids and the GGA is suitable for accurate studies of molecules.

Next, implementations of DFT via the `AIMPRO` code will be looked at.

2.4 The AIMPRO software package

Modelling techniques are very useful to both explain what is being observed in experiment, and predict the properties of systems of atoms. For this project, calculations are carried out using density functional theory as implemented in the "ab initio modelling program" (AIMPRO) [21, 146].

Throughout the results presented in next chapters, the Perdew, Burke and Ernzerhof (PBE) formulation [136] of the generalised gradient approximation is used to model the exchange-correlation energy, and hence obtain total energies and forces. In this chapter, a brief explanation of some very important additional approximations and practical considerations are presented.

2.4.1 Supercell

The aim of many of the calculations in this project is to determine the properties of a defect in bulk diamond, or at its surface. There are two common methods adopted for such simulations, both of which have advantages and disadvantages. The first method is to assemble a cluster of atoms, along the lines of a giant molecule, such that the core of the system closely resembles the material of interest. The outermost part of the cluster is normally terminated by a chemical such as hydrogen, so that there are no surface states to interfere with any defect buried in the core of the cluster. To minimise the error due to the presence of the surface, the cluster must be made sufficiently large for any defect states to decay to zero before they arrive at the surface.

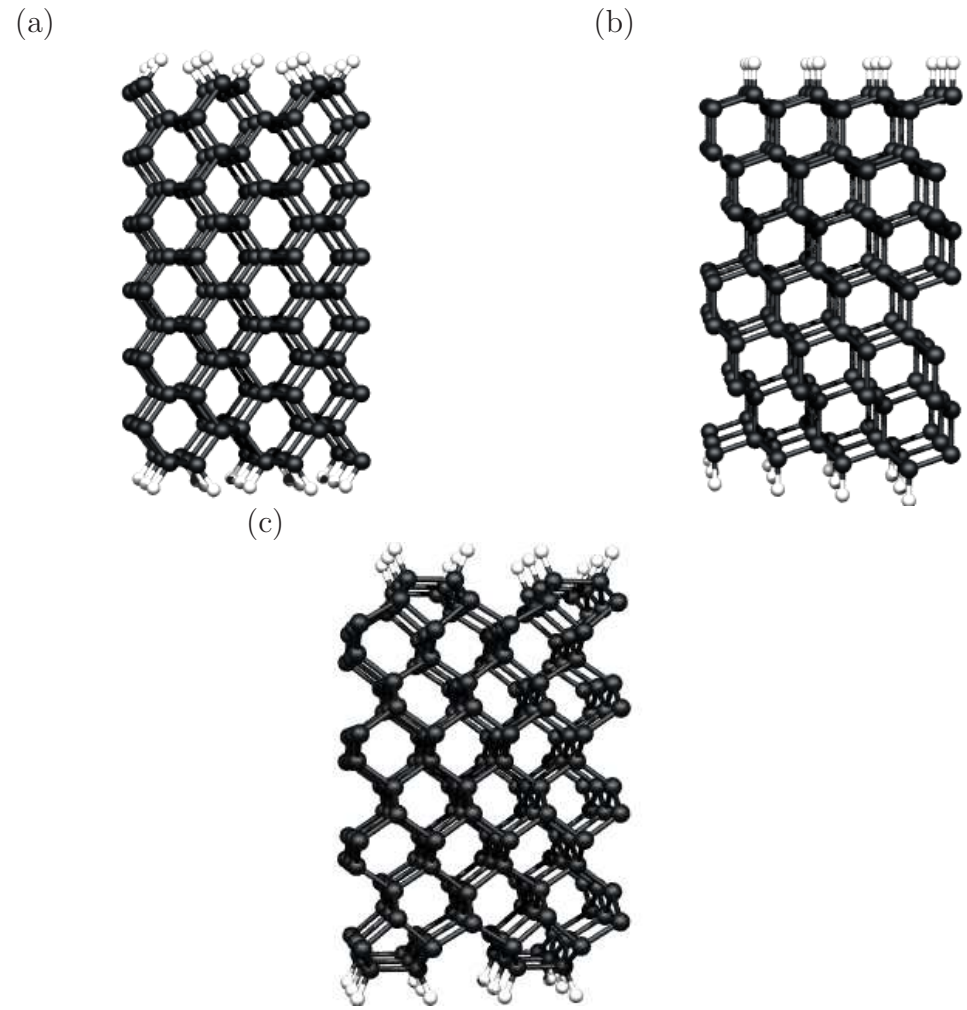

Figure 2.1: Optimised structures of H-terminated supercell slabs for (a) (110), (b) (111) and (c) (001) diamond surfaces.

However, a more common approach is to build a crystal of defects. This is the supercell approach, where in general a non-primitive unit cell of the host material is constructed, and the defect placed inside. The periodic boundary condition then fills the computational universe with an infinite array of defects. An advantage of this approach is that Bloch's theorem is satisfied, and the electronic structure can be obtained in a standard solid-state-physics sense. This has the advantage of no surface, but a disadvantage of defect-defect interactions. Again, the simulation system must be made sufficiently large that these computational artifacts are minimised. Also,

supercells can be used to model surfaces within the method by using the slab method as shown in figure 2.1. In this method, two of supercell directions that parallel to the surface are infinite, but periodic and the third that perpendicular to the surface is finite and the supercell vacuum is created between the repeated images and it is not filled with atoms.

AIMPRO employs both types of approximation, but for the current project the supercell approach has been adopted. As a consequence of using a periodic boundary conditions, the simulation cell can be represented in reciprocal space, so that the Brillouin zone (BZ) of the simulation cell must be accounted for.

2.4.2 Brillouin zone sampling

Since even when one is simulating defects in a solid there remains bulk-like electron states that exhibit dispersion with the electron wave-vector, integration over the reciprocal lattice is required to find the total energy, charge density and other physical quantities of the system that are modelled with a periodic boundary condition.

Let us consider $f(k)$ as a function to be integrated over the BZ, and by construction it must be periodic in reciprocal space. This function has been used in BZ and has an unknown analytical form. In practice one may approximate the analytic integration with a numerical integration over a mesh of points in k-space. For a given BZ with the volume $(2\pi)^3/\Omega$, the average of f is

$$\bar{f} = \frac{\Omega}{(2\pi)^3} \int f(k) dk \tag{2.28}$$

$$\approx \frac{1}{N} \sum_i^N f(k_i) \tag{2.29}$$

Computationally, k is very expensive by increasing the density of the mesh to accurately represent the system.

To avoid such a problem, some alternative schemes have been suggested [12,27] to use a small set of selected special k-points to represent the entire BZ. Alternatively, the method proposed by Monkhorst and Pack (MP) [129,132] which uses an equally

spaced grid of $i \times j \times k$ points, is the method implemented within AIMPRO.

$$k(i,j,k) = v_i a_1 + v_j a_2 + v_k a_3 \tag{2.30}$$

where

$$v_i = (2i - I - 1)/2I, (i = 1, 2, 3, ...I) \tag{2.31}$$

$$v_j = (2j - J - 1)/2J, (i = 1, 2, 3, ...J) \tag{2.32}$$

$$v_k = (2k - K - 1)/2K, (i = 1, 2, 3, ...K) \tag{2.33}$$

where a_1, a_2 and a_3 are the unit vectors of reciprocal space and I, J and $K \geq 1$. Some of the k-points may become equivalent in a supercell that has high symmetry where the sums are performed over the remaining, unique k-points only. For instance, Consider in a cubic system the sampling $4 \times 4 \times 4$ MP grid which contains 64 k-points. From the equations above the k-points $(\frac{1}{8}, \frac{1}{8}, \frac{1}{8})$ and $(\frac{3}{8}, \frac{3}{8}, \frac{3}{8})$ have seven other equivalent points each with all possible sign combinations. The k-points $(\frac{3}{8}, \frac{1}{8}, \frac{1}{8})$ and $(\frac{3}{8}, \frac{3}{8}, \frac{1}{8})$ have 23 other equivalent points each with all possible sign combinations, and interchanging x, y and z. So the calculation should be done with just four k-points and the others then determined by symmetry, but their weights when their charge densities are symmetrised and added should be in the ratio 8:24:24:8 or 1:3:3:1. The effect of sampling on the total energy has been examined for 216 atom supercell containing a substitutional boron and the energy difference between $2 \times 2 \times 2$ and $4 \times 4 \times 4$ is 0.1 meV per atom.

For a surface calculation with the surface for example normal to z-axis, the k-point mesh to lie in the xy-plane and the z-coordinate of all k-points should be one. That means there is no dispersion of the electronic band structure of the slab in z-direction.

2.4.3 Basis sets

A basis set is a mathematical tool expressing one function in terms of a sum of a set of another function type. This is often used where there is not an analytic form of some function, but it can be represented as a sum of other functions which do have an

analytic form. Alternatively one can view the Taylor expansion of, say, a sine function as expressing a sine function using a basis set of functions of the form x^n.

In terms of quantum-mechanical functions, such as electron states and charge densities, the use of basis sets is essential. There are two common kinds of basis sets used in DFT software package: plane waves, because they satisfy Bloch's theorem, and Gaussian type orbitals, because they phenomenologically represent molecular orbitals rather well. The basis set that is used in AIMPRO is Cartesian Gaussian type orbitals for the Kohn-Sham functions and plane-waves to expand the charge density.

Each of the Cartesian Gaussian orbitals are centred at an atomic site R_i and has the form

$$\phi_i(r - R_i) = (x - R_{i,x})^{n_1}(y - R_{i,y})^{n_2}(z - R_{i,z})^{n_3} e^{-\gamma(r-R_i)^2} \tag{2.34}$$

where γ is a constant for each function and $\sum n_i \geq 0$. Different kinds of orbitals can be constructed that look like those found in a hydrogenic atom by selecting different values of n_i. For example, when $\sum n_i = 0$ it means that there is one solution where all n_i is equal to zero and in turn single spherical symmetry orbital is formed to be s-like. When $\sum n_i = 1$, that means there are three solutions where one of the three n_i is equal to 1 while the others are zero and in turn gives rise to three, p-like orbitals. When $\sum n_i = 2$, that means there are six solutions where for three of them, two of n_i equal 1 and the third one is zero, and for the other three solutions, one of n_i is equal to 2 while the others are zero is. By linear combinations of the solutions can give five orbitals that are d-like, and one orbital that is s-like.

One advantage of these sets that they can decay rapidly away from the atom centre and so represent localised orbitals very well, while to perform this with oscillating functions, it needs to combine a huge number of plane waves. In addition, Gaussian orbitals have radial parts of the form $\mathrm{e}^{-\gamma R^2}$ whereas electronic orbitals are proportional to e^{-r} and the benefit of in their use is that, the integrals can be determined analytically and since the product of two Gaussian orbitals is also a Gaussian function, many of the integrals required in the quantum-mechanical equations of motion can be found very efficiently.

For the results presented in this thesis, the Kohn-Sham functions are represented by a basis set where at each carbon atom 13 functions using fixed linear-combinations of s and p orbitals with addition of a set of d functions for polarisation are included, and for the impurities the basis sets are indicated in table 2.1.

Table 2.1: The angular momentum included in the basis sets of the impurities that have uses in these calculations. In each case, p and d indicates the *maximum* orbital angular momentum for a given exponent, and p and d correspond to GTOs with three linear and six quadratic polynomial coefficients, respectively. In the case of the d-GTOs, this includes one of the form $(x^2 + y^2 + z^2)\exp(-\gamma r^2)$, which is strictly an $l = 0$ function. For each case, the angular momentum terms are listed in order of increasing localisation, i.e. increasing γ.

	Nitrogen	Boron	Phosphorus	Silicon	Hydrogen
Basis set	*dddd*	*ddpp*	*dddd*	*dddd*	*ppp*
Number of functions	40	28	40	40	12

Both lattice constant and bulk modulus of pure bulk diamond have been calculated using the above basis sets by obtaining the total energy as a function of volume and fitting the Burch-Murnighan equation of state. The results were very close to the experiments with 0.2% (an overestimate) [158] and 0.5% (underestimated) respectively, as indicated in table 2.2

2.4.4 Pseudopotential approximation

As mentioned in section 2.1, using a quantum-mechanical method for a system with a large number of particles represents a hard calculation. However, one can reduce the number of particles significantly by the application of a further approximation.

Chemistry is almost entirely determined by the valence electrons of the atoms,

Table 2.2: Comparing both the Bulk modules and Lattice constant with Experiment

	Theory	Experiment
Lattice constant (Å)	3.573	3.567 [85]
Bulk modules (GPa)	440	442 [31]

and the core electrons create a screening potential separating the valence electrons from the nucleus. Noting that they play no significant role in many of the properties of interest, one may remove the core electrons from the explicit quantum-mechanical simulation by the use of pseudo potentials which accurately mimic properties of the valence electrons in the atom, and keeps the core electrons fixed in the atomic states.

The removal of the core electrons from the simulation has a second important advantage. The core electrons are very tightly bound to the nucleus, and have a correspondingly high (negative) energy. The contribution that the core electrons provide to the total energy of a collection of atoms dominates. Therefore, to guarantee that energy differences between, say, two structures containing the same atoms, is accurate, the core electrons must be very accurately modelled.

In addition, since the electron wave functions oscillate rapidly close to the nucleus because they are orthogonal to all other electrons in the atom, the number of basis functions needed to describe the system where the core electrons are included explicitly must be very large.

In AIMPRO, the norm-conserving separable pseudo potentials of Harwigsen, Goedecker and Hutter [77] are used.

Chapter 3

Derived quantities

3.1 Introduction

Once it is possible to calculate the energy (and forces) associated with a collection of nuclei and electrons, the simulations may be used to obtain quantities that can be compared either directly or indirectly with experimental observation. The following sections outline the method for deriving these quantities.

3.2 Structural optimisation

For the properties of a surface or point defect to be relevant, they must be obtained with reference to equilibrium conditions. This means that the structures of interest are most often those which have no net force, and represent a minimised total energy. However, the atoms in a supercell or cluster at the beginning of a simulation are not generally at their optimal positions, i.e. they are not in equilibrium. To obtain an optimal structure, one requires a knowledge and minimisation of the forces on each atom.

This is achieved in practice by applying the conjugate gradient method within *AIMPRO* [142, 143] which is one of several methods that could be employed to find the lowest energy structure and it requires only the forces to be known at any stage.

This defines the direction in which the atoms should be moved to reduce the total energy, and requires a knowledge of the forces. The force on each atom (a) is given analytically by

$$f_{la} = -\frac{\partial E}{\partial R_{la}} \tag{3.1}$$

where R_{la} is the atom position and l is the direction of the force (x, y or z).

Once the direction has been determined, the atoms are displaced along this vector, and the minimum in energy *for this displacement direction* obtained. The conjugate gradient method then requires that the next search direction is conjugate to *all previous search directions*, so in general, with the exception of the first step, this is not in the direction of the forces.

3.3 Diffusion

The method used in this work is the climbing nudged elastic band (NEB) technique, as implemented within *AIMPRO* [79,80]. This method is used to find reaction pathways when both the initial and final structural states are known. This method is based upon finding a saddle point and the minimum energy paths between initial and final structures. It works by linearly interpolating a set of images along the path between known initial and final points and optimising this string of images to determine the minimum-energy route between the initial and final structures. These configurations are connected by spring forces to ensure equal spacing along the reaction path. A modification of the NEB method is used to find the minimum energy path (MEP) and to allow the highest energy image at the saddle point to climb. Only the highest image is optimised with the climbing constraint. It means that different spacing will be created on either side of the saddle point, that happens if the maximum image is very far from the saddle point.

Once a saddle point energy has been found, reaction or migration rates may be derived, or the full barrier may be incorporated in further analysis to include tunnelling processes that may occur in chemical reactions.

3.4 Vibrational modes

The calculation of vibrational modes is an important tool of theoretical simulations to predict experimental observables. Vibrational modes can be obtained using *AIMPRO* and compared with the experiments, such as infrared absorption spectroscopy and Raman scattering. For example, defects can be detected due to associated atomic vibrations if they are infrared or Raman active. A mode is infrared active if there is a change in the dipole during the displacement of the atom, and the Raman is active if there is a change in the polarisability.

The procedure for obtaining the modes is based upon a harmonic approximation. The second derivatives of the total energy with respect to the displacements of pairs of atoms are obtained. These represent the force constants in the harmonic oscillator model.

The matrix of the terms

$$\frac{d^2E/dR_i dR_j}{\sqrt{M_i M_j}}$$

is the dynamical matrix of the system and its eigenvalues are the squares of the oscillator frequencies.

3.5 Formation energy

The formation energy is the difference in energy between the configuration of the particles and their free energies when they are in their reference states. That means the formation energy of particular system Y can be defined as;

$$E^f(Y) = E^{\text{tot}}(Y) - \sum \mu_i, \tag{3.2}$$

where $E^{\text{tot}}(Y)$ is the total energy of the system Y which made up of particles (or atoms) of type j. μ_i is the chemical potential of the atoms species i. To obtain the chemical potential of each atom the reference state must be selected carefully. For example, the diamond or graphite might be the reference state of carbon atom and

the H_2 molecule or isolated hydrogen atom might be the reference state of hydrogen atom.

The equation 3.2 can be used for neutral charge state systems. For positive or negative charged systems, the chemical potential of extra/fewer electrons must be taken into account and the equation 3.2 becomes

$$E^f(Y) = E^{\text{tot}}(Y) - \sum \mu_i + q\mu_e, \tag{3.3}$$

where q is the charge state of the system and μ_e is the electron chemical potential which identical to the Fermi level E_{F} at absolute zero in the ground state. In this equation, the energy of the valence band maximum E_v is often considered to be the zero of the E_{F} and the term $q\mu_e$ can be written as $q(E_v + E_{\text{F}})$.

Due to the periodic nature of the calculations and compensating background charged applies of charged systems in the supercell method, errors arise because of electrostatic and multipole interations [124]. Therefore, another term $\xi(q)$ can be added to the equation 3.3 which is called the correction for the periodic boundary condition.

$$E^f(Y) = E^{\text{tot}}(Y) - \sum \mu_i + q\mu_e + qE_{\text{F}} + \xi(q), \tag{3.4}$$

where in the neutral charge state (q=0), this equation becomes as in 3.2.

3.6 Electrical levels

Defect levels that are introduced in the band gap due to impurities in semiconductors are an important characteristic. There are several methods to calculate the positions these levels (donor and acceptor levels) and here a brief description of two methods are presented: the formation energy method and the marker method.

The first method is comparing the formation energies of system in previous section in different charge states (3.4). The electrical level of a defect corresponds to the electron chemical potential position when two charge states of the defect have the same energy.

The marker method attempts to remove systematic errors by calculation of *relative* donor energies. For example, if the donor level of N in diamond is known, then the donor level of P could be estimated by finding the difference in the formation energy donor levels of the two systems and adding this quantity to the *experimental* donor level of the N (the marker).

In general, to determine the donor (0/+) or acceptor (-/0) of structure level under study, the donor or acceptor level of well known defect is needed as a reference by calculated the difference energy between them where the energy difference (ionisation energy) between the neutral and charged structures under study is

$$\delta E_x(0/+) = E_x(0) - E_x(+) \tag{3.5}$$

where the $E_x(0)$ and $E_x(+)$ are the total energy of the neutral and charged state of the defect, and the ionisation energy of the reference defect (marker) is

$$\delta E_r(0/+) = E_r(0) - E_r(+) \tag{3.6}$$

where the $E_r(0)$ and $E_r(+)$ are the total energy of the neutral and charged state of the reference defect, Then the donor level $(0/+)_x$ can be calculated by

$$(0/+)_x = \delta E_x(0/+) - \delta E_r(0/+) + (0/+)_r \tag{3.7}$$

where $(0/+)_r$ is the donor level of the reference defect (marker).

3.7 Electron affinity

The electron affinity (χ) of the system strictly is defined as;

$$\chi = E(\mp) - E(0) \tag{3.8}$$

where $E(0)$ is the total energy of the system in neutral charge state and $E(\mp)$ is the total energy of the system when the electron added $E(-)$ from, or removed to infinity.

In practice the electron affinity of the system can be defined by

$$\chi = E_{\text{vac}} - E_{\text{c}} \tag{3.9}$$

where E_{vac} is the vacuum energy level and E_{c} is the conduction band minimum. Therefore, when the E_{c} lies below E_{vac} as illustrated in figure 3.1(a) , that means the system possesses positive electron affinity and when the E_{c} lies above E_{vac} as illustrated in figure 3.1(b), the system has negative electron affinity.

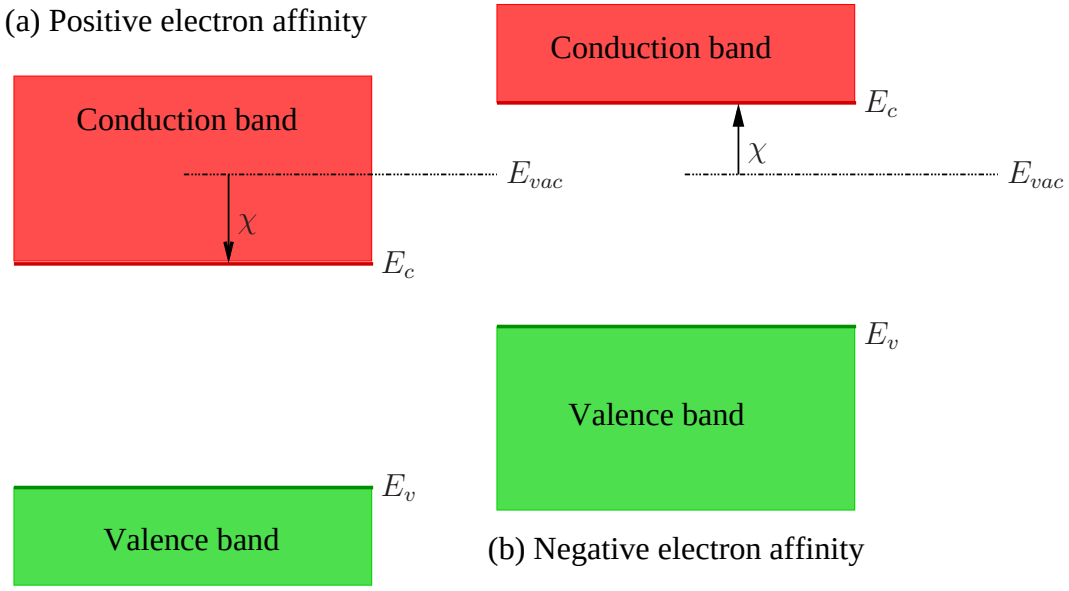

Figure 3.1: Energy level schemes for semiconductor materials with (a) positive and (b) negative electron affinity.

A standard approach has been used to estimate the electron affinity for different diamond surface orientations in the present work [104, 153, 160, 161].

Figure 3.2 shows an example of electron affinity calculation where the electrostatic potential as a function of position in z-direction through the slab into the vacuum, the electrostatic potential variation in bulk diamond, the bulk valance band maximum E_{v} and E_{c} have been plotted. In this calculation the experimental value of the band-gap for diamond (5.47 eV) has been taken into account where E_{c} was located at the experimental value above E_{v}. Then, the electrostatic potential from the bulk diamond, E_{v} and E_{c} are shifted in energy until bulk diamond potential aligns with that found in the middle of the slab system. After that, the electron affinity of the system can be determined from difference between the conduction band minimum and

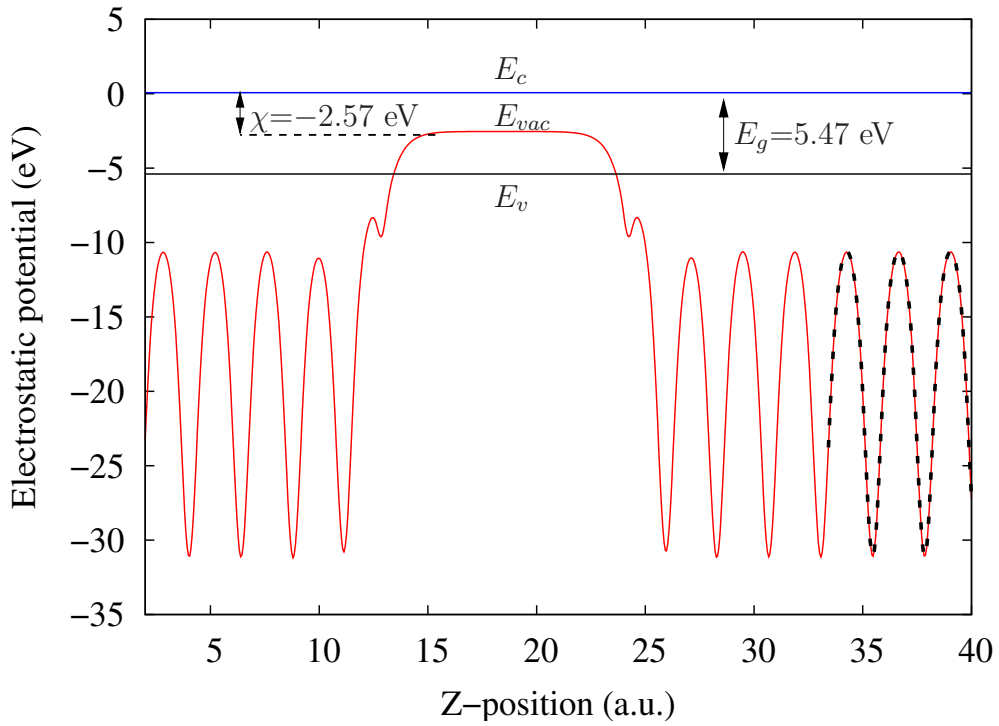

Figure 3.2: An example x, y-averaged electrostatic potentials as a function of z, for (110)-hydrogenated diamond surface (red). The average bulk potential (dashed-black) have been aligned with the electrostatic potentials of the H-terminated surface to place the conduction band minimum (E_c: blue) at zero. E_c is set 5.47 eV above E_v (solid-black) and χ is the electron affinity which is the difference between the vacuum level (E_{vac}) and E_c

.

vacuum level. It is useful to note that in order to refer the bulk energy bands to the vacuum level, the same energy shift can be applied to the electronic band structure found for bulk diamond.

3.8 Electron paramagnetic resonance

Electron paramagnetic resonance (EPR) is a technique for studying chemical species that have one or more unpaired electrons. A lot of centres in semiconductors materials

have been identified using this technique. The electron is negatively charged particle which moves around the nucleus as it possesses orbital angular momentum S and the magnitude of S is

$$\hat{S} = (\frac{h}{2\pi})[S(S+1)]^{\frac{1}{2}} \tag{3.10}$$

where S is the spin quantum number and h is Planck's constant. If the dimension is restricted to one specified direction, usually assigned the z direction, then the spin angular momentum can take the formula

$$S_z = \frac{m_s h}{2\pi} \tag{3.11}$$

where m_s can have $(2S+1)$ different values. The electron spin is associated with magnetic moment μ_e which in turn is proportional to the spin angular momentum where

$$\mu_e = -g_e \mu_B S \tag{3.12}$$

where g_e is called g-factor of electron and μ_B is the Bohr magneton and it is equal to

$$\mu_B = \frac{e\hbar}{2m_e} \tag{3.13}$$

where e is the electron charge, m_e is the electron mass and $\hbar = h/2\pi$. The negative sign in equation (2.12) arises from the fact that the magnetic moment of the electron is collinear but antiparallel to the spin itself. The simple spin Hamiltonian for a free electron in a magnetic field that is defined along the z direction is

$$\hat{H} = g_e \mu_B \hat{S}_z B \tag{3.14}$$

When the defect with unpaired electron (the total spin is not equal to zero) is exposed to the external magnetic field, the spin of unpaired electron may take the same direction ($m_s = 1/2$) of the magnetic field or in the opposite direction ($m_s = -1/2$). This is the Zeeman effect and each direction has a specific energy as shown in figure 3.3. The separation between two levels is proportional to the external magnetic field

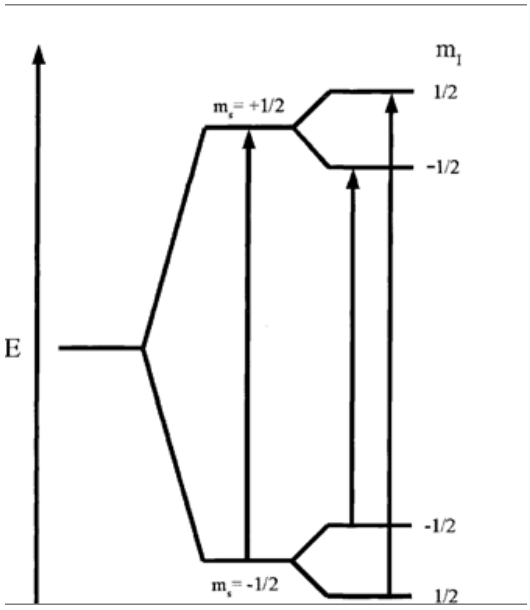

Figure 3.3: Schematic shows energy levels of a system with $S = 1/2$ and $I = 1/2$ in applied magnetic field.

as in the formula

$$\Delta E = -\mu_B g B \tag{3.15}$$

where μ_B is the Bohr magneton, B is the magnetic field and g is called a g-factor and it is related to the electron orbital angular momentum. The electron moves between the two levels due to emitting or absorbing energy which is equal to $h\nu$.

Each carbon atom in perfect diamond has a core electrons and valence electrons with a configuration $(1s^2)2s^2 2p^2$ respectively and the valence electrons are involved in the chemical bond. In the case of $S = 0$, EPR is inactive. When a defect is introduced in the crystal, a level may be created associated with an unpaired electron in the band gap, which makes the structure EPR active, such as substitutional nitrogen, boron and phosphorus in diamond.

Crucially, it is possible to *calculate* some of the spectroscopic quantities obtained in an EPR experiment. Amongst these, the hyperfine interactions arises as a result of interaction between a nuclear magnetic dipole moment (associated with nuclear spin) and an electronic magnetic dipole moment which is associated with the electron spin

density. The hyperfine interaction of the nucleus with spin $I \neq 0$ exists in the region of unpaired electron spin must be considered in the spin Hamiltonian. To explain such a system, consider a simple two-spin system ($S = 1/2$, $I = 1/2$). By applying an external field B, the hyperfine interaction Hamiltonian for this system is given as:

$$\hat{H} = A\hat{I}.\hat{S}, \tag{3.16}$$

where A is the hyperfine tensor which could be isotropic or anisotropic and thier forms can be written as a function of the spin density, respectively:

$$A_{\text{iso}} = \frac{2}{3}\mu_0 g_e \mu_B g_n \mu_n \rho_{\text{spin}}(r) \tag{3.17}$$

and

$$A_{\text{aniso}} = \frac{1}{4\pi}\mu_0 g_e \mu_B g_n \mu_n \int \rho_{\text{spin}}(r)\frac{3\cos^2(\theta) - 1}{2r^3} d^3r \tag{3.18}$$

where r and θ are the electron coordinate and the angle between r and the symmetry axis, respectively. μ_n is the nuclear magneton and ρ is the electron charge densities difference of spin up and spin down which can be calculated by *AIMPRO*. Also, the hyperfine tensor A could be diagonal or axially symmetrical with two components $A_\perp$ and $A_\parallel$, respectively and the hyperfine interaction term in equation 3.16 can take the form

$$H = A_\perp(I_x S_x + I_y S_y) + A_\parallel I_z S_z = (A_{\text{iso}} - A_{\text{aniso}})I.S + 3A_{\text{aniso}} I_z S_z \tag{3.19}$$

where

$$A_\perp = A_{\text{iso}} - A_{\text{aniso}} \tag{3.20}$$

and

$$A_\parallel = A_{\text{iso}} + 2A_{\text{aniso}} \tag{3.21}$$

.

Now by adding this term the Hamiltonian becomes has the form

$$H = g_e \mu_B S_z B + \sum_i S.A_i.I_i \tag{3.22}$$

Since the nuclear spin and its magnetic moment are specific to the chemical species and its isotope, hyperfine interactions are a very useful way to identify the composition of a defect. In addition, since the spectra are generally referenced to crystallographic axes, the *symmetry* of a defect can be obtained, and combining modelling with experiment has proved highly effective in unambiguously identifying the microscopic structure of defects in diamond [8, 41]. In this work, hyperfine interaction has been calculated for very known epr defects such as P1 and nitrogen-vacancy and proposed and alternative models for new epr defects, which have been observed recently, labelled WAR9, WAR10 and WAR2, in diamond in chapter 4.

Part II

Application

Chapter 4

Structures of point defects in bulk diamond from EPR

4.1 Introduction

Incorporation of defects in diamond can affect its electronic, electrical and optical properties. The topic of significant debate is how these defects are incorporated into CVD diamond. Some important defects exist in CVD diamond but there is little information about how they are grown in. In this chapter, two very well known defects which are P1 and N-V centres and three new defects, labelled WAR9, WAR10 and WAR2, are studied to investigate and understand their structures and then for centres whose structures are known to study their polarisation which will be reviewed in the next chapters.

Nitrogen, as a common impurity, is frequently used to classify diamonds [110]. Type-I diamonds have sufficient nitrogen to be detected using infra-red absorption spectroscopy, and is subdivided into type-Ia diamond where the nitrogen is in aggregated forms, and type-Ib diamond where the nitrogen is in the form of isolated substitutional impurities. Type-II diamond is nominally nitrogen free, with type-IIa being essential impurity free material.

The neutral single substitutional nitrogen defect, N_s is observed via epr, referred

to as P1. The P1 centre consists of a nitrogen atom bonded with three nearest-neighbour carbon atoms and an anti-bonding orbital between the nitrogen atom and the fourth carbon neighbour leading to a centre with C_{3v} symmetry. In this defect, the unpaired electron is chiefly localised on the carbon atom and lone pair on nitrogen atom where the distance between nitrogen and carbon is increased to 30% longer than that for an undistorted of C−C bond in diamond [20]. For further corroborating the assignment of P1 to N_s, the hyperfine and quadrupole parameters for ^{14}N and the hyperfine parameters for ^{15}N and ^{13}C have been studied by electron nuclear double resonance (ENDOR). In this work the hyperfine interactions were determined for different carbon neighbours, C1, ..., C7 groups as shown in table 4.1.

N_s is also observed via infrared (IR) absorption spectroscopy, where the defect's spectrum has a maximum at 1130 cm^{-1} and a sharp peak at 1344 cm^{-1} associated with a local vibrational mode [29, 33]. N_s gives rise to a deep donor state in the band gap at about 1.7 eV below the conduction band, which means the the N_s^+ with T_d symmetry can be produced by donating an electron to nearby defect or E_c.

Another form of N-related defect in diamond is the nitrogen-vacancy defect (N-V). N-V in diamond consists of a substitutional nitrogen atom adjacent to a carbon vacancy as shown in figure 4.6. It possesses C_{3v} symmetry. This defect is observed in as grown CVD [103] and HPHT diamond. The N-V defect can also be formed in diamond that has been irradiated to form vacancies. After that when diamond containing nitrogen atom is annealing at about 900 K, the vacancy becomes mobile, and it can be trapped by nitrogen atom to form N-V centres in either the negatively N-V^- or neutral $(N\text{-}V)^0$ charged state depending on the availability of electron donors. Recently, it has been shown that near 100 % of the N-V centres are preferentially oriented along specific direction in CVD diamond grown on (110)-oriented substrates [46], suggesting the defect grows as a unit as will be discussed in chapter 6.

The negative system can be existing in either S=1 or S=0 and S=1/2 for the neutral charge state [74]. $(N\text{-}V)^-$ is of most interest because it has a spin-one ground state [119] with a long spin-coherence time, and diamond can emerge as a candidate

material for a range of quantum-based applications including quantum computing and magnetic field sensing which can be used to detect very small magnetic fields. Since nitrogen atom has five valence electrons, It is believed that the $(N\text{-}V)^-$ is comprised of six electrons, where three of them came from the dangling bonds connecting the vacant site with sp^3 of the three nearest-neighbour carbon atoms, two came from the nitrogen atom and the extra electron might be captured from elsewhere in the crystal.

$(N\text{-}V)$ has been observed in absorption and photoluminescence (PL) with a Zero-phonon line (ZPL) at 2156.2 meV (575 nm) associated with $(N\text{-}V)^0$, arising from the transition between the E ground state and an A excited state of a centre. Also, it has been observed, the ZPL at 1945 meV (637.5 nm) associated with $(\text{V-N})^-$ due to the transition between $^3A_2$ to ^3E of a centre [74, 127].

The neutral charge state of $N\text{-}V$ defect in diamond with $S = -3/2$ has also been observed via EPR [55]. The five electrons of the $(N\text{-}V)^0$ can form $a_{1\text{N}}^2 a_{1\text{C}}^2 e^1$ configuration which gives rise to the many-electron ground state ^2E. By promoting an electron from a singlet $a_{1\text{C}}^2$ to the doublet e^1, the configuration becomes $a_{1\text{N}}^2 a_{1\text{C}}^1 e^2$ and the many-electron states $^2A_1$, $^4A_2$ and ^2E. The assignment of the spin of these states to ^2E ground state and $^2A_1$ follows from electronic structure arguments and they were not determined in the uniaxial stress-splitting study of the ZPL. The system with $S = 3/2$ has been assigned to the $^4A_2$ excited state of $(N\text{-}V)^0$ [59] and it is derived from the configuration $a_{1\text{N}}^2 a_{1\text{C}}^1 e^2$.

Exposure to high-energy irradiation, however, is liable to result in displacement of host atoms that in sufficient concentrations will impact the operation of a detector. Displacement of host atoms creates the primary irradiation defects of vacancies (V) and carbon self-interstitials (I). Surprisingly, I are mobile even at very low temperatures [171] under ionising conditions, forming I-aggregates.

Both V and I centres give rise to very specific experimental signatures. The 1.673 eV optical centre, observed in irradiated type-IIa diamond and labelled GR1, is due to the neutral vacancy [37]. The ground state structure for a single I is the [001]-oriented split-interstitial, $I_{[001]}$. This produces optical absorption lines [38] at

1.685 eV and 1.859 eV, and has been assigned [88] to the $S = 1$ electron paramagnetic resonance (epr) centre labelled R2. Under purely thermal processes [177], $I_{[001]}$ anneals out at lower temperatures than V, at around 700 K. Pairs of I are correlated with the $S = 1$ R1-epr centre [172], which anneals out around the same temperature as R2. A centre containing three I also gives rise to an $S = 1$ epr signal [89], labelled O3. Quantum-chemical simulations [73], show that the proposed models from experiment are likely to be correct, but also reveal that the R1-structure is not the most energetically stable form of the di-interstitial aggregate, presumably a consequence of their formation mechanism. Indeed, the most stable form of the di-interstitial is epr and optically inactive, only potentially being visible to experiment via its local vibrational-modes. In addition, theory explains the thermal loss of R2 at around 700 K as corresponding to the migration step that also corresponds to a reorientation, the calculated [73] activation energy of 1.7 eV agreeing well with the value of 1.6 eV obtained experimentally [130].

Hydrogen also is a common impurity in diamond. Incorporation of hydrogen atom in semiconductors such as diamond can affect the electrical properties by neutralising both n-type and p-type dopants or by producing a variety of defects and impurity states. The hydrogen atom in the gas phase during chemical vapour deposition (CVD) growth is the most abundant atom, where the hydrogen can be incorporated during CVD diamond growth when it is not replaced with a carbon atom. The incorporated hydrogen atoms can be combined with carbon dangling bonds to form H-related defects such as H1, H2, VH^- and NV-H defects. The H1, H2 and VH^- defects have been reported in CVD polycrystalline [186] and CVD monocrystalline [62, 94] diamond. Previous studies have been suggested that H1 is assigned to H-vacancy defects in neutral charge state and the same defect for H2 with increasing the distance between carbon dangling bond and hydrogen atom [94, 186].

In this chapter the results of density functional theory presented for the hyperfine interactions of two very well known epr defects, which are P1-centre and N-V centres. The hyperfine interaction of nitrogen and nearest, next, second and third carbon

neighbours for both defects are calculated and they were in agreement with previous studies. The polarisation of theses defects will be studied in chapter 7 to understand their growth mechanisim. In addition, three new defects labelled WAR9, WAR10 and WAR2 are modelled. These defects have observed in CVD diamond recently via epr and models developed from the experimental data. These models have been evaluated and the results are presented in this chapter, where the calculations showed that the proposed models of WAR9, WAR10 and WAR2 were incorrect structures, so the incorporation mechanism of these defects can not be studied.

4.2 Computational method

Generalised-gradient-approximation functional calculations have been performed using the AIMPRO code as discussed in chapter 2 (section 2.4).

Matrix elements of the Hamiltonian are determined using a plane-wave expansion of the density and Kohn-Sham potential [147] with a cutoff of 175 Ha, resulting in convergence of the total energy with respect to the expansion of the charge density to within around 10 meV. Structures are optimised using a conjugate gradients scheme, with the optimised structures having forces on atoms of $< 10^{-3}$ atomic units, and the final structural optimisation step is required to result in a reduction in the total energy of less than 10^{-5} Ha.

For bulk diamond, the computational approach yields an equilibrium lattice parameter and bulk modulus as listed in table 2.2 and they were in accord with experiment. The calculated indirect band-gap of bulk diamond for both functionals, reflecting the well documented underestimate of the band-gap arising from the underpinning methodology, and is consistent with previous calculations [115]. The defects are modelled using supercells with periodic boundary conditions, based upon the conventional unit cell of the diamond structure. Two sizes of cells have been used, being $2\times2\times2$ and $3\times3\times3$ conventional cells containing 64 and 216 host sites, respectively.

The Brillouin zone is sampling using the Monkhorst-Pack scheme [129]. Sampling

has been varied to assess its impact upon the derived properties, and we find that a mesh of $2 \times 2 \times 2$ points yields an adequate level of convergence in terms of structure and derived quantities such the as hyperfine interactions reported in this chapter.

The hyperfine interactions between the unpaired electron and nuclear spins in ^{15}N, ^{14}N, H or ^{13}C in the defects are modelled. Hyperfine interactions are modelled as outlined previously [156]. Briefly, this involves the combination of pseudo-potentials and reconstructed all-electron wave functions in the core region [19, 81]. Reconstruction of the ion cores allows us to calculate the hyperfine tensor elements within a frozen-core all-electron wave function approximation, without the computational difficulties associated with a full all-electron calculation. The reconstruction in the hyperfine calculations in atomic calculations were achieved using a systematic polynomial basis [145]. This approximation has been successful to model and calculate the hyperfine interaction of other defects in diamond, including hydrogen [41,49,156] nitrogen [48,50] and sulfur [8] containing centres. The calculated magnitudes are typically within a few percent for large interactions such as is the case for S in the W31 centre [8], but for hyperfine interactions with an absolute magnitude of the order of MHz, the uncertainty is much larger. For such cases, which includes WAR9-10, order of magnitude agreement is the best that may be achieved. However, even in these cases, the principal directions tend to be reproduced to a much higher accuracy. Throughout the chapter the principal directions are reported in terms of spherical-polar angles defined as follows: θ is the angle from the crystallographic [001] direction and φ is the angle formed between the projection of the direction onto the (001) plane from [100] toward [010].

4.3 Results

4.3.1 Substitutional nitrogen in bulk diamond

The calculations of substitutional N_s^0 show that in equilibrium three bonds to the nearest carbon atoms are formed with the N atom and one bond between the substi-

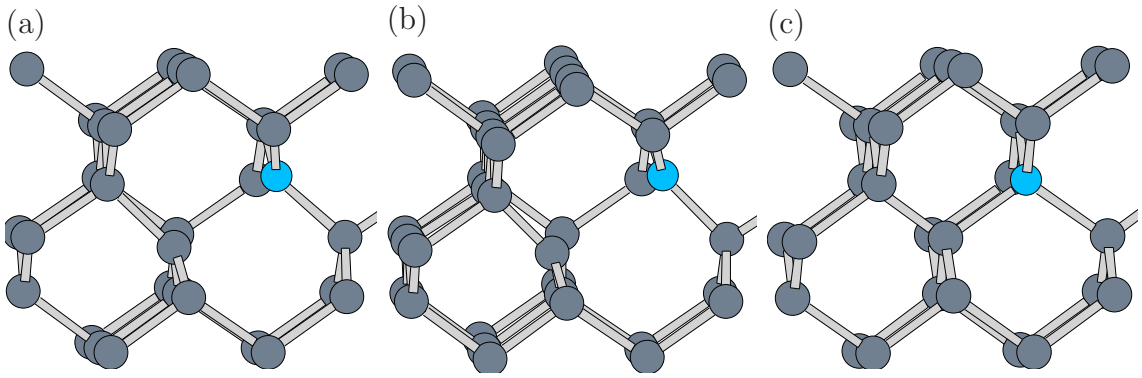

Figure 4.1: Schematic of substitutional nitrogen defects in diamond. Blue and gray atoms are N and C, respectively.(a) the neutral C-centre (N_s^0), (b) negative charge (N_s^-), and (c) positive charge (N_s^+). The horizontal direction is [110] and the vertical direction is [001].

tutional N a neighbouring carbon atom is broken, increasing the distance to 30.8% of the normal C-C distance. The structure is illustrated in figure 4.1(a). This can be understood as a chemical effect. Nitrogen is tri-valent and is therefore chemically satisfied in the equilibrium structure where two electrons occupy a lone-pair orbital aligned along $[1\bar{1}1]$. The more distant carbon neighbour is then in a radical state. This radical carbon forms three σ-bonds with its three carbon neighbours and the fourth bond, an electron occupies a radical p-orbital forming σ^*-bond aligned along [111]. The P1 can be oriented along one of eight $\langle 111 \rangle$ crystallography directions in bulk diamond.

The electronic band-structure is shown in figure 4.2. This shows that this defect creates a partially occupied level in the band gap, localised at around $E_c - 1.6\,\text{eV}$ based upon the formation energies (section 3.6). The calculated value is close to experiment which is 1.7 eV [52].

The centre can be ionised into negative and positive charge states. Both ionised N^- and N^+ forms have been modelled, and their structures are illustrated in figures 4.1(b) and (c), respectively. The ionised C-centre, N^+, is isoelectronic with carbon, and forms four bonds with the nearest-neighbour C atoms. In the N^- form, the carbon radical

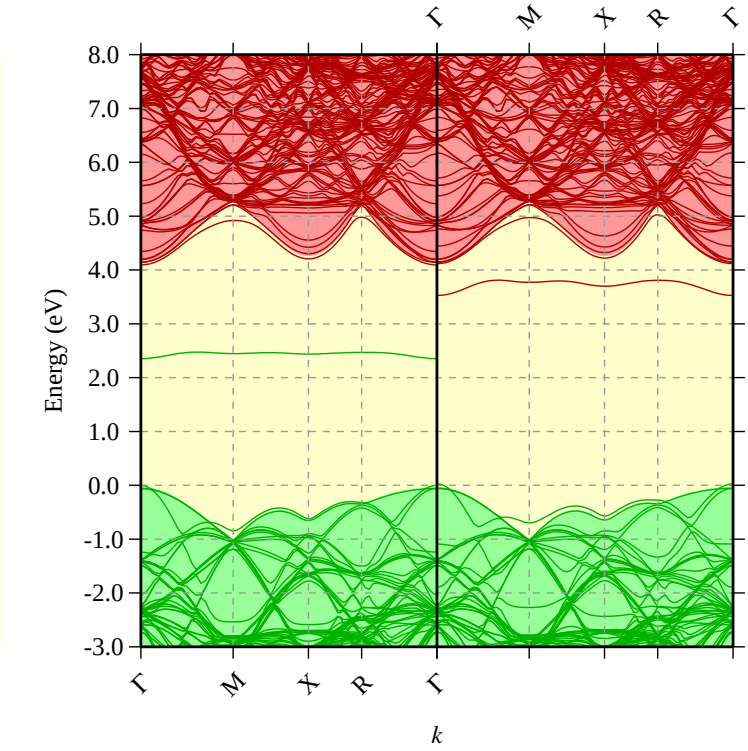

Figure 4.2: The band structure of neutral , S= 1/2 substitutional N in diamond. The left and right panels are spin up and spin down spectra, respectively. Shaded areas and lines represent the band structure of bulk and defective diamond, respectively. The green and red colours show occupied and empty states, respectively. The energy scale has been defined so that the valence band top is at 0 eV. The band-structure is plotted for high symmetry branches of the simple cubic Brillouin zone using the conventional notation.

becomes a lone-pair, and the broken bond is extended further to about 40.4% greater than a host bond.

Figure 4.3 shows the relationship between the chemical potential of the electrons (approximately the Fermi energy) and the formation energy. Where the neutral and positive charge states have the same formation energy defines the donor level, but

in addition, where the neutral and negative charge states have the same formation energy there is an acceptor level in the band-gap. This may be viewed as being a rather surprising result, but there is an evidence that this is seen in experiment [99].

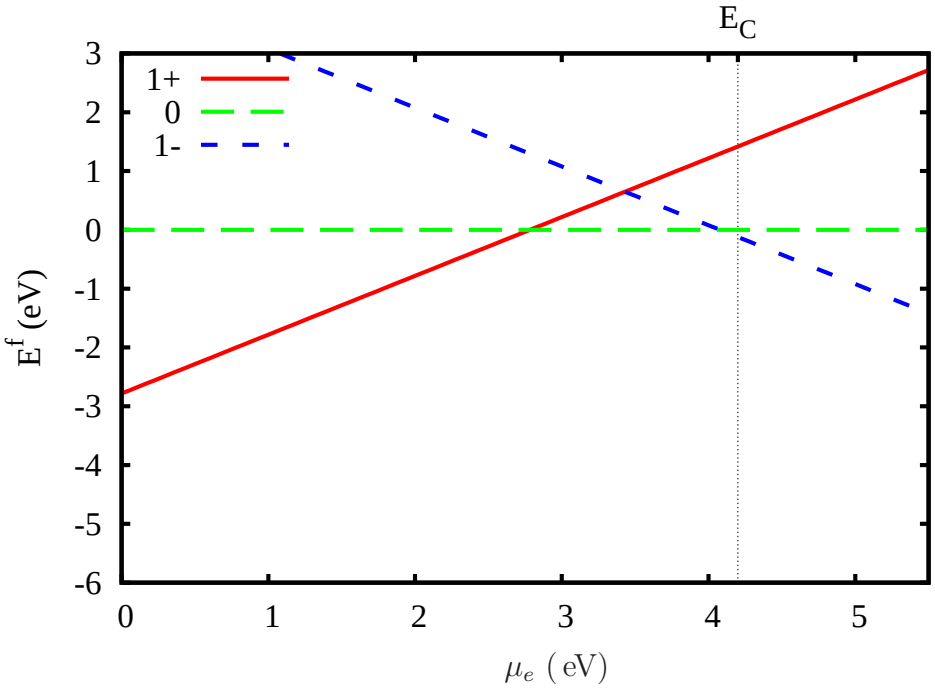

Figure 4.3: Relative formation energy for N_s in three charge states as shown, where the formation energy of the neutral charge state is chosen to be 0 eV. Donor and acceptor levels can be obtained from the critical point where the charge states are in equilibrium with the neutral system.

As mentioned above, substitutional N is also seen in infrared absorption – in this case, this is a process by which the vibrational modes of the defect couple with light. The calculated vibrational modes for the neutral and positively ionised forms are at 1328 cm^{-1} and 1321 cm^{-1} respectively. The results are obtained from modelling the N_s in 64 atom supercell using GGA, sampling $2 \times 2 \times 2$ and the same basis sets that used in the other calculations. As a reference, the calculated frequency for pure diamond is 1315 cm^{-1}. Because the computational method underestimates the elastic constant, the frequencies are expected to be underestimated too. The difference between the

C-centre mode and the bulk mode is 13 cm^{-1}, which is very good agreement with the 11 cm^{-1} difference from experiment.

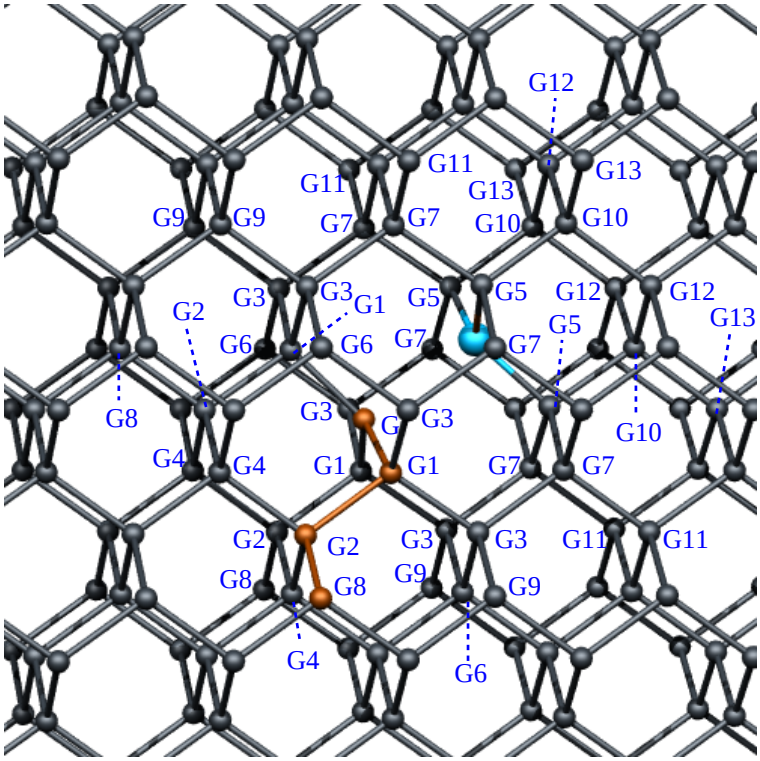

Figure 4.4: Schematics of P1-centre in diamond in the neutral charge state. Labelled sites are indicating the carbon radical G and nearest, next, second and third neighbours (G1, G2,...., G13). The orange in colour path shows the larger hyperfine values of carbon atoms. The colours and axes are as in figure 4.8.

Finally, AIMPRO can be a very useful tool for determining the hyperfine interactions of the defect. It has been used to calculate the hyperfine interaction between the unpaired electron spin and ^{14}N, radical ^{13}C and nearest, second and third neighbours carbon atoms of the defect. The calculated hyperfine parameters for the nitrogen and radical carbon sites were found to be favourably compared with the experiment [34] in terms of values and directions as shown in table 4.1. In the table, the $A \parallel$ is the component of the interaction along the N-C direction, and $A \perp$ is the two components

of the interaction perpendicular to N-C axis. Also, in good agreement is found for a number of distinct carbon sites and the results are given in table 4.1. The results show that the unique carbon atom is strongly coupled to the unpaired electron where most spin density is localised on the unique carbon. The hyperfine interaction between the nitrogen atom and the unpaired electron is less strong than the unique carbon.

The other carbon in nearest, second and third neighbours were also studied, which are labelled as a groups (G1, G2,.....,G13). The results of hyperfine calculations show that, they are weakly coupled to the unpaired electron. Figure 4.5 shows the root mean square (RMS) of the calculated and experimental hyperfine interaction values for ^{13}C sites as a function of distance from the mid point between the nitrogen and unique carbon. In this figure the calculated values are divided into two groups: the first one represents the ^{13}C neighbours to unique carbon (G) and the second ^{13}C neighbours to nitrogen atom. From the present calculations, the principal values of the G1 site is consistent with experimental values of the C_3(c) cite with different sign where the RMS for G1 and C_3(c) (4.5) are 22 and 25 MHz, respectively. The calculation underestimates the hyperfine interaction by around 12 %. Also, the principal directions of the G1 site deviate from N-C axis by 4° which is slightly different with experiment deviation of $-2.3°$ for C_3(c) site. The G2 site possesses the highest values comparing to the other sites, with the RMS value of 32 MHz which in agreement with the value of 34.6 for C_2(d). The calculated value is underestimated by about 9% and in agreement in term of the sign and directions where G1 shows nearly axially symmetric and deviated from [111] direction by 1.26° comparing with the value of 3.9° that obtained from ENDOR measurements.

Table 4.1: Hyperfine tensors (MHz) for ^{14}N and ^{13}C in the P1 centre, as shown in figure 4.4. Experimental data on ^{14}N and ^{13}C are taken from references [15, 34]. Directions of principal values of hyperfine matrices given as [θ,φ], where θ is calculated from [001] crystal axis and φ from [100] axis while rotating about [001]. D_C and D_N are the distance from the radical carbon and nitrogen atoms, respectively.

	Sites	Calculations	(θ, φ)	D_C	D_N		Experiment	(θ, φ)
^{14}N		$A_{\parallel} = 109$	$(55, 45)$	2.02	0.00	^{14}N	114.032	$(54.74, 45.00)$
		$A_{\perp} = 72$					81.318	
G		$A_{\parallel} = 373$	$(55, 45)$	0.00	2.02	C_1(a)	340.8	$(54.74, 45.00)$
		$A_{\perp} = 170$					141.8	
		$A_1 =$-23	$(90, 315)$				26.49	$(90, 315)$
G1	3	$A_2 =$-20	$(59, 45)$	1.48	2.74	C_3(c)	22.77	$(52.36, 45)$
		$A_3 =$-23	$(31, 225)$				25.32	$(37.64, 225)$
		$A_1 = 29$	$(90, 315)$				30.92	$(90, 315)$
G2	3	$A_2 = 38$	$(56, 45)$	2.36	4.14	C_2(d)	40.29	$(58.66, 45)$
		$A_3 = 29$	$(34, 225)$				31.66	$(31.34, 225)$
		$A_1 = 12$	$(68, 30)$				11.76	$(71.5, 33.2)$
G3	6	$A_2 = 8$	$(136, 99)$	2.52	3.08	C_5(g or e)	8.58	$(138.6, 101.0)$
		$A_3 = 8$	$(60, 137)$				8.12	$(55.0, 137.0)$
		$A_1 = 3$	$(90, 315)$					
G4	3	$A_2 = 3$	$(71, 225)$	2.76	4.60			
		$A_3 = 5$	$(19, 45)$					
		$A_1 =$-5	$(90, 315)$				10.64	$(90, 315)$
G5	3	$A_2 =$-2	$(78, 45)$	2.77	1.48	C_4(b)	14.5	$(59.19, 45)$
		$A_3 =$-5	$(12, 225)$				10.62	$(30.81, 225)$
		$A_1 = 4$	$(90, 225)$					
G6	3	$A_2 = 4$	$(60, 135)$	2.92	3.70			
		$A_3 = 6$	$(30, 315)$					

Table 4.1: (Continued)

	Sites	Calculations	(θ, φ)	D_C	D_N		Experiment	(θ, φ)
		$A_1 = 1$	$(50, 249)$				2.7	
G7	6	$A_2 = 1$	$(140, 241)$	3.07	2.51	C_7(e or g)	2.7	
		$A_3 = 3$	$(86, 156)$				2.7	
		$A_1 = 15$	$(58, 45)$				14.5	$(59.19, 45)$
G8	3	$A_2 = 11$	$(32, 225)$	3.75	5.26	C_4	10.62	$(30.81, 225)$
		$A_3 = 11$	$(90, 315)$				10.64	$(90, 315)$
		$A_1 = 0.4$	$(69, 8)$					
G9	6	$A_2 = 0.4$	$(58, 111)$	3.86	4.48			
		$A_3 = 1$	$(39, 250)$					
		$A_1 = 5$	$(68, 45)$				4.1	
G10	3	$A_2 = 3$	$(90, 315)$	4.16	2.38	C_6(f)	4.1	
		$A_3 = 4$	$(22, 45)$				4.1	
		$A_1 =$ -0.2	$(102, 168)$					
G11	6	$A_2 =$ -0.1	$(34, 97)$	4.49	3.86			
		$A_3 = 0.4$	$(59, 250)$					
		$A_1 = 2$	$(45, 180)$					
G12	3	$A_2 = 3$	$(48, 333)$	4.63	2.79			
		$A_3 = 4$	$(76, 76)$					
		$A_1 = 5$	$(28, 45)$					
G13	3	$A_2 = 5$	$(90, 315)$	5.28	3.76			
		$A_3 = 6$	$(62, 225)$					

Interesting results are found from these calculations, where there is disagreement in the hyperfine interactions of G5 site and the experimental values of C_4(b) (*i.e.* G5 in figure 4.4) site. It is expected that the G5 has negative values because the nitrogen atom possesses positive values. Also, the principal values of G5 site are small comparing with C_4(b) where the RMS values of G5 is lowering by 65% because

most of the charge density is localised on the radical carbon atom G and N atom. So, the G5 site can not be assigned to C_4(b) site. The C_4(b) site is axially symmetric and the measurements showed that it is deviated from [111] by 4.5° with negative sign comparing to 22° with positive sign for G5 site.

It is found from our calculation that the hyperfine tensors of G8 site are consistent with C_4(b) site in terms of values, sign and angles. In addition, G8 deviates from [111] by 3.26°, and thus G8 site can be assigned to C_4(b). Also, the path (orange in colour) in figure 4.4 indicates where the larger hyperfine values are calculated suggesting that means the spin density is larger along the path.

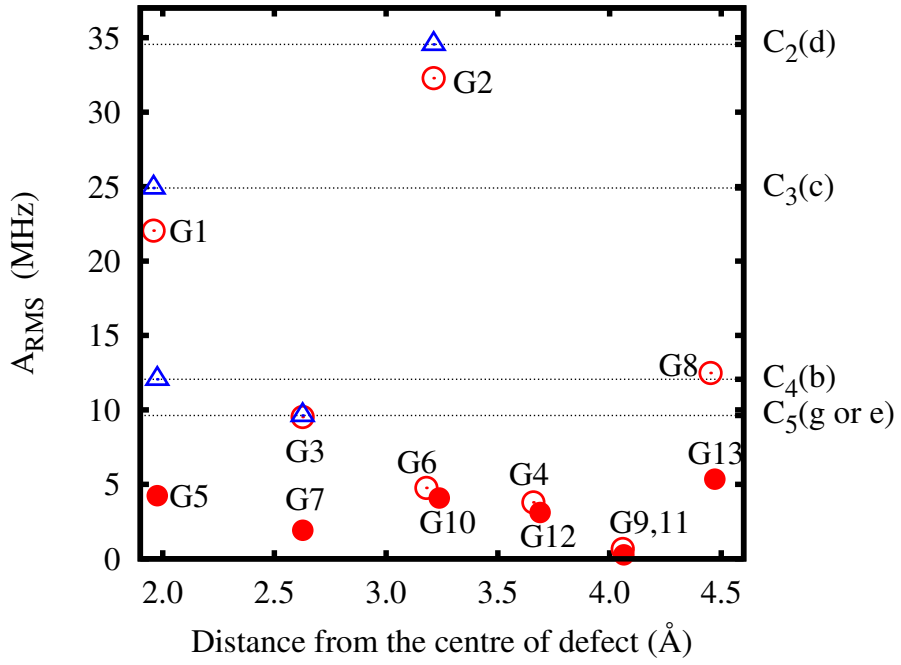

Figure 4.5: The relationship between the root mean square (RMS)of hyperfine tensors for ^{13}C and the distance from the mid of nitrogen and unique carbon. The red circles represent the calculated RMS of ^{13}C neighbours to unique carbon (open circles) and to nitrogen atom (solid circles). The blue triangles represent the RMS of experimental data.

The hyperfine interactions of the other sites are generally small in comparison.

The hyperfine interaction that can be associated with C_7(e or g) (*i.e.* G3 or G7 in figure 4.4) and C_6(f) (*i.e.* G10 in figure 4.4) sites have not been identified by ENDOR but have been observed by EPR. The EPR measurements show that the hyperfine interactions for both sites were very small also with isotropic components and the the location of the C_7 site is unknown. From the present calculations of hyperfine interactions for these sites, the C_7 with RMS value of 2.7 MHz might be assigned to one of G7, G9, G11 or G12 sites with the RMS values between 1 to 3 MHz but with anisotropic components. In addition, the C_6(f) has the RMS value of 4.1 MHz and might be assigned to one of G4, G5, G6, G10 or G13 with RMS values between 4 to 5 MHz but also with anisotropic components. It may be that the experiment group are averaging of several non-equivalent sites.

Based upon this, and other quantitative agreements with experiment [8, 48, 64], this shows one can calculate hyperfine coupling very accurately and hence we can use the calculated values to distinguish between different models for less well-understood centres.

4.3.2 Nitrogen-vacancy in bulk diamond

The neutral N-V centre with $S = 1/2$ and the negatively charged N-V with both $S = 0$ and $S = 1$ in diamond have modelled. To describe the geometry of the negatively charged N-V centre in diamond, the system is optimised until the forces between the atoms become negligible. The optimised structure of $(N\text{-}V)^-$ has trigonal symmetry with $S = 1$. The bond lengths that connect to the nitrogen atom are 1.48 Å and the bond lengths that connect to the radical carbon atom are 1.49 Å, which are in agreement with previous calculations [1, 74]. The calculated distance from the vacant site to the nearest neighbour radical carbon and nitrogen atoms are 1.64 and 1.68 Å, respectively, where the position of the vacancy was determined by calculating the middle point between two atoms that placed on the same axes along [111] direction.

The band structure structure of $(N\text{-}V)^-$ has been calculated. These dangling bonds create an orbital singlet of symmetry a_1 occupied by two electrons an orbital

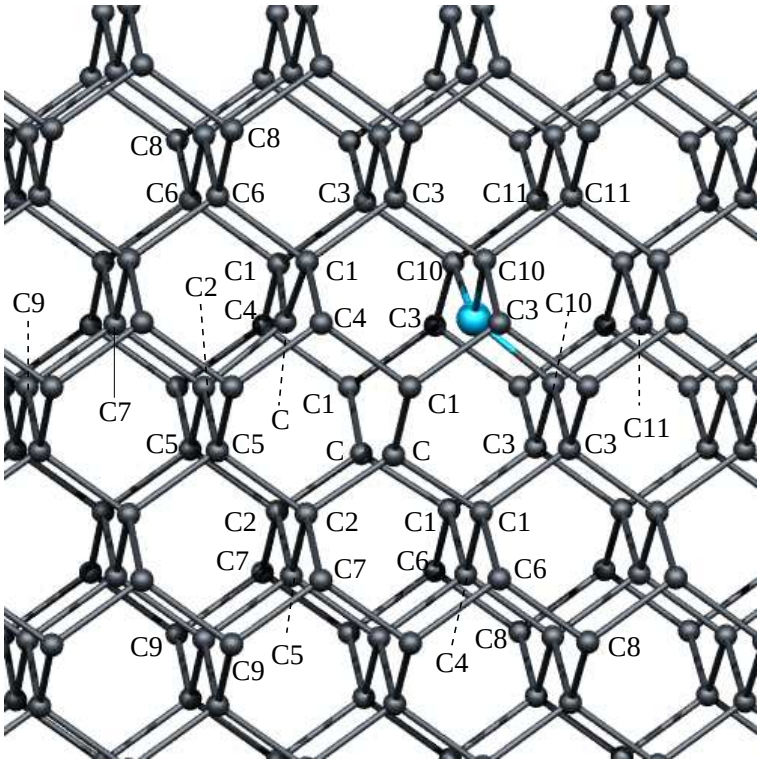

Figure 4.6: Schematics of N-V centre in diamond in the neutral charge state. Labelled sites are indicating the carbon radical C and nearest, next, second and third neighbours (C1, C2,...., C11). The colours and axes are as in figure 4.8.

doublet e_x, e_y occupied by two electrons with parallel spin lying above a_1 as shown in figure 4.7. Another state which is occupied by the remaining two electrons is considered to be deep in the valence band and thus it does not participate in the excitation. The Kohn-Sham energy levels predicted that the $a_1^{\uparrow}$ and $a_1^{\downarrow}$ levels (occupied) to lie 1.16 and 1.99 eV below the $e_{xy}^{\uparrow}$ and $e_{xy}^{\downarrow}$ levels in the band gap.

The hyperfine interactions of nitrogen ^{14}N and ^{13}C carbon atoms at nearest neighbours to the vacancy in $(N\text{-}V)^-$ centre have been calculated as reported in table 4.2. In order to estimate the accuracy of the calculations, it is important to compare the calculated hyperfine values to the known experimental data. The calculations predict that the hyperfine tensors associated with the three radical carbon atoms (C site) have

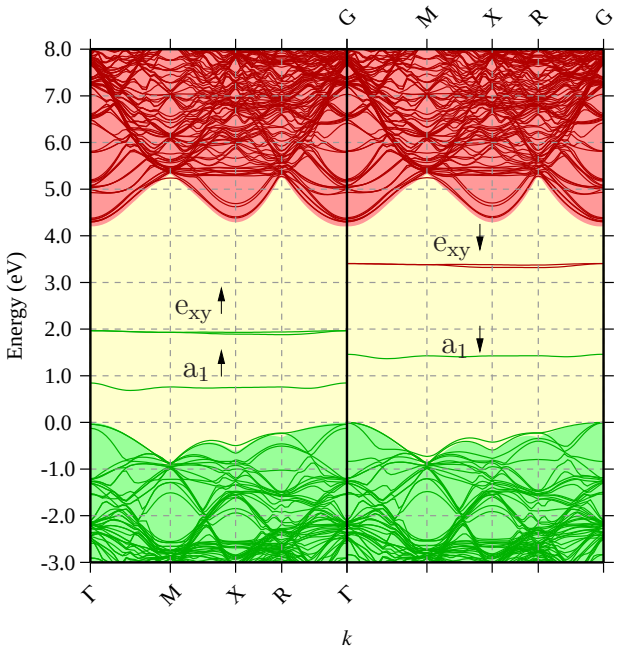

Figure 4.7: The band structure of $(N\text{-}V)^-$ in diamond. The left and right panels are spin up and spin down spectra, respectively. Black lines represent the band structure of bulk diamond. The red and blue colours show occupied and empty states, respectively. The energy scale has been defined so that the valence band top is at 0 eV. The band-structure is plotted for high symmetry branches of the simple cubic Brillouin zone using the conventional notation.

the largest values which is in agreement with previous calculations and the epr measurements.This comes from the fact that most of the spin density is localised on the three radical carbon atoms and in turn came from the spin polarised e level localised on the carbon dangling bonds due to the symmetry. The charge density has been estimated to be 72 % is localised on the radical carbon atoms and 0.2 % on the nitrogen atom. The remain charge density is roughly 28 % which spreads in the lattice [78]. The ^{14}N in $(N\text{-}V)^-$ is weakly coupled to the unpaired electron where the hyperfine tensors are very small with with negative spin density and they are consistent with

the experimental data and previous calculations.

Table 4.2: Hyperfine tensors (MHz) for ^{14}N and ^{13}C in the $(N\text{-}V)^-$ centre, as . shown in figure 4.6. Experimental data is taken from references [54, 78, 119]. Previous theoretical data on both ^{14}N and ^{13}C are taken from [1]

	D_{vac}	Calculations	(θ, φ)	Theory	Experiment	Experiment*
		$A_1 = -2.2$	$(40, 77)$	-1.7	± 2.1	-2.70
N	1.68	$A_2 = -2.2$	$(74, 147)$	-1.7	± 2.1	-2.70
		$A_3 = -1.7$	$(55, 135)$	-1.7	± 2.3	-2.14
		$A_1 = 117.1$	$(36, 45)$	109.5	± 123	
C	1.64	$A_2 = 117.3$	$(90, 45)$	110.2	± 123	
		$A_3 = 200.8$	$(54, 135)$	185.4	± 205	
		$A_1 = -6.7$	$(61, 114)$	-4.8		
C1	2.49	$A_2 = -6.3$	$(55, 178)$	-3.7		
		$A_3 = -3.5$	$(48, 127)$	-1.5		
		$A_1 = -9.7$	$(90, 45)$	-7.4		
C2	2.53	$A_2 = -9.5$	$(6, 45)$	-7.3		
		$A_3 = -7.6$	$(84, 135)$	-5.8		
		$A_1 = 3.0$	$(62, 29)$	2.8		
C3	2.94	$A_2 = 3.2$	$(89, 61)$	3.3		
		$A_3 = 4.9$	$(28, 26)$	4.6		
		$A_1 = 1.6$	$(63, 45)$	1.4		
C4	2.95	$A_2 = 3.2$	$(90, 45)$	2.4		
		$A_3 = 3.2$	$(27, 135)$	2.9		
		$A_1 = 3.3$	$(72, 45)$	3.4		
C5	2.97	$A_2 = 4.9$	$(90, 45)$	4.7		
		$A_3 = 5.2$	$(17, 135)$	4.9		
		$A_1 = 13.1$	$(50, 172)$	13.5		
C6	3.89	$A_2 = 13.2$	$(61, 109)$	14.2		

Table 4.2: (Continued)

	D_{vac}	Calculations	(θ, φ)	Theory	Experiment1	Experiment2
		$A_3 = 19.0$	$(54, 136)$	19.4		
		$A_1 = 11.8$	$(90, 45)$	12.8	± 15.0	
C7	3.91	$A_2 = 12.0$	$(33, 45)$	12.8	± 15.0	
		$A_3 = 17.4$	$(57, 135)$	18	± 15.0	
		$A_1 = 2.5$	$(81, 63)$	2.6		
C8	5.00	$A_2 = 2.6$	$(42, 163)$	2.7		
		$A_3 = 3.8$	$(49, 146)$	3.8		
		$A_1 = 1.2$	$(20, 45)$	1.5		
C9	5.10	$A_2 = 1.3$	$(90, 45)$	1.5		
		$A_3 = 2.2$	$(60, 135)$	2.2		
		$A_1 = -0.2$	$(90, 45)$			
C10	2.53	$A_2 = -0.0$	$(89, 90)$			
		$A_3 = 1.1$	$(89, 135)$			
		$A_1 = -0.1$	$(15, 45)$			
C11	3.92	$A_2 = -0.1$	$(90, 45)$			
		$A_3 = 0.4$	$(47, 111)$			

It has been suggested that the hyperfine constants are approximately proportional to the spin density according to the equation

$$A_{ij}^{(I)} = \frac{1}{2S} \int d^3 r n_S(r) \beta_I \beta_e \hbar^2 \left[\left(\frac{8\pi}{3} \delta(r) \right) + \left(\frac{2x_i x_j}{r^5} - \frac{\delta_{ij}}{r^3} \right) \right], \tag{4.1}$$

where S is the spin state, β_I and β_e are the nuclear and electron Bohr magneton respectively and $n_S(r)$ is the spin density of the spin state. Thus, more than nine sites of carbon nuclei in the second neighbour of the vacancy should have the value of 70 MHz and less than 10 MHz for the more distant carbon atoms [120]. This suggestion is not completely in agreement with the epr data, where, for instance, the hyperfine constants of 15 MHz was observed from the three ^{13}C [119]. The hyperfine

Table 4.3: Hyperfine tensors (MHz) for ^{15}N and ^{13}C in the $(N\text{-}V)^0$ centre, as shown in figure 4.6. Experimental data is taken from references [78,119] and Experimental data on ^{13}C atoms are taken from [119]. Previous theoretical data on both ^{14}N and ^{13}C are taken from [1]

	Calculations	(θ, φ)	Theory	Experiment
	$A_1 = -23$	$(76, 145)$	-23.4	-23.8
^{15}N	$A_2 = -23$	$(39, 106)$	-23.4	-23.8
	$A_3 = -37$	$(55, 45)$	-39.0	-35.7
	$A_1 = 69$	$(35, 45)$	60.6	
^{13}C	$A_2 = 70$	$(90, 45)$	61.0	
	$A_3 = 145$	$(55, 135)$	126.2	

interactions between the unpaired electrons and the ^{13}C at next, second and third neighbours of $(N\text{-}V)^-$ could be important for quantum-based applications. The hyperfine interactions for these sites have been calculated. The hyperfine tensors of six and the three symmetrically equivalent carbon atoms at C6 and C7 sites respectively as shown in figure 4.6 are large compared with the other ^{13}C sites.

The hyperfine tensors of 15 MHz have been measured but it was not shown in detail, where the hyperfine splitting is isotropic. This site has been assigned to the three symmetrically equivalent carbon atoms at third neighbour distance of 3.86 Å [1], which is in agreement with these calculations at C7 site. There is no experimental data from the literature to compare the other calculated ^{13}C hyperfine interactions but these calculations are in accord with previous theoretical results. The hyperfine interactions of nearest and second neighbours to the nitrogen atom, labelled C3, C10 and C11 are calculated in this work as reported in table 4.2. The hyperfine tensors are very small and they are unreported in previous works.

The hyperfine interactions of ^{15}N and ^{13}C in $(N\text{-}V)^0$ are calculated. This defect

has C_{3v} symmetry with S=1/2. The calculations show that the hyperfine interactions between the ^{15}N and the unpaired electron is approximately 10 times than $(N\text{-}V)^-$ and it was in agreement with experiment. That means the spin density localised on the nitrogen atom is small but significant. The hyperfine interactions of the three nearest-neighbour carbon atom are also calculated. A large proportion of spin density is localised on these three carbon atoms, but less than for $(N\text{-}V)^-$ and the hyperfine tensors are in agreement with previous LSDA calculations [59] as reported in table 4.3.

Again AIMPRO can predicts the hyperfine interactions of the defect with good accuracy. The hyperfine interactions have been modelled for $(N\text{-}V)^0$ and $(N\text{-}V)^-$ in bulk diamond and they were in accord with the previous calculations and experimental results. The contribution of the carbon atoms at large distance is important for quantum-bases applications because they have significant hyperfine tensors especially on C6 and C7 groups. These hyperfine tensors could be investigated in detail experimentally.

4.3.3 Interstitial nitrogen defects in bulk diamond

In type-I material, the presence of nitrogen significantly affects the formation of radiation centres. Previous calculations [66] examined the sequence of formation of centres made up from nitrogen combined with I. A key to the understanding of this sequence is in the determination of the structure of the H1a infra-red centre [66, 117], which is a pair of nitrogen atoms in a [001]-split configuration at a host site. The annealing properties for formation of H1a are very important [111]. In type-Ib material H1a forms around 650°C, whereas in type-Ia it occurs around 300°C. In the former case the initial process must involve the formation of a complex of I and substitutional N which becomes mobile and is then trapped at a second substitutional N site in a metastable form prior to re-arrangement into the [001]-split form [66]. The activation energy for the migration of the nitrogen interstitial, $N_{[001]}$, is essentially the same as that of I, calculated [66] at 1.7 eV, consistent with the temperature of formation of pre-cursors to H1a in type-Ib material.

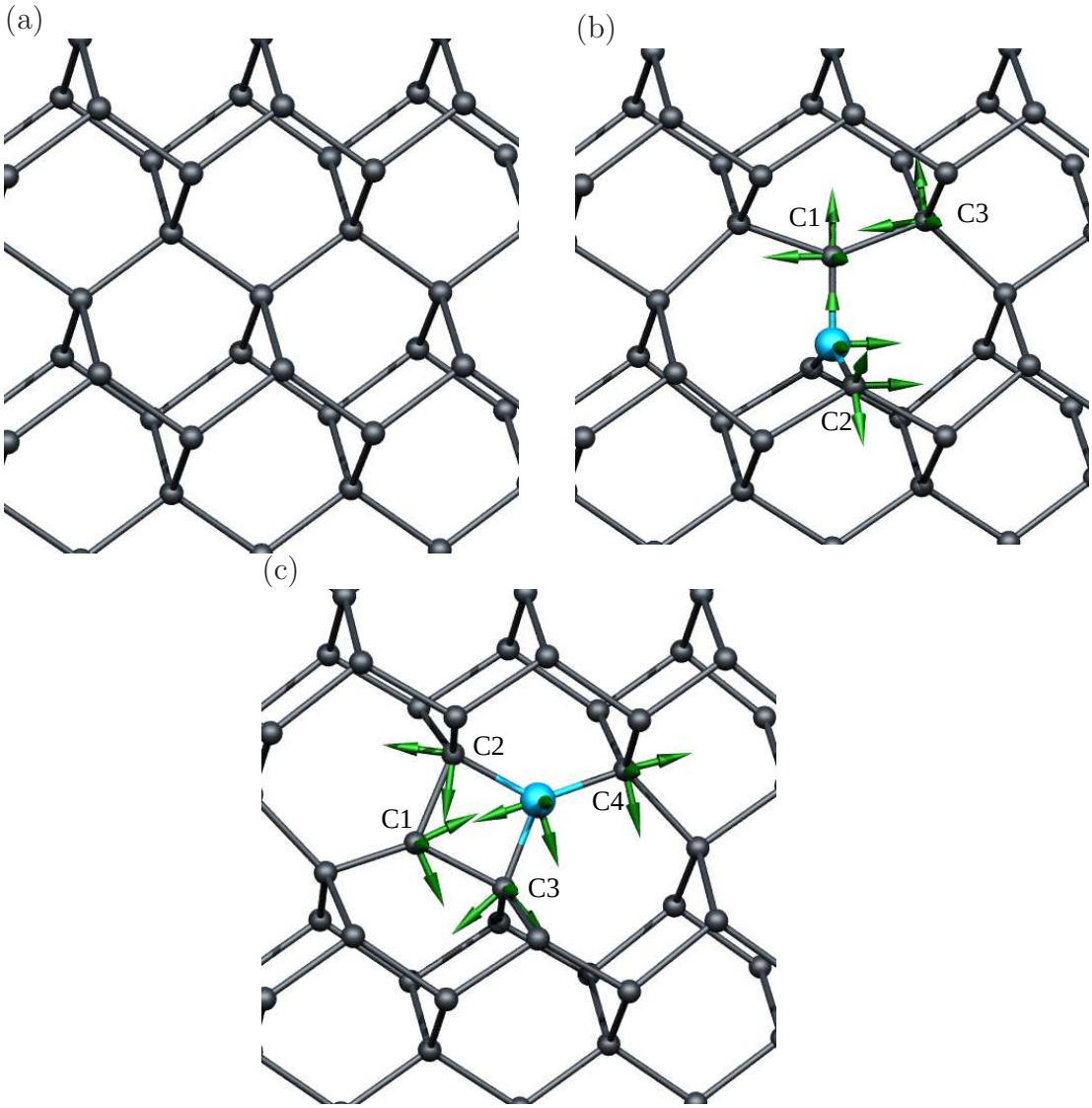

Figure 4.8: Models proposed for epr-active nitrogen interstitial centres in diamond: (a) representative of defect-free diamond, (b) the $N_{[001]}$ model for WAR9, and (c) the $N_{[001]}$–$I_{[001]}$ model for WAR10. Arrows indicate the calculated principal directions of the hyperfine tensors at ^{15}N and labelled ^{13}C sites. Vertical and horizontal axes are [001] and approximately [110], respectively, with the structures rotated slightly to show atoms that would otherwise be eclipsed from view.

Recently [53], two $S = 1/2$ epr-defects have been observed, labelled WAR9 and WAR10 in ^{15}N isotopically-enriched high-temperature–high-pressure grown synthetic diamond. The material had been subject to electron irradiation and a high-temperature anneal sufficient to remove all mono-vacancies performed. The material is understood to have an inhomogeneously distributed N concentration that means some regions contain isolated N, whereas others contain N in the aggregated, A-form. Both centres are in low concentration (< 1ppm) and are not affected by annealing up to 1800 K. In addition to the impact of temperature upon the centres, the key data for determination of atomistic structures comes from the interpretation of the angular dependence of the spectra, yielding the symmetry of WAR9 and WAR10 to be C_{2v} with {110} mirror plane, and C_{1h} with a {110} mirror plane, respectively. The hyperfine interactions between the unpaired electron and nuclear spins at the nitrogen site are small in both cases. Based upon the symmetry and processes involved in the formation of the centres, models were proposed for these epr-centres as shown in figure 4.8, being $N_{[001]}$ and $N_{[001]}$–$I_{[001]}$ structures, respectively, with the latter being of a similar form to the R1-epr centre.

However, there is a critical issue to address in these assignments: both centres are stable at 1800 K. This is at odds with the calculated [66] migration barrier for $N_{[001]}$, being just 1.7 eV that would most likely correspond to rapid diffusion below 1000 K, consistent with the formation of H1a in type-Ib material. It is possible that the measurements are over an insufficient time-scale to see the loss of $N_{[001]}$ to traps if the mean-free-path is short compared to the average distance to a trap site, but this seems unlikely given that the anneal is sufficient to remove other radiation products such as lattice vacancies which possess higher migration barriers. In addition, $N_{[001]}$–$I_{[001]}$ pairs have been proposed as an explanation for optically transitions at 2.807 and 3.188 eV in irradiated and annealed type-Ib material [66], as they have the required band-gap states for the electronic transitions and the local modes that explain the side-bands to the zero-phonon transitions. These centres anneal out well below 1800 K, at around the same temperature as H1a [60]. If the proposed structures are unable to explain

the WAR9 and WAR10 epr centres, alternative structures must be sought.

Next, the results of first-principles simulations of models for the WAR9-10 centres are presented, including those originally proposed, shown in figure 4.8. We calculated the hyperfine interactions for both the ^{15}N and key ^{13}C sites and compare the magnitudes and directions with those reported from experiment.

We begin with the models proposed previously [53] for WAR9 and WAR10, shown in figure 4.8, and discuss the merits of each assignment in turn based upon the simulation of the hyperfine interactions at the nitrogen site.

The calculated hyperfine tensors for $N_{[001]}$ are reported in table 4.4. It should be noted that for the nitrogen atoms in both simulation and experiment have directions that are entirely specified by the symmetry of the system, and the agreement of the angles in no way either adds to or detracts from any assignment of microscopic structure. We therefore focus upon the principal values, for which an understanding of the electronic structure is helpful. Chemically, the nitrogen atom is fully saturated forming three σ-bonds with the nearest three carbon atoms. Two electrons occupy a lone-pair orbital aligned along [110], which has an energy around 0.9 eV above the top of the valence band. The central carbon atom (labelled C1 in figure 4.8) forms three σ-bonds with its neighbours, with the fourth electron occupying a radical p-orbital aligned along $[1\bar{1}0]$. The spin polarisation of the system results in an occupied spin-up orbital around mid-gap and an empty, spin-down state in the upper half of the band-gap. The localisation of the majority of the spin-density in the carbon radical orbital leads to the small, nearly isotropic hyperfine interaction calculated for the ^{15}N, and the large highly anisotropic hyperfine interaction with ^{13}C1.

The RMS value for the nitrogen site is 12.4 MHz and 8.1 MHz from theory and experiment, respectively, so if the assignment of WAR9 to $N_{[001]}$ is correct, theory overestimates the hyperfine interaction by around 50%. In absolute terms, however, based upon comparisons of calculated hyperfine interactions for other N-containing point defects in diamond [48, 50] the agreement between theory and experiment is tolerable, and on the basis of the hyperfine interactions alone, the $N_{[001]}$ model for

WAR9 is plausible.

Table 4.4: Hyperfine tensors (MHz) for ^{15}N and ^{13}C in $N_{[001]}$, as shown in figure 4.8(b). Directions are indicated in parentheses using spherical polar coordinates as defined in section 7.2. Experimental data for WAR9 are taken from [53]. Note, the angles for A_2 from experiment are equivalent to those expressed from theory under the convention in section 7.2.

	A_1	(θ, φ)	A_2	(θ, φ)	A_3	(θ, φ)
			$N_{[001]}$			
N	11	$(90, 45)$	12	$(0, 0)$	14	$(90, 315)$
C1	96	$(90, 225)$	96	$(0, 0)$	350	$(90, 315)$
C2	51	$(90, 45)$	52	$(55, 135)$	68	$(36, 315)$
C3	−27	$(8, 45)$	−24	$(82, 225)$	−22	$(90, 315)$
			WAR9			
N	8.30	$(90, 45)$	7.85	$(180, 45)$	8.17	$(90, 315)$

Although the agreement between the experiment and model principal values is tolerable, they are certainly not convincing in isolation and we are yet to address any other aspects of the centre. In particular, the thermal stability is a serious problem with the assignment of $N_{[001]}$ to WAR9, which has been shown to be stable to at least 1800 K. This must cast significant doubt over the assignment of WAR9 to $N_{[001]}$.

We now turn to WAR10. The R1-like $N_{[001]}$–$I_{[001]}$ complex (figure 4.8(c)) has low symmetry, but sufficient to constrain some of the principal direction angles. As with the $N_{[001]}$ centre, the nitrogen and one of the C-atoms form three σ-bonds and give rise to p-orbitals that are occupied by the balance of the electrons. However, in contrast to $N_{[001]}$, the p-orbitals are not at right-angles: they are parallel. In the R1, di-self-interstitial centre the three-fold-coordinated atoms are equivalent so that the

gap-states are made up from linear-combinations of both sites. In $N_{[001]}$–$I_{[001]}$ the two sites are non-equivalent, and the electronic structure is very similar to $N_{[001]}$, being made up from a lone-pair orbital with an energy close to the valence band top, and a half-filled C-related radical.

The calculated hyperfine interactions for the R1-like $N_{[001]}$–$I_{[001]}$ centre are, in line with the observed values for WAR10, very small as listed in table 4.5, with most of the unpaired spin residing in the vicinity of the carbon radical. Purely in terms of the magnitudes, the calculated and observed values are in agreement and then one might be tempted to conclude that the R1-like model for WAR10 is plausible. However, the angles are in stark disagreement. For A_2 the directions are specified by the mirror plane, and must agree with experiment. Similarly, the values of φ in A_1 and A_3 are specified by symmetry as both lie within the mirror plane. The only values for comparison are θ_1 and θ_3, which are constrained by orthogonality of the principal directions. Thus, despite the relatively low symmetry there is in fact only one free parameter. The value of 72° for θ_1 is easy to justify. This places the direction at 18° to the [110] direction, which is also the angle formed by the line joining the N-atom to the C-radical, consistent with figure 4.8(c).

Thus, although the magnitudes are plausible, the directions constitute an serious objection to the assignment of the R1-like $N_{[001]}$–$I_{[001]}$ to the WAR-10 epr centre.

We have also examined other I- and N-containing centres with a view to the determination of an alternative model for either of WAR9 or WAR10. Given the high thermal stability it seems likely that the defects will have at least two interstitial components, and two such possible structures are shown in figure 4.9(a) and (b) based upon alternative models from previous studies [66, 73], labelled the Humble and π-bonded forms, respectively. Indeed, the Humble structure is slightly lower ($\sim 50\,\text{meV}$) in energy than R1-like arrangement, with the π-bonded form being 0.64 eV higher in energy than the Humble form. The structure in figure 4.9(a) has the advantage that is has the same symmetry as the R1-like form, and is therefore a ready candidate for WAR10.

Table 4.5: Hyperfine tensors (MHz) for ^{15}N and ^{13}C in the R1-like $N_{[001]}$–$I_{[001]}$ model for WAR10, as shown in figure 4.8(c). Directions are indicated in parentheses using spherical polar coordinates as defined in section 7.2. Experimental data for WAR10 are taken from [53]. Note, the angles for A_1 from experiment are equivalent to those expressed from theory under the convention in section 7.2.

	A_1	(θ, φ)	A_2	(θ, φ)	A_3	(θ, φ)
			R1-like $N_{[001]}$–$I_{[001]}$			
N	−4	(72, 45)	−2	(90, 315)	−2	(18, 225)
C1	85	(66, 45)	87	(24, 225)	326	(90, 315)
C2	−29	(83, 234)	−23	(81, 142)	−22	(11, 225)
C3	−30	(49, 45)	−25	(90, 315)	−23	(41, 225)
C4	−2	(13, 45)	−2	(90, 315)	−0	(77, 225)
			WAR10			
N	−1.01	(134.8, 45.0)	0.00	(90.0, 315.0)	1.00	(44.8, 45.0)

The hyperfine interactions calculated for these forms are listed in table 4.6. The values for the Humble-structure are small and consistent with experimental values for WAR10, but as with the R1-like structure, the directions disagree. Again, the directions we find can be traced to the local structure, being defined for the N-site by the direction to the carbon radical. The principal values for π-bonded model are large compared with WAR10, consistent with the relative proximity of the carbon-radical site which is immediately adjacent to the N-site, and in any case this structure does not have the correct symmetry. None of the relatively low-energy $N_{[001]}$–$I_{[001]}$ structures considered in this study satisfactorily match the experimental observations.

We have also considered N_s–$I_{[001]}$ pairs, although theoretically such defects are

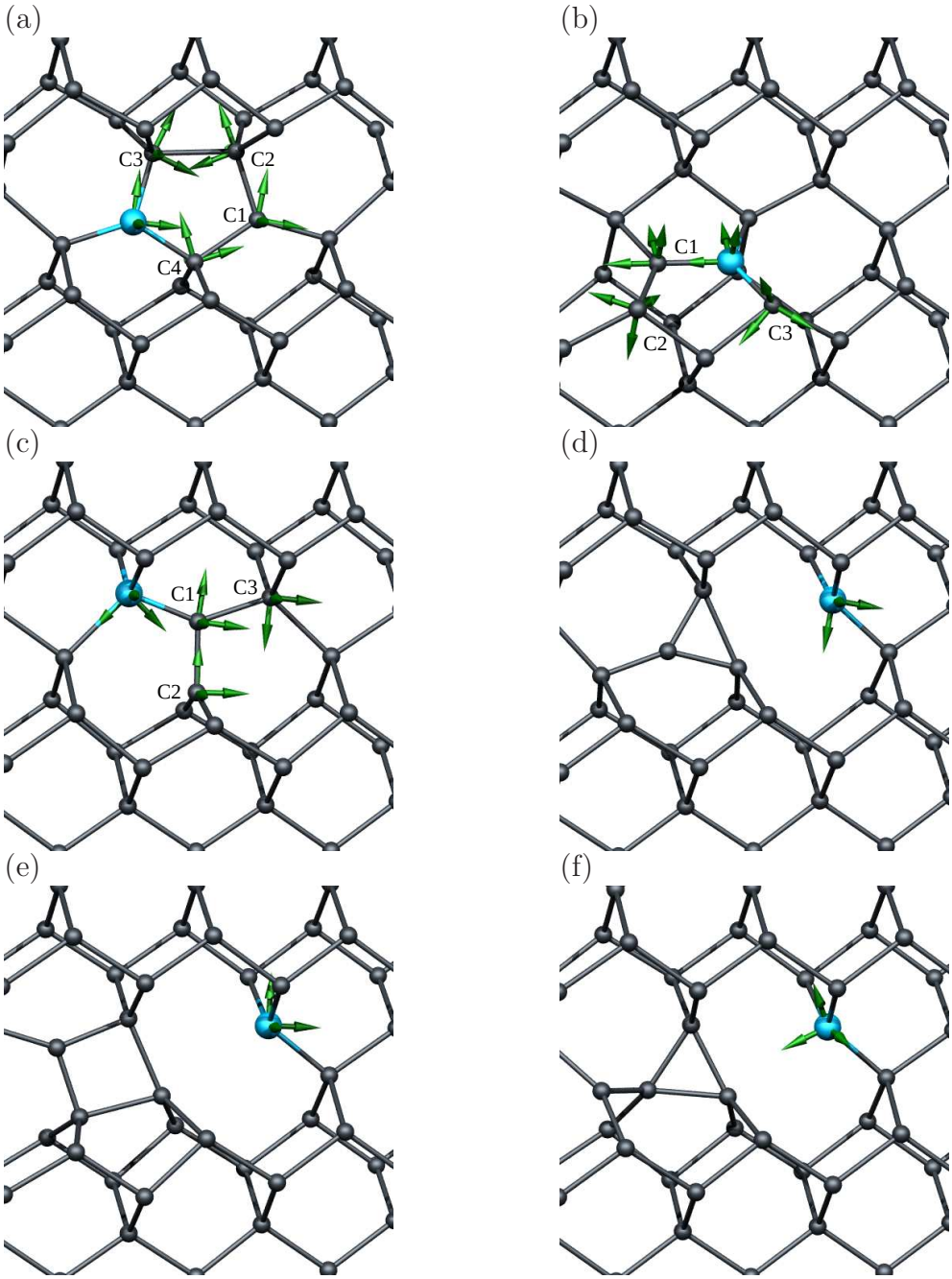

Figure 4.9: Models of $N_{[001]}$–$I_{[001]}$ and N_s–$I_{[001]}$ complexes in diamond. (a) the Humble and (b) the π-bonded form of $N_{[001]}$–$I_{[001]}$. (c) in nearest-neighbour configuration, (d) in next-neighbour configuration, (e) in third-neighbour configuration, (f) in third-neighbour configuration with different orientation. Arrows indicate the principal direction of the hyperfine interactions at ^{15}N and selected, labelled ^{13}C sites. The crystallographic directions are as in figure 4.8.

Table 4.6: Hyperfine tensors (MHz) for ^{15}N and ^{13}C in $N_{[001]}$, as shown in figure 4.9. Directions are indicated in parentheses using spherical polar coordinates as defined in section 7.2.

	A_1	(θ, φ)	A_2	(θ, φ)	A_3	(θ, φ)
Humble-ring structure: figure 4.9(a)						
N	−4	(90, 225)	−1	(83, 315)	0	(7, 135)
C1	87	(79, 315)	88	(11, 135)	326	(90, 225)
C2	−28	(70, 135)	−22	(20, 315)	−21	(90, 45)
C3	−2	(27, 135)	−2	(90, 225)	0	(63, 315)
C4	−29	(17, 315)	−24	(74, 135)	−21	(90, 45)
π-bonded structure: figure 4.9(b)						
N	−40	(42, 225)	3	(90, 315)	4	(48, 45)
C1	53	(50, 45)	54	(90, 315)	258	(40, 225)
C2	−25	(74, 349)	−21	(19, 201)	−18	(80, 81)
C3	−9	(45, 119)	−8	(54, 255)	−5	(113, 3)
N_s–$I_{[001]}$, nearest-neighbour: figure 4.9(c)						
N	−2	(45, 90)	1	(45, 225)	1	(45, 45)
C1	100	(82, 135)	102	(8, 315)	352	(90, 45)
C2	−38	(89, 135)	−29	(1, 315)	−26	(90, 45)
C3	−32	(5, 315)	−29	(85, 135)	−26	(90, 45)
N_s–$I_{[001]}$, second-neighbour: figure 4.9(d)						
N	1	(80, 225)	1	(90, 315)	1	(10, 45)
N_s–$I_{[001]}$, third-neighbour: figure 4.9(f)						
N	−3	(65, 41)	−2	(72, 303)	−2	(1, 211)

even less thermally stable than $N_{[001]}$. These structures are shown schematically in figure 4.9(c)–(f). For structures (c)–(e) the symmetry is consistent with WAR10, and the relative distance of the carbon-radical from the nitrogen site would be expected to yield a small value for the principal components of the hyperfine tensor.

Starting with the structure where N_s immediately neighbours the split-interstitial, we find that both the principal values and directions of ^{15}N agreed well with experimental results for WAR10. The nearly 45° angles seen in experiment for the free parameter can be explained by the angle between the carbon sites at the core of the defect and the location of the N atom. However, not only is this structure high in energy relative to the compositionally identical $N_{[001]}$, the barrier to rearrangement into $N_{[001]}$ is very small and it is inconceivable that such a geometry would exist even at moderate temperatures, let alone at 1800 K. However, it might perhaps suggest the local arrangement of components required, there being some additional component present that stabilises the carbon radical and nitrogen in a geometry similar to that shown in figure 4.9(c).

Chemical reconstructions in more distant pairs of N_s and I render them more plausible in terms of relative stability. In terms of the calculated hyperfine values, the distance between the C-radical and N-site leads to suitably small quantities[1], but the directions, once again aligned from the N-site to the radical site, are not a good fit. More seriously, based upon the convincing assignment of H1a [66,117], it seems highly probable that the metastable forms of N_s–$I_{[001]}$ will convert to $N_{[001]}$ at temperatures below 650°C, and therefore cannot easily explain the thermal stability of WAR10.

Finally, guided by the likelihood that larger aggregates of self-interstitials will be more thermally stable than $N_{[001]}$–$I_{[001]}$, we have also simulated some structures based upon the O3-epr centre [89] (figure 4.10(a)) and the very stable tetra-interstitial complex shown in figure 4.10(b), thought to be the basic building block of the highly stable interstitial platelet extended defects [64, 72, 73].

[1]For the structure shown in figure 4.9(e), the values are < 0.5 MHz and have therefore not been included in table 4.6.

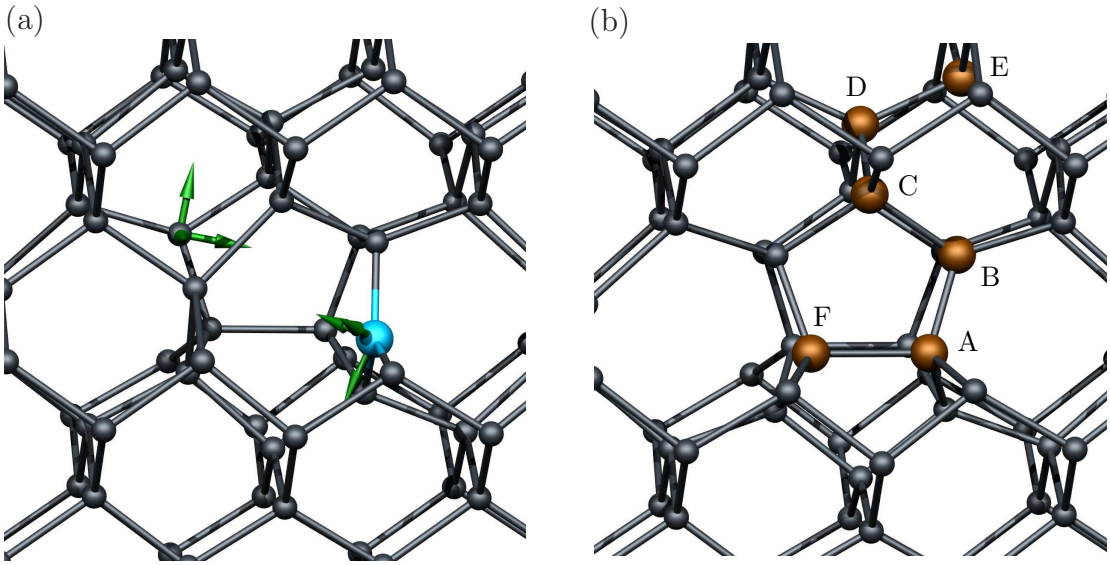

Figure 4.10: Models proposed for nitrogen interstitial-self-interstitials centres in diamond: (a) an O3-like structure, (b) the tetra-interstitial. Arrows in (a) indicate the calculated principal directions of the hyperfine tensors. Vertical and horizontal axes are [001] and approximately [110], respectively, with the structures rotated slightly to show atoms that would otherwise be eclipsed from view. Labelling in (b) indicates sites for the N and carbon radicals, as described in the text.

Substitution of one of the three-fold-coordinated sites in the O3 structure, as shown in figure 4.10(a), generates a defect with no overall symmetry, and such a defect cannot easily explain either WAR9 or WAR10. The calculated hyperfine interactions are listed in table 4.7, and are very small, consistent with the unpaired spin being predominantly localised at the distant carbon radical site. If the symmetry assignment for WAR10 is incorrect, this centre may be candidate based upon magnitude of hyperfine interaction at the N-site, but the angles remain a challenge.

Since the all-carbon tetra-interstitial is fully four-fold co-ordinated, there is no obvious site for the location of a three-fold nitrogen. However, there are several sites that can generate C_{1h} or even C_{2v} symmetry. We have optimised nitrogen substitution at a range of sites in or adjacent to the tetra-interstitial, and those indicated in figure

Table 4.7: Hyperfine tensors (MHz) for ^{15}N and ^{13}C in the O3-like structure shown in figure 4.10(a) and the tetra-interstitial, figure 4.10(b). In the latter case, the combinations of sites are indicated by the subscripts. Directions are indicated in parentheses using spherical polar coordinates as defined in section 7.2. Relative energies, E^{rel}, are for N at the different sites in the tetra-interstitial (eV).

	E^{rel}	A_1	(θ, φ)	A_2	(θ, φ)	A_3	(θ, φ)
O3-like structure							
N		−0.4	(72, 184)	0.1	(25, 50)	0.2	(73, 279)
C		92	(79, 223)	94	(11, 27)	337	(87, 133)
Tetra-interstitial							
N_A	0.0	−51	(89, 47)	−14	(10, 313)	−14	(80, 137)
C_F		87	(71, 133)	87	(19, 312)	309	(90, 43)
N_D	0.1	−167	(32, 45)	−139	(90, 135)	−137	(58, 225)
C_E		164	(40, 225)	165	(90, 315)	337	(50, 45)
N_C	0.7	−98	(50, 234)	−48	(64, 119)	−47	(51, 6)
C_B		140	(64, 14)	140	(58, 123)	302	(44, 253)
N_D	1.1	−75	(49, 136)	−30	(73, 30)	−30	(46, 282)
C_C		149	(63, 315)	150	(90, 225)	308	(27, 135)
N_C	1.2	−85	(25, 135)	−56	(90, 225)	−55	(65, 315)
C_D		84	(47, 326)	84	(84, 231)	254	(44, 135)

4.10(b) Equilibrium structures more closely resemble the P1-epr centre associated with neutral N_s, which has a relatively large hyperfine interaction at the N-site adjacent to a carbon radical: the defect has axial symmetry and the ^{15}N hyperfine tensor is characterised by [3] a value of -159.7 MHz parallel to the C_3 axis, and two components of -113.8 MHz perpendicular to the axis. The calculated hyperfine interactions at sites indicated in figure 4.10(b) are listed in table 4.7. Because the degree of relaxation of the 'broken' C–N bond depends upon the site in the defect structure, the range of hyperfine interaction magnitudes is quite large, being from around -14 to -138 MHz for the perpendicular component, and between -51 and -167 MHz for the parallel component. Even the smallest values are significantly larger in magnitude than the 8 MHz of WAR9, and ~ 1 MHz for WAR10.

It is perhaps surprising that the location of the N atom at site D is comparable in energy to where N is in the core of tetra-interstitial. With reference to WAR9 in particular, under reorientation between two equivalent locations of the carbon radical where the N atom is at site D, a C_{2v} structure can be obtained. The reorientation barrier is small (< 0.1 eV), so it is possible that at modest temperatures the motional average may be seen, such as proposed for the N4-epr centre [48]. We calculate that such an average would yields principal values of -137, -139 and -167 MHz for ^{15}N. These values are on average a factor of twenty times larger than the experimental values measured for WAR9, and we therefore conclude that nitrogen at site D, although potentially generating the correct symmetry, cannot be responsible for the observed epr centre.

Although the range of orientations listed in table 4.7 for the tetra-interstitial is not comprehensive, it captures the most stable arrangements we have examined. In addition, we have explored other locations both for the N atom and the associated carbon radical, and none yield hyperfine tensors that can explain either WAR9 or WAR10.

From the present calculations of hyperfine interactions for proposed structure of WAR9, we find that the neutral charge state of $N_{[001]}$ is plausible in terms of principal

values and the directions, but is very difficult to justify on the basis of thermal stability. For the proposed structure of WAR10, the principal values of the neutral charge state of the R1-like $N_{[001]}$–$I_{[001]}$ structure are consistent with experiment but the directions are not.

We conclude that the models proposed for both centres require further examination. The high thermal stability might point to a larger aggregate (i.e. a greater number of self-interstitial components). However, preliminary calculations investigating alternative N-containing radiation products have failed to identify a strong candidate for either epr centre.

4.3.4 H-divacancy defect in bulk diamond

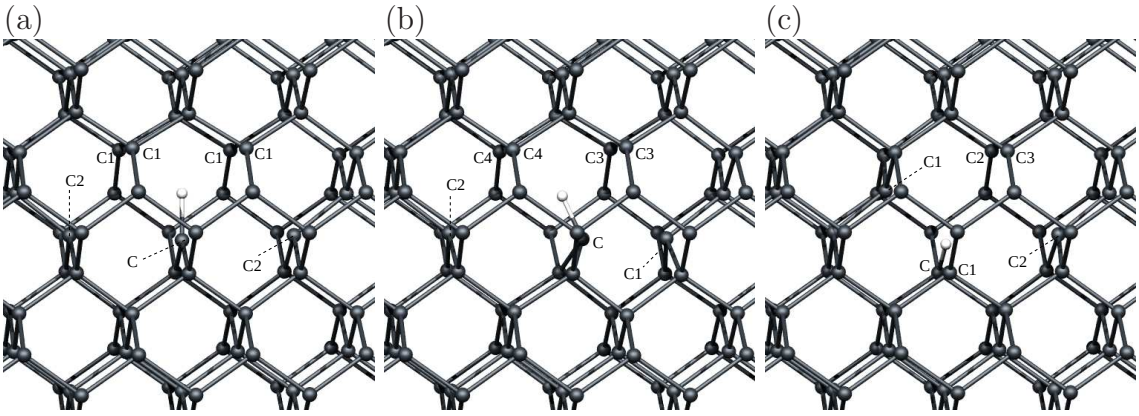

Figure 4.11: Schematic of V-H-V defects in diamond. White and gray atoms are hydrogen and carbon atoms, respectively.(a) the proposed model of WAR2 defect (V-CH-V), (b) reconstructed model of (V-CH-V) and (c) alternative model of WAR2 defect (V_2-H). Labelled sites are indicating the carbon radicals. The horizontal direction is [110] and the vertical direction is [001].

An epr defect with S=1/2 has been observed in CVD diamond which is labelled WAR2. This defect involves a single hydrogen atom and it has C_{2v} symmetry with a {110} mirror plane. The proposed structure of WAR2 defect neutral charge state is $(V\text{-}(CH)\text{-}V)^0$ where the hydrogen atom is bonded to a carbon atom which in turn

bonds with two other carbons with sp^2 configuration as shown in figure 4.11(a). Seven radical carbon atoms which surround the vacancies are included in this structure. The defect has been observed in diamond homoepitaxially grown on {001} oriented substrates, where it is preferentially aligned with respect to the [001] growth direction. Significantly, the defect can keep its polarisation (no reorientation) till anneals out after 1288 K.

There has been some debate about the role of the quantum mechanical behaviour of the hydrogen atoms for defects that including hydrogen atoms such as (N-V-H)$^-$ in bulk diamond [156]. Conventional density functional theory cannot explain this behaviour because the hydrogen atoms are regarded as static instead of taking into account the tunnelling of hydrogen atom between the equivalent sites. It has been also predicted that the hyperfine interactions of the static model of (N-V-H)$^-$ does not agree with the epr data while the hyperfine interactions of the structure with tunnelling of H atom between equivalent equilibrium sites are in agreement with the experimental results. This process could be the average contribution of three sites of epr measurement. Quantum tunnelling behaviour of hydrogen also succeed to explain the model of V_2-H$^-$ epr defect which is assigned to KUL2 epr spectra.

The critical issue to address in this assignment is the stability of the proposed structure (V-(CH)-V)^0 at more than 1288 K where there are two other more stable structures as will be discussed later. The hyperfine interactions of the proposed structure for WAR2 defect and the other two alternative structures have been modelled. The hyperfine interactions have been calculated for both the H and key ^{13}C sites and compared with the magnitudes and directions with that reported from experiment.

The discussion begins with the model proposed previously [26] for WAR2 as shown in figure 4.11(a), and the features of assignment in turn based upon the modelling of the hyperfine interactions at the hydrogen site.

First of all, the directions are completely specified by the symmetry of the system in both simulation and experiment for the hydrogen atom. The neutral charge state of (V-(CH)-V) structure can be thought of as possessing seven electrons from the

Table 4.8: Hyperfine tensors (MHz) for H and ^{13}C in the proposed and the alternative models of WAR2, as shown in figure 4.8(b). Directions are indicated in parentheses using spherical polar coordinates as defined in section 7.2. Experimental data for WAR2 are taken from [26] (Note, the angles for A_2 from experiment are equivalent to those expressed from theory under the convention in section 7.2).

	A_1	(θ, φ)	A_2	(θ, φ)	A_3	(θ, φ)
			(V-(CH)-V)^0			
H	0.0	$(0, 90)$	-3	$(90, 45)$	-1	$(90, 315)$
C	33	$(0, 90)$	27	$(90, 45)$	66	$(90, 315)$
C1	97	$(83, 53)$	98	$(55, 142)$	180	$(58.7, 131.4)$
C2	-99	$(55, 45)$	-56	$(35, 45)$	-55	$(90, 135)$
			(V-(CH)-V)^0-reconstructed			
H	4	$(49, 45)$	-3	$(41, 45)$	0.4	$(90, 45)$
C	21	$(72, 45)$	20	$(90, 45)$	27	$(18, 135)$
C1	-9	$(53, 45)$	-7	$(37, 45)$	-7	$(90, 45)$
C2	-145	$(55, 45)$	-73	$(36, 45)$	-72	$(90, 135)$
C3	24	$(82, 60)$	25	$(41, 60)$	37	$(67, 119)$
C4	167	$(88, 45)$	167	$(66, 115)$	323	$(56, 135)$
H(dynamic)	-0.3		0.4		0.9	
			V_2-H			
H	1	$(90, 45)$	0.4	$(0, 0)$	1	$(90, 315)$
C1	23	$(90, 45)$	23	$(55, 135)$	38	$(36, 315)$
C2	160	$(8, 45)$	161	$(82, 225)$	301	$(90, 315)$
C3	-119	$(55, 45)$	-58	$(35, 45)$	-57	$(90, 45)$
H(dynamic)	-0.5		-0.5		1	
			WAR2			
H	20.1	$(0, 90)$	30.9	$(90, 45)$	27.7	$(90, 315)$

dangling orbitals, and the electrons must be accommodated in the linear combination of these orbitals where one p-orbital on the unique carbon atom bonded with the H and six on the other carbon atoms which surround the vacancies. The hyperfine interactions of H and the radical carbon atoms have been calculated as listed in table 4.8. The principal values for the hydrogen atom are very small compared with experiment, where the root mean square (RMS) value of H site is 1.8 MHz and 26.6 MHz from theory and experiment, respectively. The calculated hyperfine interaction is smaller than the experiment by an order of magnitude.

There is another issue for assignment of WAR2 to an unreconstructed (V-(CH)-V)^0 structure, which is the thermal stability of the proposed structure. This structure can be reconstructed into the structure as in figure 4.11(b) with low symmetry C_s, where the latter is lower in energy by 0.4 eV. The hyperfine interactions of the static model for the reconstructed structure have been calculated and they are also reported in table 4.8 where the hyperfine tensors of the H site are very small comparing with epr data. An alternative model for a defect with C_{2v} symmetry would be a dynamic model, where the carbon atom C move toward the carbon atom C2 instead of C1 and it possesses the symmetry C_s. under reorientation between two equivalent locations of the C-H, a C_{2v} structure can be obtained where the reorientation barrier is small about 0.35 eV. The hyperfine parameters for this model are calculated to be $A_1 = -0.13$ MHz, $A_2 = 0.41$ MHz and $A_2 = 0.87$ MHz. Again, these values are very small and disagree with the experimental data.

The (V-(CH)-V)-reconstructed structure as in figure 4.11(b) can be further converted into another more stable structure as in figure 4.11(c) at growth temperatures , labelled V_2-H. The V_2-H with C_s symmetry is lower in energy than the proposed structure of WAR2 by 3.4 eV, and the barrier to convert from the (V-(CH)-V)^0- reconstructed to this structure is about 1.2 eV. The hyperfine interactions of the static model of V_2-H have been calculated and the hyperfine tensors are very small and does not agree with epr data. The quantum tunnelling for the H atom gives an alternative model for V_2-H where the hydrogen atom tunnelling between the three radical cites,

labelled C and C1. This dynamic model has an average symmetry C_{2v} which the same as observed via epr but it has different polarisation which directed along [111] direction. The calculated hyperfine parameters for the this model were $A_{\perp} = -0.5\,\mathrm{MHz}$ and $A_{\parallel} = 1.4\,\mathrm{MHz}$ which are very small comparing with experimental data. Here $A_{\parallel}$ is the component of the interaction along the [111] direction, and $A_{\perp}$ is the two components of the interaction perpendicular to [111] axis.

The hyperfine interactions of proposed model for WAR2 defect and alternative models have been investigated and the impact of quantum tunnelling has been studied. It has shown that the hyperfine parameters of proposed model does not consistent with epr data. This structure unstable thermally and there are more stable structures can be formed during diamond growth. The hyperfine parameters for the static and dynamic of (V-(CH)-V)-reconstructed and V_2-H models also were very small and disagreed with experiment. From the hyperfine calculations, the proposed and alternative models can not be assigned to epr observation and might be has different structure.

4.4 Conclusions

Density functional theory has used to calculate the hyperfine interactions of proposed models of the three new epr defects have been observed recently which are labelled WAR9, WAR10 and WAR2. The main issue of the proposed models is the thermal stability of these structures where these structures are not stable at growth temperatures. There is another issue of exclusion of assign the proposed structures to epr observation which is the hyperfine interactions between the unpaired electron and the nucleus. The calculations showed that the hyperfine parameters of the proposed models were not consistent with epr data.

For P1 and N-V centres in diamond, both defects are very known and the results of hyperfine interactions from AIMPRO calculations are in good agreement with epr observation. Some carbon cites are not determined correctly via epr and ENDOR

measurements and they are distinguished by AIMPRO as discussed above. Both P1 and N-V defects are chosen to study their polarisation in (110), (111) and (001) diamond surfaces especially for N-V centre in (110) surface because it has been observed recently that that 100% of this defect is preferentially aligned along specific direction as will be discussed in details in chapter 7.

Chapter 5

Diamond surfaces

5.1 Introduction

The defects in materials can have a large effect on their properties and the surfaces could be the largest defects exist in every real material. Surfaces can introduce dangling bonds, impurities to terminate them, electric dipoles and atomic reconstructions [44, 181]. For who those wishing to take advantage of material's characteristics, especially the effect of atmosphere on the surface properties, it is important to understand the nature of the material's surface and its effect on the properties of the bulk.

For diamond, it possesses very useful surface properties such as negative electron affinity and they have attracted great attention for many electronic applications [13, 28, 35, 122, 144, 165, 183]. These properties also are depending on the termination of the surface dangling bonds by hydrogen, oxygen or other species of atoms. The most important crystallographic orientations technologically are (110) and (111) and (001) as a result of the way that diamond crystals grow during the CVD process [11, 150].

DFT has been employed to investigate the structural and electronic properties and energies of the clean and hydrogen-terminated diamond surfaces for (110), (111) and (001) surface orientations as a part of present work.

5.2 Method

All the calculations were carried out using the GGA as implemented in the *AIMPRO* as described in chapter 2. To study the structural properties and energies, diamond surfaces have been simulated using the standard slab-geometry approach, with the base unit cells as detailed in Table 5.1. These diamond slabs have thicknesses of 1.6 nm, 1.5 nm and 1.5 nm for (110), (111) and (001) diamond surfaces, respectively. A vacuum layer of ∼0.6 nm was used in all cases, sufficient for the electrostatic potential to reach the vacuum limit. In all cells, the surfaces are terminated by hydrogen atoms to passivate the dangling bonds on the surface. All the atoms were allowed to move during the optimisation until get minimum energy and the forces became in the order 10^{-4} au.

The Gaussian functions are atom-centred, and for each C atom are constituted from eight fixed linear-combinations of s and p-orbitals, plus a set of d-functions for polarisations. This constitutes a basis of 13-functions per C-atom. The H atom is represented by basis sets made up from independent sets of s, p functions with three widths, constituting 12-functions per atom. A similar approach was previously used successfully to study the electronic structure of different diamond surfaces [161, 169, 170]. For bulk diamond as discussed in the previous chapter, the approach yields a lattice constant and bulk modulus of 3.573Å and 440 GPa, in good agreement with experiment.

The Brillouin zone was sampled using the Monkhorst-Pack scheme [129]. For surfaces, since there is no dispersion in the surface normal direction, the Brillouin zone is effectively two dimensional, and for the (110), (111), and (001) surfaces, 3×3, 3×3, and 4×3 meshes were used, respectively.

The absolute surface energies ($E_{\rm surf}$) have been calculated for clean and hydrogenated (110), (111), and (001) diamond surfaces. These energies are obtained using

$$E_{\rm surf}^{n\times m} = \frac{1}{2nm}\{E_{\rm tot}(N) - \sum \mu_i N_i\} \tag{5.1}$$

where $E_{\rm tot}$ is the total energy, μ_i is the chemical potential of the atom i and N_i the

Table 5.1: Surface lattice vectors in units of a_0, composition, and number of atomic layers of carbon (n) in the slab supercells used in this study.

Orientation	Termination	$\vec{v_1}$	$\vec{v_2}$	Composition	n
(110)	clean	$[110]/\sqrt{2}$	2[001]	C_{24}	12
(110)	H	$[110]/\sqrt{2}$	2[001]	$C_{24}H_4$	12
(111)	clean	$[1\bar{1}0]/\sqrt{2}$	$[10\bar{1}]/\sqrt{2}$	C_{14}	14
(111)	H	$[1\bar{1}0]/\sqrt{2}$	$[10\bar{1}]/\sqrt{2}$	$C_{14}H_2$	14
(001)	clean	$2[110]/\sqrt{2}$	$[1\bar{1}0]/\sqrt{2}$	C_{32}	16
(001)	H	$2[110]/\sqrt{2}$	$[1\bar{1}0]/\sqrt{2}$	$C_{32}H_4$	16

number of atoms of type i. The prefactor $\frac{1}{2}$ indicates that two equivalent surfaces are included in the calculations. The chemical potential of hydrogen and carbon that used in present calculation are obtained from calculation of free hydrogen atom including spin polarisation and 216-supercell carbon atoms, respectively. The H adsorption energy (E_{ad}) has been calculated as well, which is obtained from calculating the energy difference between the hydrogenated surface and the stable clean surface per H atom.

5.3 Results

5.3.1 (110)-clean and Hydrogenated surface

The diamond (110) clean surface is layers of zigzag chains as shown in figure 5.1. It has been shown that the (110) surface does not reconstruct [104, 121]. The dangling bond on each carbon atom contributes to form delocalised π orbitals and extends along the chain and therefore shows metallic band structure as illustrated in figure 5.3(a). From the optimised structure of (110)-1×1 diamond surface as shown in figure

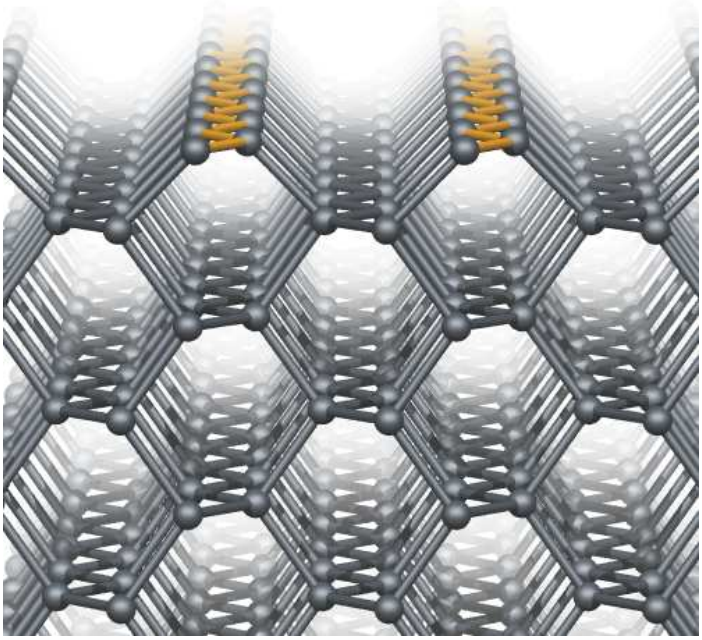

Figure 5.1: Perspective view of the optimised clean C(110) surface. The vertical direction is z axis along [110] and the horizontal direction is x axis along [001]. The zig-zag at the top (orange in colour) shows π-bonded chain.

5.2(a), there is no reconstruction for the surface but the uppermost carbon atoms are moved causing a displacement to the first layer of structure in the perpendicular direction to the surface. The C−C bond length along the zig-zag in the first layer (surface) is calculated to be 1.43 Å, which is a reduction to 92.4 % of that of a bulk C−C bond. Thus, the uppermost carbon atoms are not tetrahedrally coordinated, but rather support delocalised π network running along the zig-zag chains. Also, the bond length of C−C along the zig-zag chain in the second layer is about 1.51 Åas in figure 5.2(a), which is 97.6 % of that of a bulk C−C and the carbon atoms are approximately tetrahedrally coordinated. The distance between the first and second layers ΔZ as indicated in figure 5.2(a) is reduced by 0.18 Å comparing to the bulk, while the distance between the second and third layers is increased by 0.03 Å which are agreed with the the values of 0.17 and 0.03 Å that obtained from LDA calculation [104]. That means

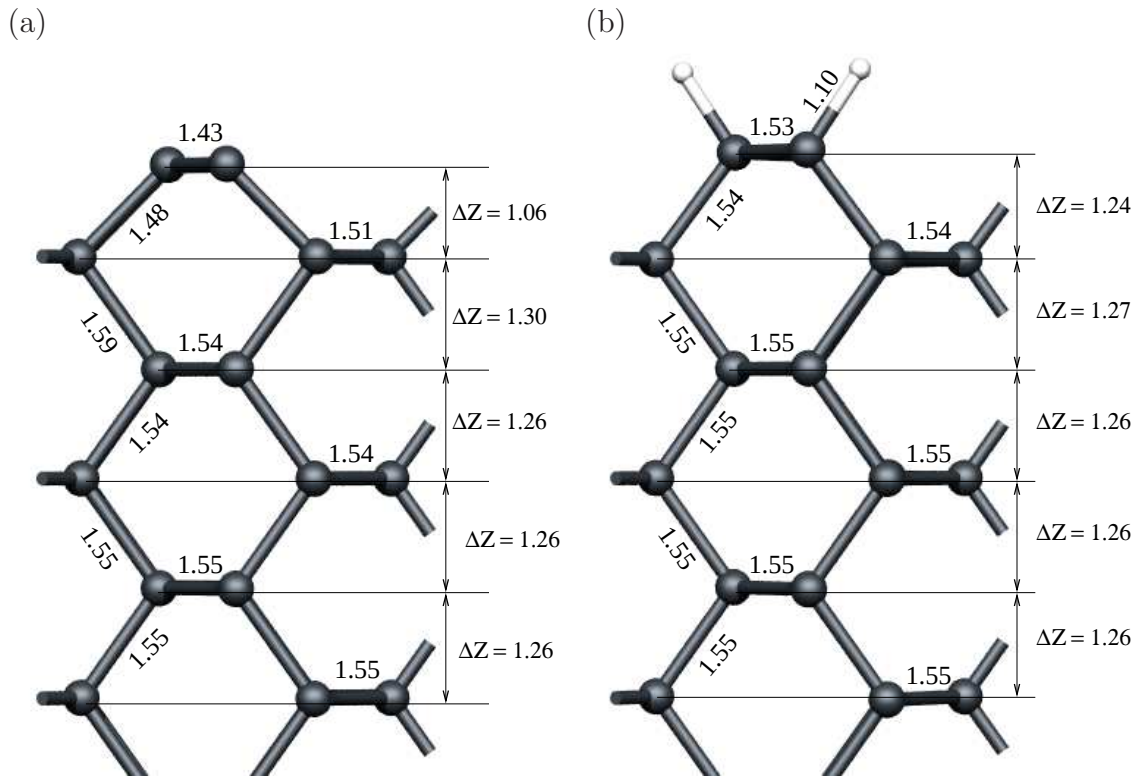

Figure 5.2: Section of relaxed atomic geometries for (a) clean and (b) hydrogenated (110)-1 × 1 diamond surface. Structural parameters include layer separations, bond lengths, and intra-layer bucklings (ΔZ). All values are in $\mathring{A}$. White and gray atoms are hydrogen and carbon, respectively. The horizontal and the vertical axes are x and z.

the uppermost carbon atoms have moved downward in the direction normal to the surface and toward the bulk diamond, while the carbon atoms in the second layer have moved upward. The C−C length on the deep layers and between them have remained as in bulk diamond. Termination of diamond surfaces by hydrogen atoms can affect on the structure and electronic properties, where addition of hydrogen removes dangling, and dimer bonds at the surface. In the case of (110) diamond surface the addition of hydrogen atoms to the carbon atoms at the surface increase the carbon coordination from three to four, the surface optimises back to an almost bulk diamond structure, and thus removing the π network along the surface.

Table 5.2: Energetics of the clean and hydrogenated (110), (111) and (001) diamond surfaces (in eV per surface site). $E_{\rm sur}$ ($E^*_{\rm sur}$), $E_{\rm ad}$ ($E^*_{\rm ad}$) and χ (χ^*) refer to the present (previous) studies of the absolute surface energies, H-adsorption energies and electron affinities, respectively. χ^{expt} is the experimental electron affinities. References data are taken from [16, 35, 58, 106, 107, 123, 151].

Termination	$E_{\rm sur}$	$E_{\rm ad}$	$E^*_{\rm sur}$	$E^*_{\rm ad}$	χ	χ^*	χ^{expt}
			110-surface				
1×1:Clean	1.54		1.66		+0.90	+0.90	+0.70
1×1:H	−2.57	−4.11	−2.68	−4.34	−2.58	−2.40	−1.10
			111-surface				
1×1:Clean	2.27		2.18		+1.25	+1.37	
1×1:H	−2.66	−4.94	−2.8	−4.15	−2.10	−2.03	−1.65
2×1:Clean	1.27		1.35		+0.39	+0.35	+0.38
2×1:H	−1.99	−3.27	−2.11		−2.27	−2.40	
			001-surface				
1×1:Clean	3.5		3.63		+2.15		
1×1:H (canted)	−1.77	−3.52			−2.38	−2.36	
2×1:Clean	2.01		2.12		+0.64	+0.69	+0.50
2×1:H	−2.29	−4.3	−2.42	−4.54	−2.07	−2.07	−1.30

The C−C bond length of uppermost atoms (surface) of the clean (110) surface is affected by adding the hydrogen termination. From figure 5.2(b), the movement of the first and second layers again in the direction normal to the surface. The C−C bond length at the first layer becomes 1.53 Å or 98.6 % of C−C length in bulk diamond instead of 1.43 Å for clean (110) surface. In the second layer, the bond length of C−C

is 1.54 or 99.8 % of the bulk comparing to 97.6 % for clean (110) surface. The first layer has moved downward by just 0.01 Å normal the surface which is insignificant and the second layer shifted from its perfect position by ten times less than this value. There is no changes for the third and deep layers from their ideal positions.

The absolute surface energy and H-adsorption energy values have been investigated for both clean and hydrogenated (110)-diamond surfaces and they are summarised in table 5.2. The absolute surface energy of the clean (110) surfaces is calculated to be 1.54 eV which in agreement with previous LDA calculations [104]. The surface energy is reduced by adding hydrogen atoms to the surface by −4.11 eV which is also in accord with the value of −4.34 eV for that calculated by LDA.

(a) (b)

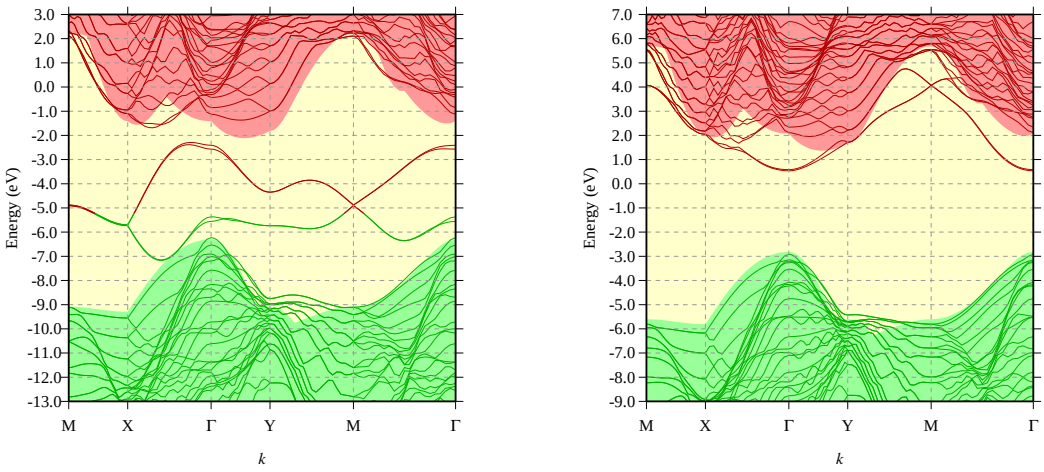

Figure 5.3: The electronic band structure of (a) clean and (b) hydrogenated (110)-1 × 1 diamond surface. The green and red colour indicate to occupied and unoccupied states. The lines and the shaded regions represent the band structure of surface slab and bulk diamond, respectively. The zero of the energy scale is the vacuum level of the system.

The band structure for clean and hydrogenated (110) diamond surface have been calculated in the present study as shown in figure 5.3. Figure 5.3(a) shows the band

structure of optimised clean (110) surface, where the energy bands of the surface slab align very well the levels from the bulk diamond. The nature of metallic for this surface is apparent at M and X points with combination of bonding (π) and anti-bonding (π^*) states, where the position of Fermi level with respect to the vacuum potential is 5.22 eV. These states are degenerate along X→M path in the Brillouin zone. Also, the π^* state along X→Γ has the largest dispersion of about 3.4 eV which in excellent agreement with previous calculations [104].

The electronic band structure for the (110)-hydrogenated surface is calculated as shown in figure 5.3(b). Adding the hydrogen atoms to the surface removes the occupied surface states from the gap and creates new unoccupied states beneath the bulk conduction band with parabolic-like shape around Γ point which are vacuum-related states [159], formed with the help of the ghost atoms. Also, the conduction band states are higher in energy than the vacuum potential, where the vacuum level sets to be zero in the energy scale of the band structure.

The electron affinity (χ) for clean and terminated (110) surfaces are calculated as reported in table 5.2. As can be seen in figure the vacuum level appears above the minimum conduction band for clean surface which means that the surface possesses positive electron affinity (PEA) with the value of +0.90 eV which is consistent with the experiment value of +0.70 eV [16, 104], while it appears beneath minimum conduction band for hydrogenated surface and that means the surface has negative electron affinity (NEA) with the value of −2.58 eV which agrees the calculated value of −2.40 eV that calculated in previous study [104] and significantly larger than the experiment value of −1.10 eV. The difference in electron affinity has to be attributed to the lowering of the potential barrier at the surface by the weaker dipole layer on the hydrogenated surface which in turn caused by the saturation of the dangling bonds with hydrogen. The difference in electron affinity values for hydrogenated diamond surfaces between the calculation and experiment might be came from the fact that it is difficult to produce 100% of H-terminated diamond surfaces in practice and also the presence of other surface impurities such as -O and -OH which increases the electron

affinity significantly even in small proportion [159]

5.3.2 (111)-clean and Hydrogenated surface

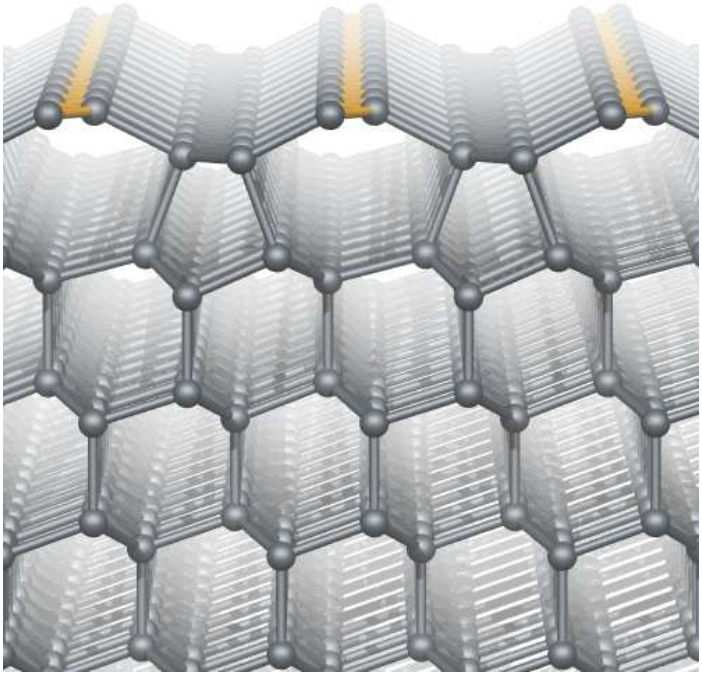

Figure 5.4: Perspective view of the optimised (111)-2 × 1 clean surface (Pandey chain). The vertical direction is z-axis along [111] and the horizontal direction is x-axis along [11$\bar{2}$]. The zig-zag at the top (orange in colour) shows π-bonded chain.

The (111) diamond surface with one dangling bond per surface atom, pointing perpendicular to the surface, is the natural cleaving plane of bulk diamond [149]. Also, bulk diamond naturally can be cleaved into another type of (111) surface, in which each carbon atom at the surface has three dangling bonds. The (111)-1 × 1 clean surface is not stable and reconstructs into several surface geometries [155]. One of the most stable structure is the Pandey chain which is a rather complicated 2 × 1 reconstruction. This surface is analogous to that first suggested for (111) surface of silicon [133] and this geometry with a 2 × 1 periodicity is widely accepted [134].

The present calculations showed that this surface can be formed by just a little shifting of the carbon atoms at the surface, where the carbon atoms at the surface for Pandey chain, form a zigzag chains that extend in parallel across the surface as shown in figure5.4.

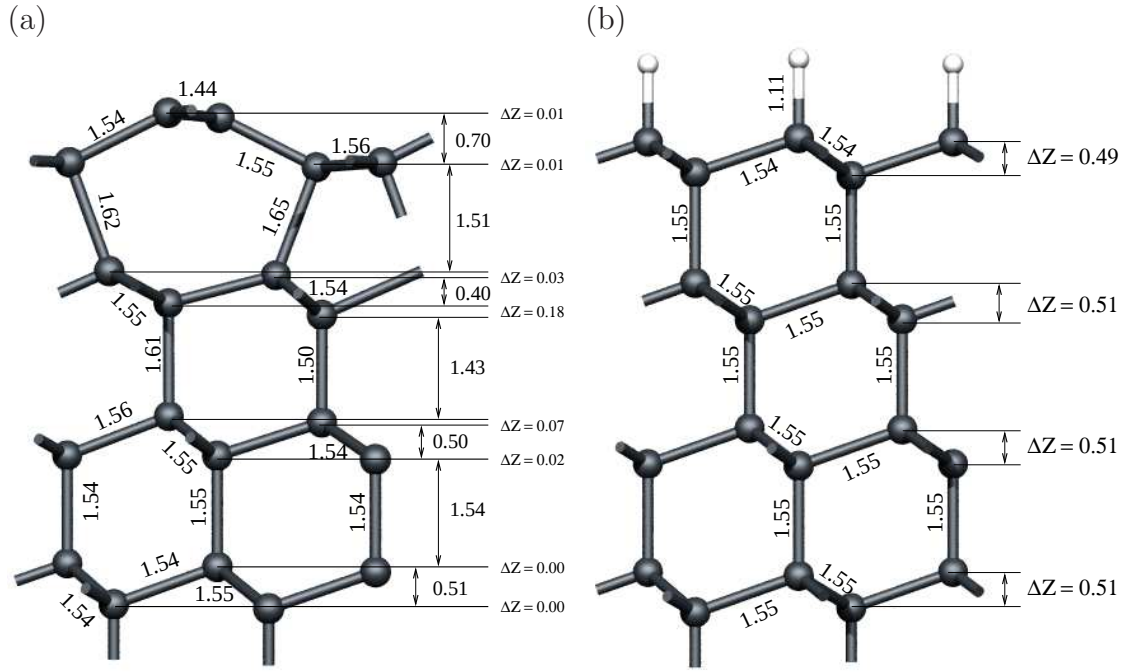

Figure 5.5: Section of relaxed atomic geometries for (a) 2×1 reconstructed clean (Pandey-chain) and (b) 1×1 hydrogenated (111)-diamond surface. Structural parameters include layer separations, bond lengths, and intra-layer bucklings (ΔZ). All values are in $\mathring{A}$. White and gray atoms are hydrogen and carbon, respectively. The horizontal and the vertical axes are x and z.

The (111)-2×1 clean surface is lower in energy than a non-reconstructed (111)-1×1 surface by 1.00 eV per surface atom as reported in table 5.2. The length of C−C bond of the zig-zag Pandey chain at the surface is calculated as shown in figure 5.5(a) to be 1.44 Å which shows a small degree of dimerisation, where the length of the C=C bond is 1.32 Å, comparable to graphite. According to the previous studies, there is no evidence for the dimerisation in Pandey chains has been found [106, 154, 174].

The C−C bond length of the chain in the second layer is 1.56 Å. The calculated C−C length values of the two chains in the present study are in agreement with the values of 1.43 and 1.54 Å found in another study [2]. The zig-zag chains in the first and second layers are not tilted significantly in the direction normal to the surface (z-direction), where the difference between the pair carbon atoms in the first layer is about 0.01 Å in [111]-direction, and the same value for the second layer as shown in figure 5.5(a). Several other theoretical studies have been investigated the tilting in the two zig-zag chains and it has been found they were flat [2, 106, 154, 174], which is supported by the present study.

For (111)-1 × 1 hydrogenated diamond surface, each dangling bond is terminated by one hydrogen atom and stabilises the bulk-terminated form [149]. The hydrogen termination of the clean surface give rise to formation of a metastable (2×1) structure and a stable (1 × 1) structure [106], and the most stable structure for the clean and hydrogenated (111) surfaces are the reconstructed (2 × 1) surface (π-bonded Pandey chains) and (1 × 1) H-terminated surface, respectively.

The (111) diamond surface is terminated by hydrogen atoms to remove the single dangling bonds. The (111)-1 × 1 diamond surface was found to be more stable energetically by 0.67 eV per surface C−C pair than H-terminated Pandey chain reconstruction, which being in accord with the calculated value of 0.69 eV, that has been obtained by previous studies [76, 106]. Termination of (111)-1 × 1 diamond surface lowers the surface energy up to −4.94 eV which is larger than that calculated using LDA by 0.79 eV. There is a very small change only in the uppermost double layer of carbon atoms as shown in figure 5.5(b).

The band structure of the clean Pandey chain surface is illustrated in figure 5.6(a) yielding features that are in good agreement with other calculations. This surface creates gap states throughout the Brillouin zone and similar to (110) surface, the dangling bonds share a delocalised π network running along the chain showing metallic nature, where they meet at the X point the position of the Fermi level with respect to the vacuum potential is 4.88 eV. The splitting between the occupied and unoccupied

(a) (b)

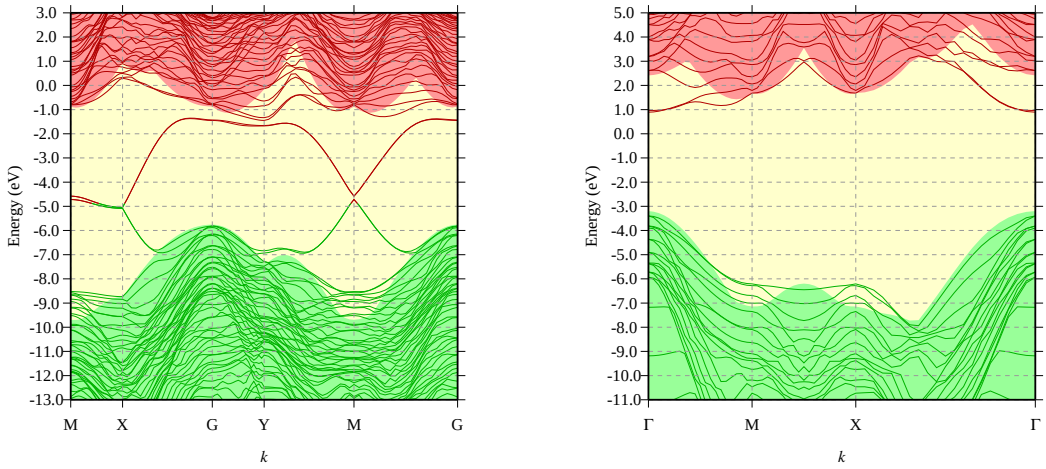

Figure 5.6: The electronic band structure of (a) (111)-2 × 1 clean and (b) (111)-1 × 1 hydrogenated diamond surface. The green and red colour indicate to occupied and unoccupied states. The lines and the shaded regions represent the band structure of surface slab and the bulk, respectively. The zero of the energy scale is the vacuum level of the system.

states in the band gap is about 4.5 eV at the Γ point which is in good agreement with the value of 4.8 eV obtained by previous calculation [175]. The very small energy splitting in the surface state around the M point is thought to be produced from the very small dimerisation of the chain at the top of the surface. In addition, it shows that the vacuum level appears above the minimum conduction band which means this surface has a PEA with the value of +0.39 eV. This value agrees with the value of +0.35 eV obtained from other calculation [153] and it is consistent with the experimental observation [135].

In the case of hydrogenated (111)-1 × 1 diamond surface, the states in the band gap were disappeared and the bulk bands were shifted upward from their positions with the clean surface by 2.6 eV which is consistent with previous calculation. Also, hydrogenation of the surface introduces unoccupied states below the conduction band

around Γ point which are vacuum-related states [159]. In addition, the vacuum level is localised below the conduction band and that means this surface have NEA. The electron affinity for this surface have been calculated to be −2.10 eV which in consistent with the value of −2.03 eV obtained from other calculation [153].

5.3.3 (001)-clean and Hydrogenated surface

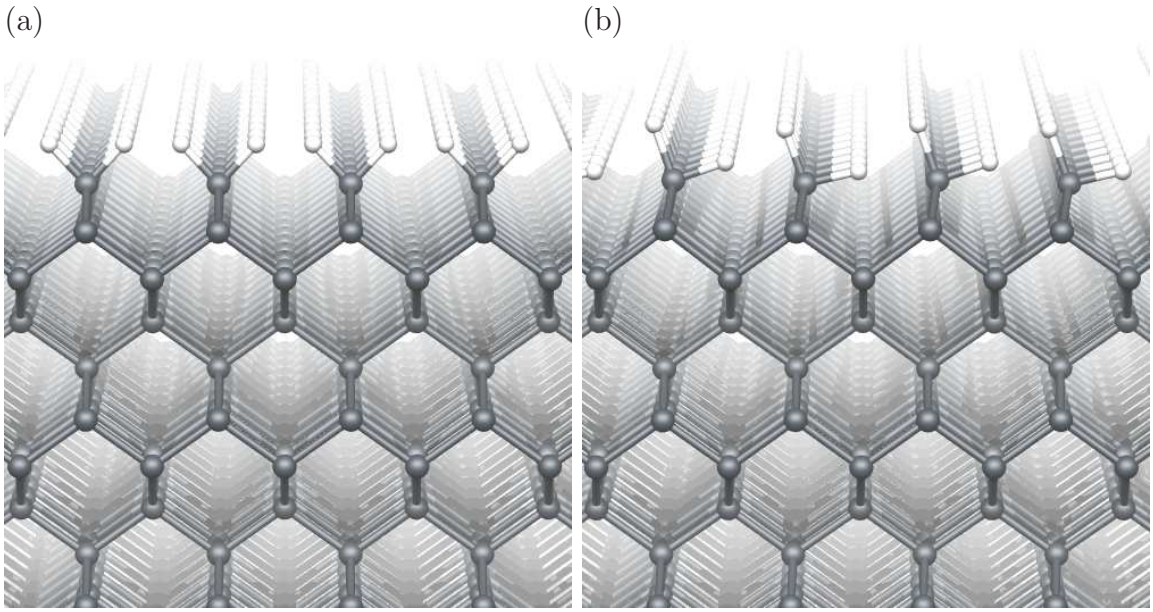

Figure 5.7: Perspective views of the optimised (001)-1 × 1 (a) symmetric configuration and (b) canted di-hydrogenated surfaces. The vertical direction is z axis along [001] and the horizontal direction is x axis along [110]. The white and gray spheres are hydrogen and carbon atoms, respectively.

The clean (001) diamond surface contains two dangling bonds per surface atom. It has been predicted that forming mutual bond of the surface atoms is lower in energy and then confirmed after that experimentally [56]. The absolute surface energy of (001)-2 × 1 clean surface is calculated to be 2.01 eV, lower in energy by 1.49 eV than the unreconstructed (001)-1 × 1 clean surface which in agreement with previous calculations [104]. Thus, (1 × 1) geometry is unstable and it can reconstructed into a

(2×1) geometry forming π-bonded dimers as shown in figure 5.9.

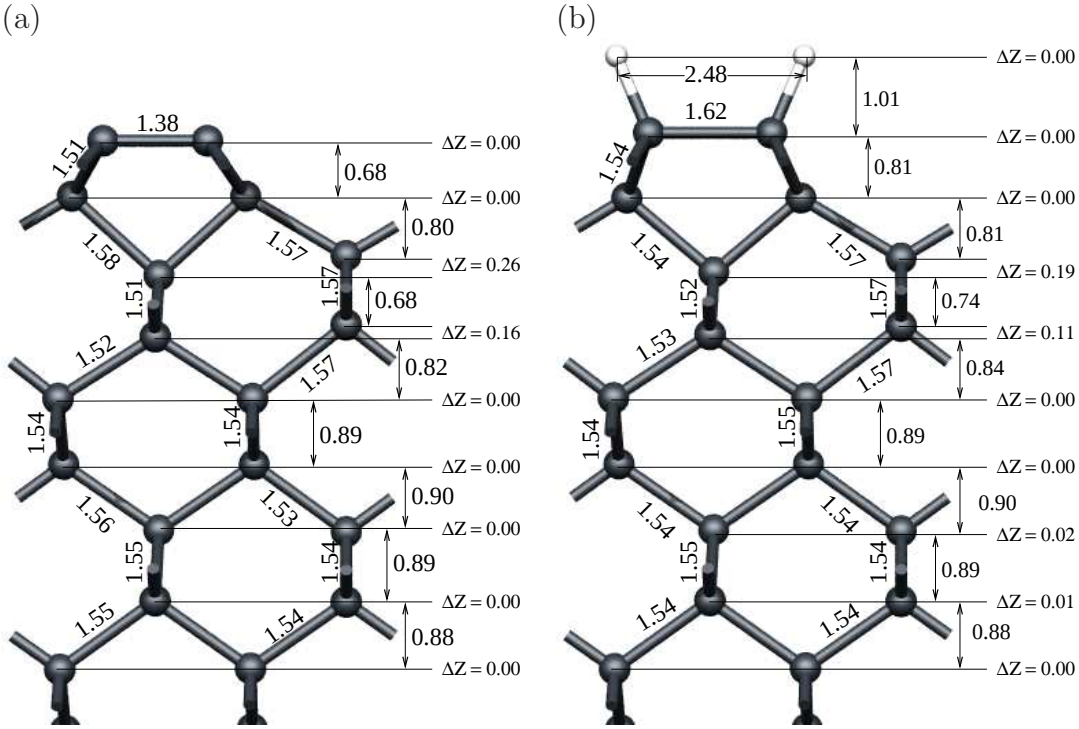

Figure 5.8: Section of relaxed atomic geometries for (a) clean and (b) hydrogenated (001)-2×1 diamond surface. Structural parameters include layer separations, bond lengths, and intra-layer bucklings (ΔZ). All values are in Å. White and gray atoms are hydrogen and carbon, respectively. The horizontal and the vertical axes are x and z.

From present calculations of the clean (001)-2×1 surface, the length of the dimer bond is 1.38 Å which is in good agreement with previous LDA-DFT calculation [58, 105], and 3% bigger comparing with the value of 1.34 Å for C=C double bonds. The difference between the pairs of atoms in at the same layer in the direction normal to the surface Δz are measured which another important feature of the structure. The dimers at the surface are not tilted to any degree and there is significant difference only in the third and forth layers with the values of 0.26 and 0.16 Å, respectively. These values agree with previous published data with respect to the *ab initio* DFT studies [58, 162]

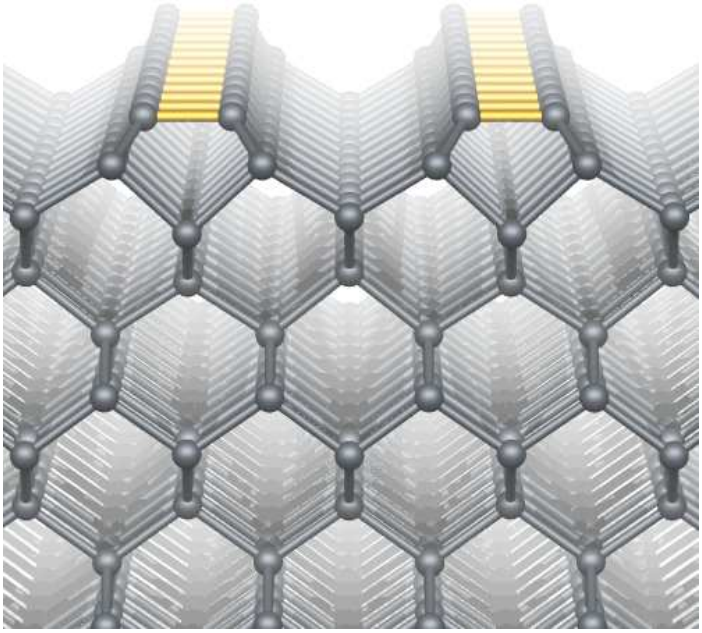

Figure 5.9: Perspective view of the optimised (111)-2 × 1 clean surface (Pandey chain). The vertical direction is z-axis along [001] and the horizontal direction is x-axis along [110].

The (001)-1 × 1 dihydride surface for both canted and symmetric geometry have been modelled as shown in figure 5.7. From the present calculations, the distance between the two hydrogen atoms is 1.09 Å, for dihydride symmetric surface and increased up to 1.37 Å for dihydride canted surface and the surface energy is lowered from −1.59 to −1.77 eV. This change in the distance is due to steric repulsion, where bonded hydrogen atoms tend to avoid each other. The stability of dihydride symmetric surface has been examined and it has been found that the hydrogen atoms deviated from the symmetric positions without dissociation from the surface [185]. Hydrogen termination of (001)-2 × 1 surface is widely accepted and considered to be the most stable under normal conditions compared to other hydrogen-terminated (001) surface [75, 148, 178], and so this was the surface studied in present work. Termination of (001)-2 × 1 clean surface lowers the surface energy to −4.3 eV which is consistent

with the value of $-4.54\,\text{eV}$ that obtained by LDA calculations [104]. Also, it is more stable energetically than unreconstructed (001)-1×1 hydrogenated surface by $0.52\,\text{eV}$ per H atom.

(a) (b)

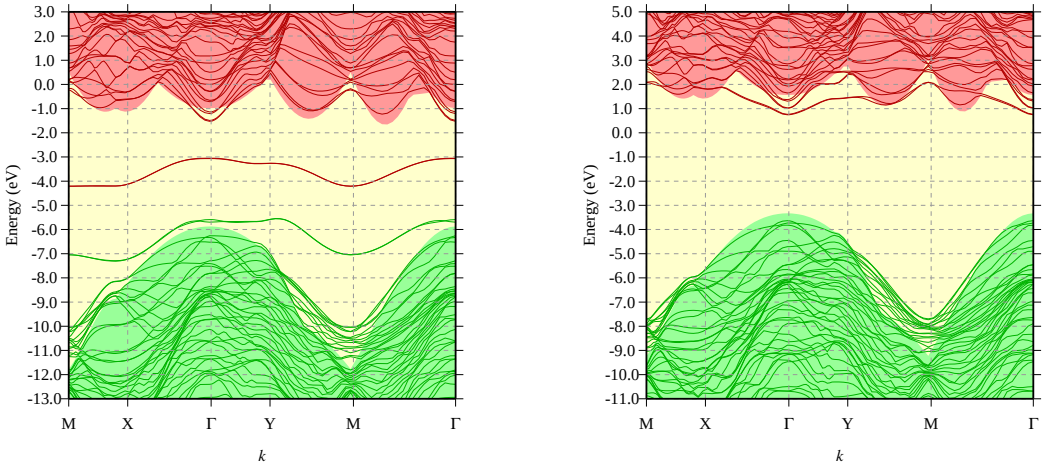

Figure 5.10: The electronic band structure of (a) clean and (b) hydrogenated (001)-2×1 diamond surface. The green and red colour indicate to occupied and unoccupied states. The lines and the shaded regions represent the band structure of surface slab and the bulk, respectively. The zero of the energy scale is the vacuum level of the system.

Hydrogenation of the (001)-2×1 clean surface forms three C$-$C single bonds and one C-H bond with each surface carbon. The optimised bond length of hydrogenated C$-$C dimer is $1.62\,\text{Å}$, where this value agrees with the value of $1.6 \pm 0.05\,\text{Å}$, obtained by low-energy electron diffraction and previous theoretical studies [58,178]. The C$-$C bond length of the middle of the slab is $1.54\,\text{Å}$, which are equal to those found in the bulk diamond.

The band structure for clean and hydrogenated (001)-reconstructed diamond surfaces are modelled and they are illustrated in figure 5.10. The significant features of (001)-2×1 clean surface are the existence of occupied and empty surface states asso-

ciated with bonding (π) and anti-bonding (π^*) p orbitals of the surface dimer. These states lie just above the valence band maximum at around the mid-gap, respectively. Forming π-bonded surface, for (001)-2 $\times$ 1 surface gives a larger energy stabilisation from 3.5 to 2.01 eV compared to that of the Pandey chain reconstruction from 2.27 to 1.27 eV. Also, the splitting of the surface states at Γ point is about 2.6 eV which is in accord with previous calculations [2].

The band structure of (001)-2 $\times$ 1 hydrogenated surface has the same similarity as in (110) and (111)-1 $\times$ 1 hydrogenated surfaces, where hydrogenation of the surface removes the π and π^* states from the band gap and dimer bonds at the surface change from double π to single σ bonds as shown in figure 5.10(b). Also, it introduces unoccupied states beneath the bulk conduction band around Γ point. Furthermore, the band states were moved upward by 2.6 eV from their positions with the clean surface which is consistent with previous LDA calculations.

The electron affinity for (001)-2 $\times$ 1 clean surface is calculated to be +0.64 eV, where the energy level lies above the minimum conduction band as shown in figure 5.10 (b). This result is consistent with the value of +0.69 eV, obtained in previous calculations in which 10 layers slab were used [153]. Also, hydrogenation of (001)-2 $\times$ 1 surface gives rise to NEA with the value of -2.07 eV which very well agrees with other self consistent LDA calculations [58, 185] and is of similar magnitude to the -1.3 eV found in experiment [123]. The calculated value is almost the same as for (111)-1 $\times$ 1 surface and lower the NEA value for (110). The canted (001)-1 $\times$ 1 hydrogenated surface has a NEA with the value of -2.38 eV.

5.4 Conclusions

`AIMPRO` has been employed to investigate the structural and electronic properties and surface energies for low index diamond surfaces. The reconstruction and structural properties for the three surface orientations are in accord with previous DFT studies. Energetically, the (111)-2 $\times$ 1 clean surface has the lowest energy compared to other

surfaces. Hydrogenation of the surfaces reduce the surface energy due to removing the dangling bonds and dimers, where (110)-hydrogenated surface has the lowest energy. H-adsorption energies on all the three surfaces are larger than the molecular binding energy per atom of the hydrogen molecule which is 2.45 eV per atom, and they are sufficiently high to allow for a dissociative adsorption of molecular hydrogen (H_2). The structures in present study that consist of 12, 14 and 16 layers for (110), (111) and (001) surfaces, and their surface energies are satisfactory to study the preferential alignment of defects in CVD diamond energetically. The (110), (111) and (001) hydrogenated diamond surfaces will be used in the following chapters to study the polarisation of some nitrogen-related centres, and other defects.

Chapter 6

Atomistic modelling of the polarization of nitrogen centres in diamond due to growth surface orientation

6.1 Introduction

Although boron is present in relatively rare natural diamonds, it is readily incorporated in synthetic material, where it can produce p-type, metallic [97, 168], and even superconducting samples [24, 102]. More commonly seen in natural diamond than boron, and also easily incorporated in synthetic material, is nitrogen. Indeed, the incorporation of nitrogen has a large effect on the structural and morphological properties of chemical vapour deposition (CVD) diamond, and relatively low concentrations of nitrogen in the gas phase can significantly affect growth rates [7, 96, 187].

In as-grown CVD diamond the most common form adopted by nitrogen is the single substitutional centre (N_s), which is labelled the P1 centre when observed in electron paramagnetic resonance (EPR) and the C-centre as seen in infra-red absorption. N_s is a deep donor, with an ionisation energy [52] of around 1.7 eV, too large to be usefully electrically active at room temperature. The deep donor behaviour may be traced to a structural rearrangement [20, 22, 48, 98, 100, 118], so that one of the four N–C bonds

is extended by 30-40%, forming a C_{3v} symmetry center with two states in the band-gap: the N lone-pair state lies a little above the valence band, and in the upper half of the band-gap a state associated with the carbon radical formed by the extension of the N–C bond is half filled. In the positive charge state, nitrogen is isoelectronic with carbon, and N_s adopts an on-site, tetrahedral geometry. N_s may also act as an acceptor [99,173], with the electron being localised at the unique carbon site, resulting in a lone-pair on the carbon and an even greater degree of dilation.

Another frequently observed form of nitrogen in as-grown CVD diamond is the nitrogen-vacancy (NV) centre, either by growing in as a unit, or by N_s trapping mobile vacancies. NV may also be formed by post-growth irradiation and heat-treatment of diamond containing N_s: irradiation creates vacancies in the diamond, which become mobile at ∼800 K, which then become trapped adjacent to the immobile nitrogen impurities [36,43], with a theoretical [68] binding energy of 3.3 eV. In the neutral charge state, NV is identified [127] by a zero-phonon line at 2.156 eV, but the arguably more interesting negative charge state emits [78] at 1.945 eV. Previous density functional theory (DFT) calculations using a very similar methodology to that employed in the current study predict [71] donor and acceptor levels for NV at $E_v + 1.5$ eV and $E_c - 3.3$ eV, respectively. More recent studies employing more advanced computational techniques also place a donor level a little above the valence band top and a mid-gap acceptor level [128, 179], lending support to the approach we have adopted. Experimentally the acceptor state lies at 2.58 eV from a band edge, as estimated from a photo-ionisation threshold around 480 nm [163]. The negatively charged centre has a spin-triplet ground state, which has recently been exploited for quantum-state based applications including quantum computing and encryption [95,182], magnetometry [9, 10, 39, 125, 164, 167], and magnetic-field based sensing [42].

In addition to the formation of NV centres in CVD grown diamond, a complex of NV with a single hydrogen atom has also be an identified [61, 65, 109]. It is not seen in natural diamond, and is thought to exist in the negative or neutral charge states [65, 67, 109, 138]. The NVH centre is seen in EPR as a $S = 1/2$ defect (the

negative charge state), but with C_{3v} symmetry, which can be explained by the rapid reorientation of the hydrogen between the three carbon radicals [65, 108, 156].

In addition to the composition of these important defects in CVD diamond, both vacancy-containing centres are grown into diamond with a non-random populations of the various symmetrically equivalent orientations [46]. In (110)-oriented substrates, the centres are preferentially aligned in two of four ⟨111⟩ directions with equal probability, and do not appear in the other orientations at all.

Typically, diamond CVD takes place in the 700–1000°C range, with the samples used in the experimental identification of polarisation being in line with this practice [46]. Importantly, there is a wealth of observation regarding the migration of N_s and NV centres, with temperatures far above those used in CVD being required. For example, the process by which N_s aggregates into pairs is activated by around [51] 5 eV, and NV centres typically begin to migrate at high temperatures, annealing out above [32] around 1500°C. It is generally believed that NV centres migrate via a mechanism which involves its reorientation, so that both reorientation and migration are insignificant in as-grown CVD diamond. NVH is also thermally stable [109], annealing out well above growth temperatures, being in excess of 2000 K. In contrast, as mentioned above monovacancies migrate even at low growth temperatures. In the light of the relative mobility of monovacancies, and immobility of N_s, NV, and NVH, the model for the incorporation of these centres takes on more significance in the light of the polarisation: it is implausible that a migrating vacancy would always result in the same polarisation, so NV and NVH centres must grow in as units. The proposal [46] is that the N atom is fully chemically bonded into the surface first, and that the subsequent layer of diamond grown over the (110) layer containing the nitrogen occasionally leaves a vacant site above it.

Although the mechanism seems plausible, it requires direct quantitative analysis, which is extremely challenging to obtain directly from the experiment. In contrast, atomistic, quantum-chemical modelling can provide immediate insight into the processes, allowing for the proposed mechanism to be evaluated. A detailed under-

standing of the processes involved may in turn provide a route to optimisation of the incorporation or exclusion of such point defects, and furthermore provide further insight into the processes underpinning diamond growth and perhaps ultimately clarify the role of impurity incorporation within surface morphology and diamond growth rate.

Therefore we have performed a density functional theory analysis of N_s, NV, and NVH centres in diamond, and investigate the polarisation of these defects with respect to not only the (110) H-terminated surface for which polarisation of these centres has been observed, but also (111) and (001) surfaces to place the (110) surface energetics in context. We first outline the methodology.

6.2 Method

The structure of defects and the method that used in this study are as described in chapters 2 and 4. In addition, the N atoms are represented by basis sets made up from independent sets of s, p, and d functions with four widths (constituting 40-functions per atom) and H by three widths of s and p functions (16-functions per atom). The Brillouin zone sampling 3×3, 3×3, and 4×3 meshes were used for the (110), (111), and (001) surfaces, respectively. The convergence of the total energy with respect to the sampling was established less than 5 meV. For the reference P1 centre, as $2 \times 2 \times 2$ sampling scheme was used as described in section 4.2.

Diamond surfaces have been simulated using the standard slab-geometry approach, with the base unit cells as detailed in table 6.1. To study N_s, NV, and NVH centres in the three diamond surfaces, the nitrogen atom was placed in each of the upper six, seven, and eight layers of the (110), (111), and (001) diamond slabs, respectively, as illustrated in figure 6.1. In each case there are multiple defect orientations relative to the surface normal, all of which have been included in the analysis. For example, for N_s in the (110) surface, there are three distinct orientations: [111], $[\bar{1}\bar{1}1]$, and either $[\bar{1}1\bar{1}]$ or $[1\bar{1}\bar{1}]$ directions, which are equivalent.

Table 6.1: Surface lattice vectors in units of a_0, composition, and number of atomic layers of carbon (n) in the slab supercells used in this study.

Orientation	$\vec{v_1}$	$\vec{v_2}$	Composition	n
(110)	$3[110]/\sqrt{2}$	$2[001]$	$C_{144}H_{24}$	12
(110)	$4[110]/\sqrt{2}$	$3[001]$	$C_{288}H_{48}$	12
(111)	$3[1\bar{1}0]/\sqrt{2}$	$3[10\bar{1}]/\sqrt{2}$	$C_{126}H_{18}$	14
(001)	$4[110]/\sqrt{2}$	$3[1\bar{1}0]/\sqrt{2}$	$C_{192}H_{24}$	16

For a reference calculation, the P1 centre was simulated in a 216-atom supercell ($C_{215}N_1$) made up from $3 \times 3 \times 3$ conventional, 8-atom unit cells.

Optimisation of the structures is performed using a conjugate gradients scheme. In determination of the equilibrium structures, all atoms were allowed to move. The impact of whether the bottom surfaces of the slabs was fixed or relaxed during optimisation was assessed, and total energies found to be independent of this choice. For instance, the N_s has been modelled in (111) diamond surface structure as a function of depth with fixing the bottom four layers and the rest layers are allowed to move, calculate the total energy and compare them to those structures with all the atoms allowed to move. The results as reported in table 6.2 show that there is no significant difference between them.

For activation energies, the climbing nudged elastic band (NEB) method has been used [79, 80].

In order to allow comparison between different surface orientations, and between defects comprised from different numbers of atoms, it is necessary to evaluate formation energies, which may be calculated for a system X using

$$E^f(X) = E^{\text{tot}}(X) - \sum \mu_j, \tag{6.1}$$

where $E^f(X)$ is the formation energy, $E^{\text{tot}}(X)$ is the total energy, and μ_j are the chemical potentials of the atomic species, respectively. Since we are primarily

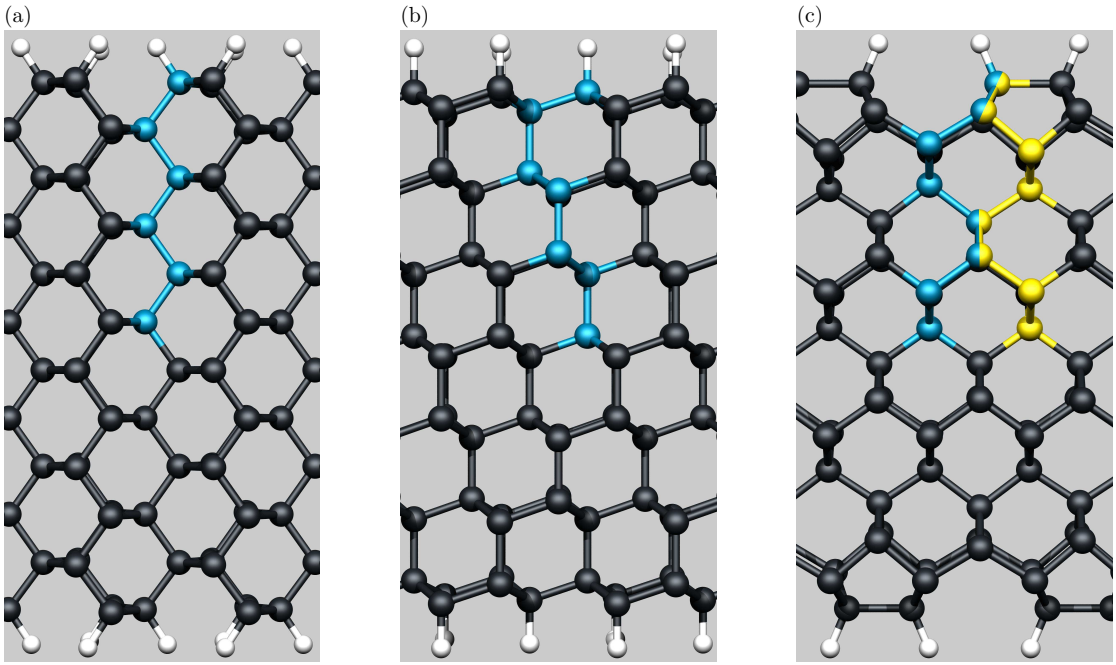

Figure 6.1: Schematics of the H-terminated (a) (110), (b) (111), and (c) (001) diamond surfaces slabs. Black and white spheres indicate C and H, respectively, with the blue sites indicating the range of sites in which N has been substituted. For the (001) surface, the yellow spheres indicate the alternative line of sites in the slab, as described in the text. For the three slabs, the surface normals are vertically up, with the projections being in the (a) $[1\bar{1}0]$, (b) $[\bar{1}10]$, and (c) $[1\bar{1}0]$ direction, and the horizontal directions being (a) [001], (b) $[11\bar{2}]$, and (c) [110], respectively.

interested in the energy differences of the point defects in different locations, it is important that we exclude contributions to the formation energy due to the different surfaces, so an alternative approach has been adopted. The formation energy of the defect alone may be obtained

$$E^f(X) = E^{\text{tot}}(X) - E^{\text{tot}}(\text{Slab}) - \sum \mu_j, \tag{6.2}$$

where $E^{\text{tot}}(\text{Slab})$ is the total energy of the defect free slab. The chemical potentials are then defined as follows. The carbon chemical potential, μ_{C}, is the energy per atom

Table 6.2: Comparison the total energy between fixed and without fixed layers structures of N_s in (111) diamond surface as a function of depth.

Depth ($\mathring{A}$)	Fixed layers (Ha)	Moved layers (Ha)	Difference (mev)
0.000	−731.98055	−731.98056	0.3
0.490	−731.9747	−731.97471	0.3
2.042	−731.97294	−731.97308	3.8
2.558	−731.97351	−731.97355	1.1
4.106	−731.97259	−731.97265	1.6
4.623	−731.97263	−731.97269	1.6
6.171	−731.97223	−731.9726	10.0

of bulk diamond. The hydrogen chemical potential is taken to be the average energy per hydrogen atom for the three low-index surfaces explored in this study, where for the slab cell C_nH_m, the average energy is calculated as $(E^{\text{tot}}(\text{Slab}) - n\mu_{\text{C}})/m$. The nitrogen chemical potential is obtained from the condition of zero formation energy for N_s in a 216-atom bulk diamond simulation. Although this condition may be viewed as somewhat arbitrary, since all N-containing centres examined in this study contain only single N atoms, the choice of μ_{N} only defines the zero of the formation energy scale, and has no impact upon formation energy differences. In addition, this condition gives a convenient immediate comparison for the energies relative to a relatively common defect centre.

Finally, for electrical levels, it would also be necessary to take into account the impact of the Fermi-energy, and to include energies of charged defects. Formation energies for charged supercells include terms [113] of the form $q(E_v(X,q) + \mu_e)$ and $\chi(X,q)$, where q is the charge state, $E_v(X,q)$ is the energy of the valence band top for the system X, and $\chi(X,q)$ represents a correction for periodic boundary conditions, typically including terms in charge and multipole interactions. However, in this study,

we are only interested in the *relative* locations of the levels at various sites with respect to the surface, and under the approximation that the additional terms in the formation energies are largely systematic, we only present donor and acceptor level *differences* in this paper, where the contributions from the periodic boundary condition error, and location of the Fermi-energy play no role.

6.3 Results

N_s, NV and NVH centres have been modelled on and below (110), (111) and (001) diamond surfaces as a function of depth, with the N-components of the defects as shown schematically in figure 6.1. As mentioned in section 6.2, the defects were modelled in all orientations, and we present the results of the simulations organised in the following way. We first present the results for the simple substitutional nitrogen centre for each surface orientation, including the impact of the proximity of the surface upon the structure, orientational anisotropy, energetics and electrical levels. We then repeat a similar analysis for NV and NVH centres, before making comparison between the three forms of N-containing defects, including the energetic basis for the existence of polarisation in (110) grown samples.

6.3.1 N_s centres

figure 6.2 shows the formation energies as a function of depth, including the various orientations of the broken bond.

Figure 6.2(a), represents the data for the (110) surface. When N_s is in the uppermost carbon layer there are essentially three possibilities. A bond may be broken in line with the P1-EPR centre in two ways; either a bond within the plane of the surface (*i.e.* either $[1\bar{1}1]$ or $[\bar{1}11]$) or one *into* the surface along $[\bar{1}\bar{1}\bar{1}]$. The relative formation energy between these two cases is independent of the atomic chemical potentials, and the latter form is found to be energetically favoured by around 0.6 eV.

The third option involves removal of the H-atom along [111] (the natural conse-

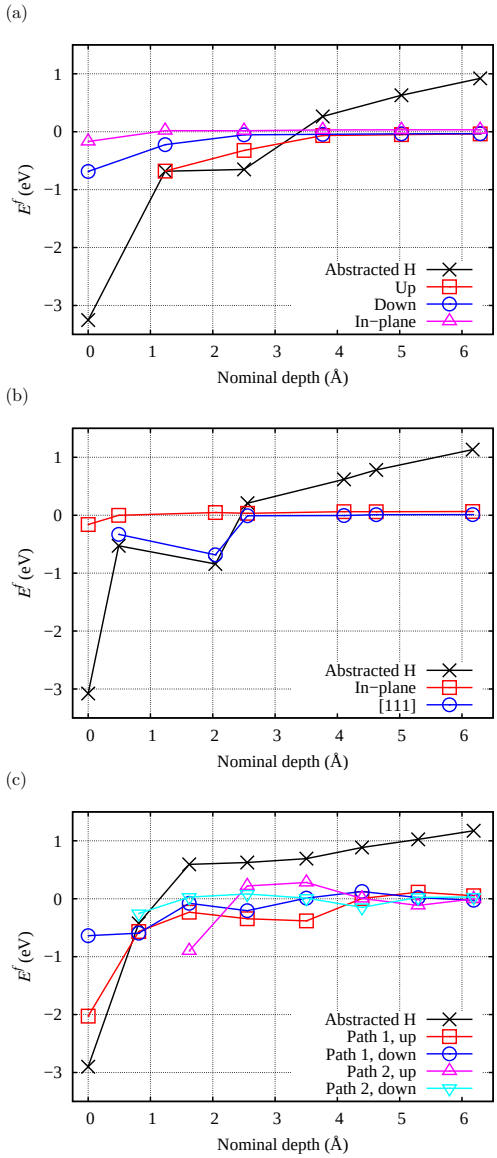

Figure 6.2: Formation energy of N_s in (a) (110), (b) (111), and (c) (001) diamond surfaces as a function of depth of the carbon site in pristine diamond (figure 6.1), as specified by equation 6.2. In each case, "up" and "down" refer to the polarisation of the dilated N–C bond relative to the N atom, with respect to the surface plane. For the (111) system, the circles represent polarisation parallel to the surface normal, and for the (001) surface, the two paths are as shown in figure 6.1. "Abstracted H" refers to structures where a hydrogen atom has been removed from a surface site above the nitrogen.

quence of a 'broken bond' out of the surface), resulting in a completely chemically satisfied system. This differs from the other two forms in composition (there is one fewer H atom), and the relative formation energy thus depends upon μ_{H}. Using the chemical potentials defined in section 6.2, E^f for N_s at the surface with a H-atom removed is $-3.3\,\mathrm{eV}$, some 2.6 eV below that of the P1-like structure polarised into the surface. Despite it being significantly more stable at the surface, removal of a surface H-atom is much less favourable where the N is buried deep within the diamond. Such structures can be viewed as a carbon radical at the surface accepting an electron from the N-donor, forming a lone-pair at the surface and an ionised P1-centre in the diamond. The energy of such an arrangement rapidly increases, and is only of any significance for N in the first three atomic layers of carbon.

For the P1-like structures, polarisation within the (110) plane is generally less favourable than the alternatives, a consequence of the relative ease with which strain is accommodated by displacement normal to the surface. Figure 6.2 shows that beyond the third layer (*i.e.* beyond just $\sim$3 Å), the formation energies of the P1-like structures converge to zero to within a few 10s of meV. The approach to zero is a consequence of the definition of μ_{N}, with the small variations ascribed to anisotropy in the supercell approximation. We have calculated sample structures in a supercell with the larger surface area and for P1-like structures in the core of the slab the formation energies differ from zero by just 30 meV. Also, table 6.3 shows the comparison of formation energy between the the large and small surfaces for selected P1-like structures in different depths. The structure of N_s in (110) surface at the sixth layer and the bond is broken in the plane is larger than the other structures due to the large interaction between the defect and its image in the direction parallel to the plane surface.

The variation in energy in the first few layers is also associated with changes in geometry. The length of the broken bond, plotted in figure 6.3(a), increases with decreasing energy; in cases such as N in the second layer and the radial in the first layer where the energy is relatively low, this effect is clear with the N–C distance being 30% greater than the value in bulk diamond.

Table 6.3: Formation energy comparison between the large and small surface areas of selected structures for N_s in (110) surface with different depths.

Depth ($\AA$)	Large surface (eV)	Small surface (eV)	Difference (meV)
1.236	−0.678	−0.680	2.7
5.028	−0.045	−0.050	4.9
6.292 (up)	−0.029	−0.037	8.2
6.292 (in plane)	0.003	0.033	30

The final aspect we review is the variation in electrical behaviour with depth. In order to determine the donor and acceptor levels, positively and negatively charged N_s have also be optimised for each position. A determination of the location of the levels within the band-gap is not the focus of this study, but rather the change in the location as a function of depth. We have therefore calculated differences in the ionisation energies and electron affinities relative to those at the deepest sites available in the simulations. The results for the (110) surface are plotted in figure 6.4(a). Where N_s is four or more layers into the diamond, the donor and acceptor levels are constant to within computational uncertainties. The splitting in the levels for different orientations arises from the finite in-plane interactions between the periodic images. However, they are much smaller than the variation in the electrical levels as a function of depth, and do not affect our conclusions.

There are some interesting effects resolved in the electrical levels in the close surface region. First, the donor level is significantly deeper (further from the conduction band minimum), which reflect the extra dilation of the unique N–C direction (figure 6.3(a)) afforded by the relatively less constrained surface. It is also possible to see by comparing with figure6.2(a) that the deeper levels correspond to the more stable orientations and depths, as one might expect.

We now turn to the (111) surface, for which the energetics are illustrated in figure

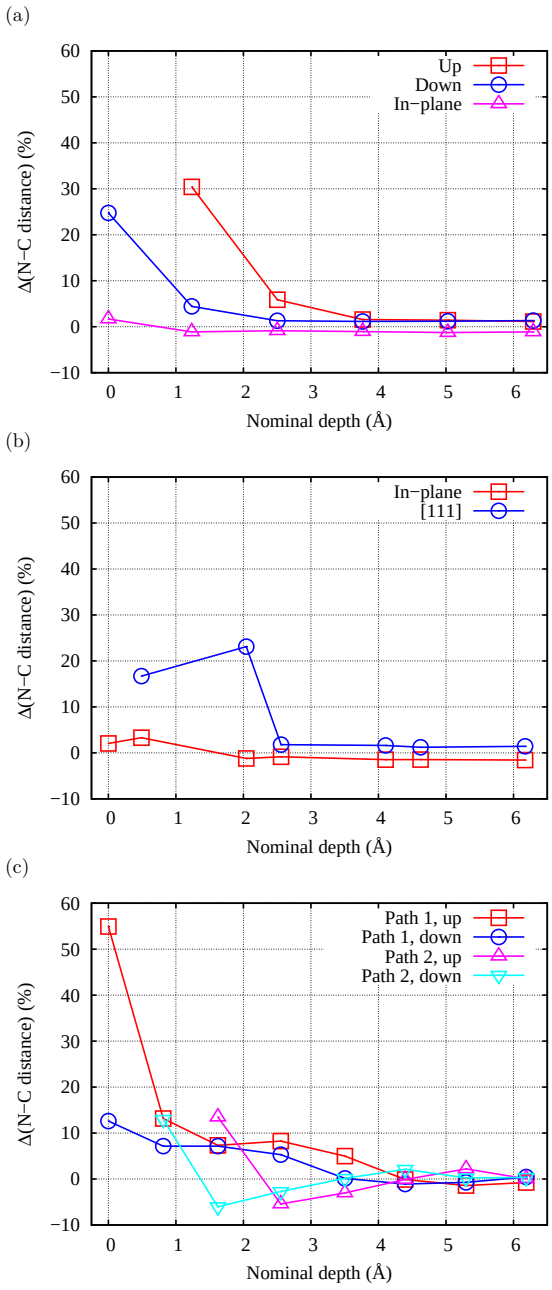

Figure 6.3: Fractional difference in the distance between the nitrogen and radical carbon atoms relative to the value calculated for P1 in bulk diamond for (a) (110), (b) (111), and (c) (001) diamond surfaces and as a function depth. Symbols follow the definition in figure 6.2.

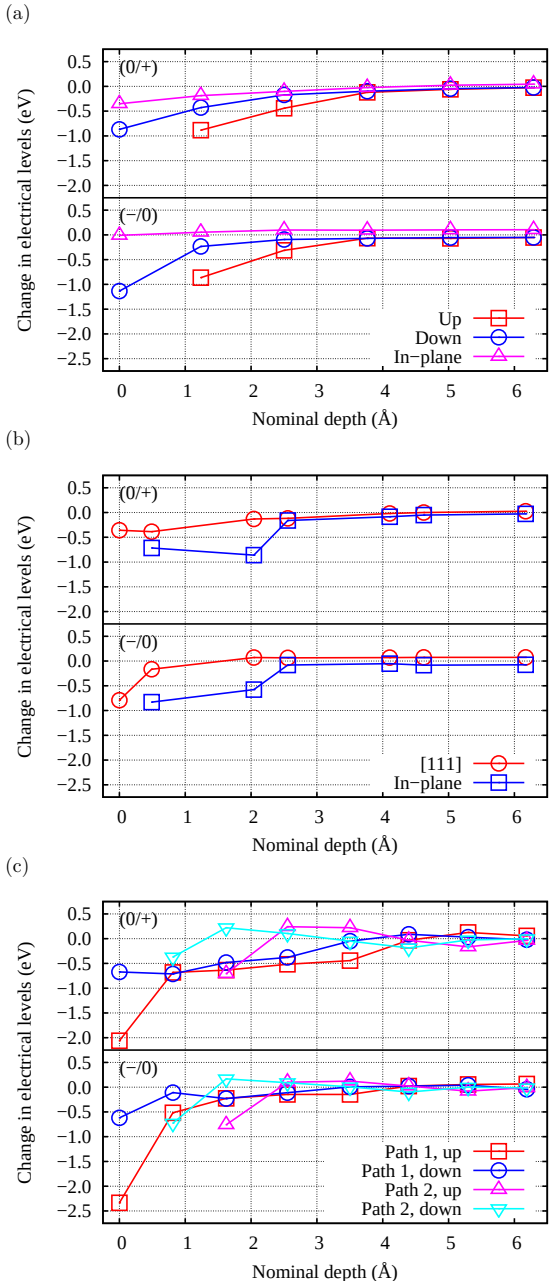

Figure 6.4: Calculated changes in donor (labelled (0/+)) and acceptor (labelled (−/0)) levels for N_s in (a) (110), (b) (111), and (c) (001) diamond surfaces and as a function depth. A positive change indicates that the level is moving upward in energy, away from the valence band top. Symbols follow the definition of figure 6.2.

6.2(b). As with the (110) surface, the scope for relaxation at the surface is reflected in the energies: N_s at the surface with a H-atom removed is by far the most energetically favourable structure. This structure is shown in figure 6.5(b). In addition, for N_s in the *third* layer and the broken bond along [111], the unique carbon site is able to relax significantly (figure 6.3(b) and 6.5(d)), becoming approximately co-planar with the three carbon neighbours in the upper-most layer. Such structures are 0.8 eV lower in energy than P1-centres located in bulk diamond. The intermediate, second layer site is relatively less stable, due to the constrained environment for the carbon radical site (figure 6.5(c)).

Finally, we turn to the (001) surface, with the energetics presented in figure 6.2(c). They follow the pattern of the other two surface orientations, with N in a surface site being energetically most favourable. Another relatively low energy structure with N in the surface layer may be generated by retaining the H atom but breaking the reconstruction along [110]. The resulting N–C separation is approximately the host second-neighbour distance (figure 6.3(c)). The formation energy just 0.9 eV higher than the chemically satisfied system with a hydrogen atom removed.

Unlike the (110) and (111) surfaces, there is more than one site in each atomic layer (it may be either under a reconstruction or a trough), so that there are many more non-equivalent sites and orientations to consider in the (001) case. In the third, fourth, seventh, and eighth layers there are two distinct sites, but in each case there are only two orientations (either polarised with a component toward the surface, or away from it), whereas in the first, second, fifth, and sixth layers there is only one site, but three orientations are non-equivalent. Thus there are either three or four configurations at each depth, all of which have been considered. Below around 4 Å, the effect of the surface is no longer resolved in the calculations.

It is helpful at this stage to make some general observations across all three surfaces. Despite the variation in the details of the properties of N_s in the different surfaces, there are many similarities, and the impact of the surface is lost beyond 3–4 Å. The most favourable location of nitrogen is at the very surface, with N_s substi-

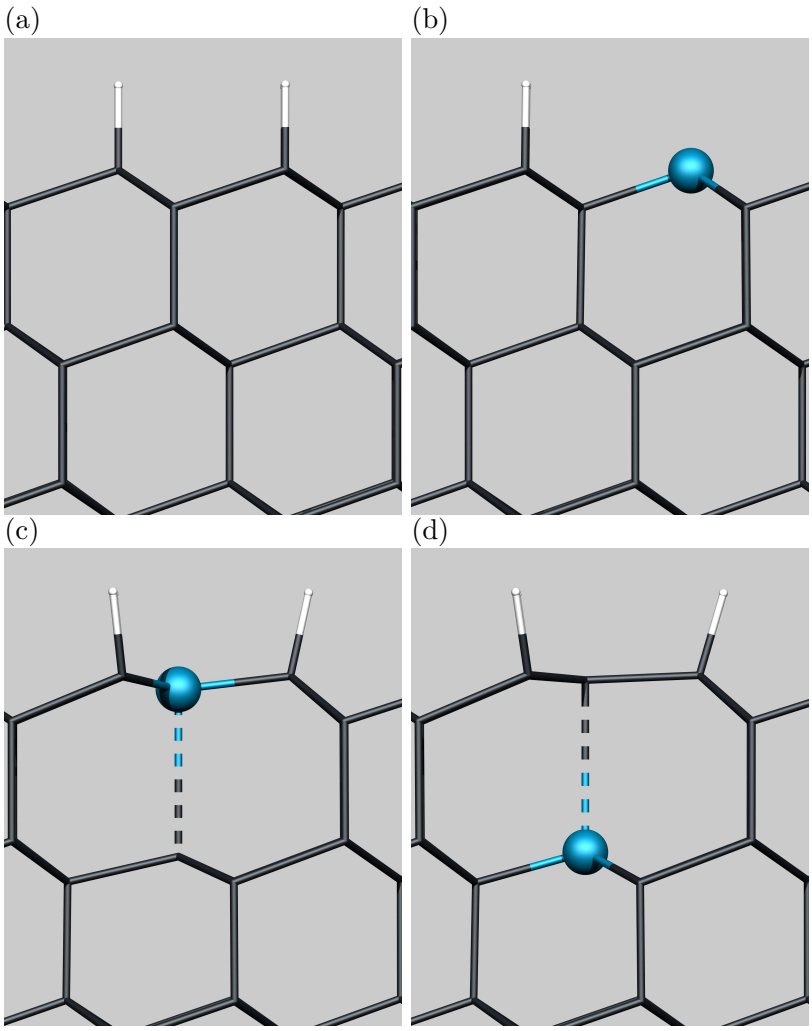

Figure 6.5: Schematics of the structures of N_s in the (111) surface. (b)-(d) show the lowest energy forms for the first to third layers, respectively, with (a) being the corresponding defect free section, for comparison. Colours are as in figure 6.1. [111] is vertically up, with the projection and horizontal direction being $[\bar{1}10]$ and $[11\bar{2}]$, respectively.

tuting for a C–H group. Such arrangements as calculated using the chemical potentials for the atomic species as defined in section 6.2 are 2.9–3.2 eV lower in energy than a fully hydrogenated surface with a neutral P1 centre buried within the diamond slab.

6.3.2 NV centres

We now turn to the case where N_s captures a lattice vacancy. As with N_s, NV contains a three-fold co-ordinated nitrogen atom with a lone-pair pointed toward the centre of the defect, but NV contains three rather than a single carbon radical, resulting in a degenerate state around mid-gap. This in turn is responsible for the three lowest many-body states of the defect when in the negative charge state [74]. However, when close to the surface of the diamond, the lowering of the symmetry results in a raising of this degeneracy [139], and where the defect is in the upper most layer, it may well be expected that even the number of dangling bonds will differ. As with N_s, we start with the results for the (110) surface, and the calculated formation energies as a function of depth are plotted in figure 6.6(a).

Variation in formation energy with position is only significant in the upper most three layers. Where nitrogen is in the upper most layer and the vacancy is adjacent to it (*i.e.* also in the upper most layer), two of the three dangling bonds are eliminated. The structure (figure 6.7(d)) has a calculated formation energy of $-1.2\,\text{eV}$. Where nitrogen is in the second layer and the vacancy is in the first, again only one dangling bond remains (figure 6.7(c)) with a correspondingly low formation energy of $-0.9\,\text{eV}$. Thus we find that the orientation of NV centres within the (110) growth plane are thermodynamically more favourable than out of the surface. In other words, based upon NV formation energies, it appears that the preferential orientation of NV centres out of the surface in (110) grown diamond cannot be explained. However, we shall show in section 6.3.4 that this is not the case.

The favourable formation energy of the NV centres is only present in the upper two layers in the (110) surface. For NV incorporated deeper within the diamond, it cannot be formed with fewer than three dangling bonds.

NV may exist in the negative charge state, and in figure 6.8, the variation in the acceptor level with location is plotted. Based upon an acceptor level around mid-gap, all locations of NV within the (110) surface remain acceptors, the electrical level being generated by the presence of at least one carbon radical.

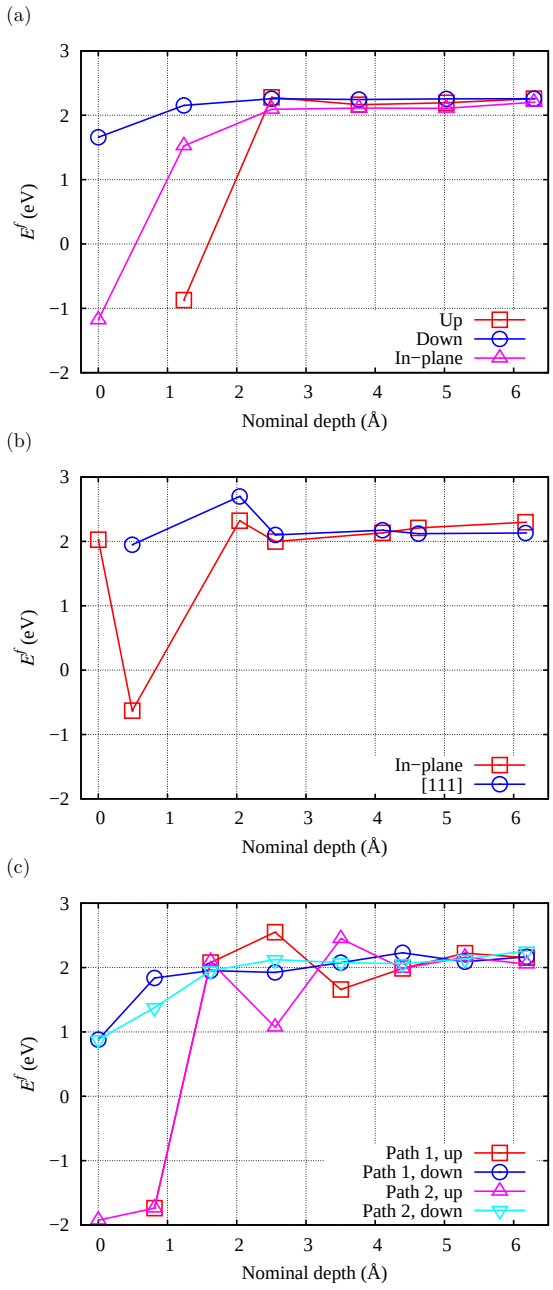

Figure 6.6: Formation energy of NV in (a) (110), (b) (111), and (c) (001) diamond surfaces as a function depth of the carbon site in pristine diamond (figure 6.1), as specified by equation 6.2. Symbol and labels follow the definitions in figure 6.2.

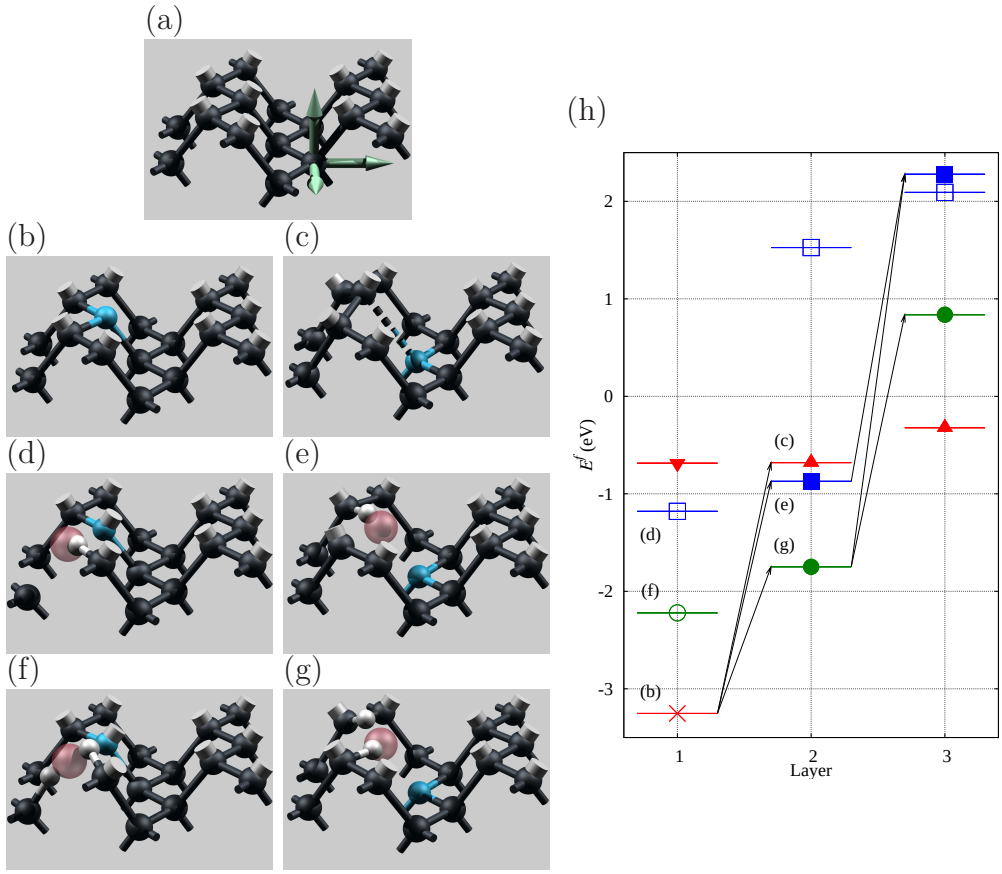

Figure 6.7: Schematic perspective structures of N_s, NV, and NVH in the (110):H surface. Black, blue and white spheres represent C, N, and H, respectively, with red, translucent spheres indicating the vacancy. For clarity, surface H are not plotted but their direction is indicated by white stumps. (a) shows a section of defect free surface, with arrows indicating the [001] (right) [$\bar{1}$10] (out of the page) and [110] directions. (b), (d), and (f) show N_s, NV, and NVH where N lies in the upper most carbon layer, and (c), (e), and (g) show the same centres in the second layer. (h) shows a plot of the calculated formation energy for the upper most 3 layers. Circles, triangles and squares indicate N_s, NVH, and NV, respectively. For N_s the filled symbol indicates that a H atom has been removed, whereas for NV and NVH the filled symbol indicates polarisation of the centres out of the surface. Labelling in (h) indicates associated structures depicted, and the arrows indicating possible production paths are explained in the text.

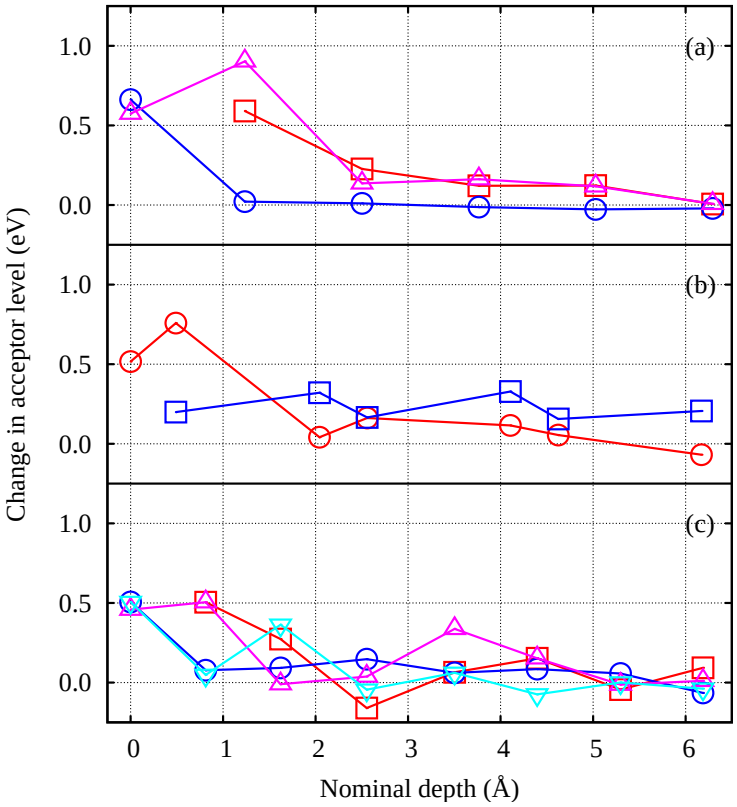

Figure 6.8: Calculated changes in acceptor level for NV in (a) (110), (b) (111), and (c) (001) diamond surfaces and as a function depth. A positive change indicates that the level is moving upward in energy, away from the valence band top. Symbols follow the definition in figure 6.2.

The dramatic formation energy variation seen for the (110) surface is also present in the other two surfaces (figure 6.6(b) and (c)). In the (111) surface with N in the second layer, and the vacancy in the first a single dangling bond is present, leading to a formation energy of $-0.6\,\text{eV}$. Similarly, for the (001) surface sites in the upper layers may result in a single radical, and it is in this surface orientation that the formation energy of the NV centre has the lowest value determined of the three low-index surfaces examined in this study. Where N lies in either the first or second layers, and the vacancy lies in the upper most carbon layer, the formation energies reflect that there is only one radical carbon site, being between $-1.9\,\text{eV}$and $-1.5\,\text{eV}$.

These structures are 0.3–0.7 eV lower in energy than the most favourable form on the (110) surface, and 0.9–1.2 eV lower in energy than the (111) surface. The differences seen here for the energies as a function of surface orientation is in line with previous studies [114], where the energies of substitutional impurities were found to exhibit similar variations.

Overall, the formation energies of NV centres in the diamond surfaces are much higher than the corresponding N_s defects. Both forms of nitrogen share the substantial stabilisation in the upper most carbon layer due to the removal of dangling bonds, which requires the removal of a hydrogen atom in the case of N_s. The relative energies of N_s and NV shall be returned to in section 6.3.4, but first we move the hydrogen decorated NV centres, NVH.

6.3.3 NVH centres

The formation energies as a function of depth for NVH are plotted in figure 6.9. The introduction of hydrogen to the NV centres lowers the symmetry of the centre in bulk diamond, increasing the number of possible orientations. However, it is known that the hydrogen atom can readily reorient between carbon sites, and to simplify the graphical presentation, we include only the energies for the most favourable location of the hydrogen for each orientation of the underlying NV centre.

The energy profiles resemble in shape those of NV plotted in figure 6.6, but are offset downward in energy by 0.5–1.0 eV, the reduction due to there being fewer radicals in all layers.

For the (110) surface, NVH has the lowest energy with nitrogen in the first layer and the vacancy in the same layer (figure 6.7(f)), having a formation energy of -2.2 eV. Then, with nitrogen in the second layer and the vacancy in the first (figure 6.7(g)) the energy rises to -1.7 eV. As with the case for the undecorated NV centre, this suggests that on a simple basis of formation energies a polarisation within the growth plane would be preferred, at odds with the observed polarisation. We shall return to this issue in section 6.3.4.

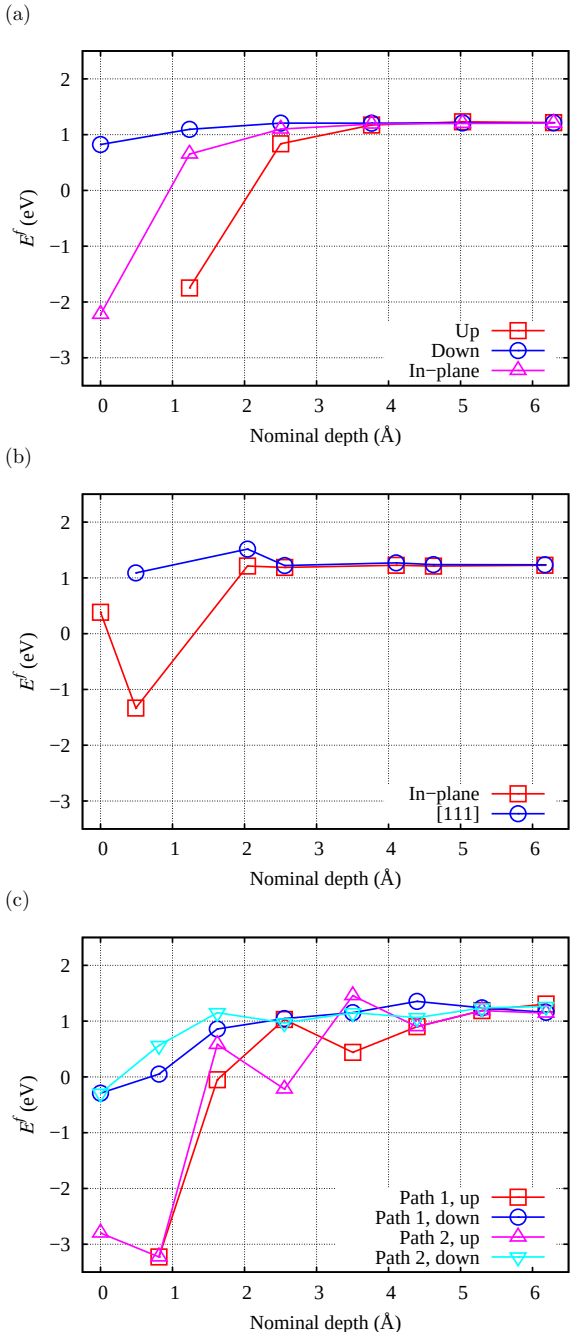

Figure 6.9: Formation energy of NVH in (a) (110), (b) (111), and (c) (001) diamond surfaces as a function depth of the carbon site in pristine diamond (figure 6.1), as specified by equation 6.2. Symbol and labels follow the definitions in figure 6.2.

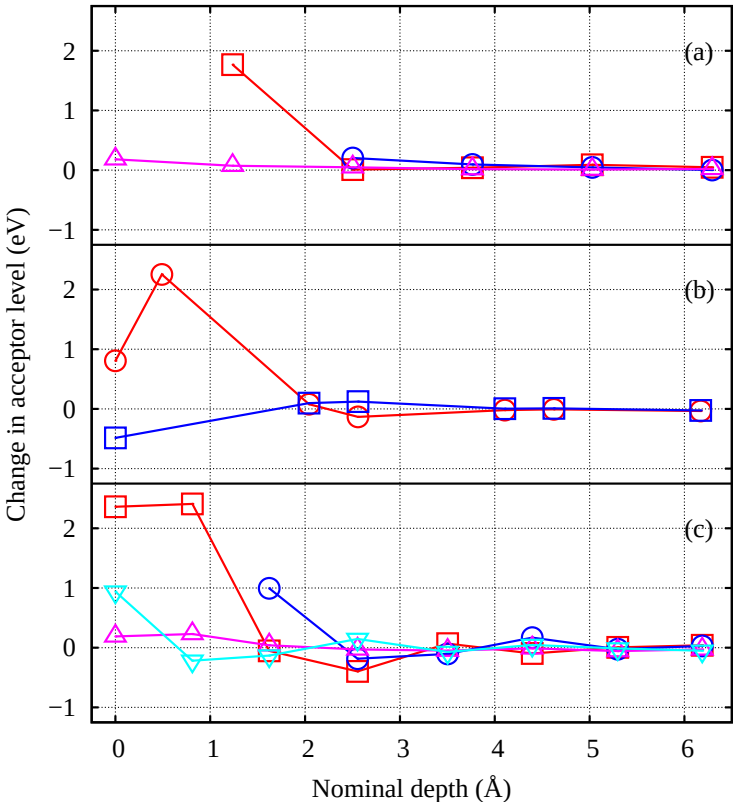

Figure 6.10: Calculated changes in acceptor level for NVH in (a) (110), (b) (111), and (c) (001) diamond surfaces and as a function depth. A positive change indicates that the level is moving upward in energy, away from the valence band top. Symbols follow the definition in figure 6.2.

There is a relatively small reduction in formation energy with the addition of hydrogen for NVH in the upper layers of the (111), and for the (001) surface NVH is very stable, with the most favourable formation energy of any surface examined in this study. The lowest energy of NVH arrangement places nitrogen in the second layer with the vacancy in the first, with a formation energy of −3.5 eV, but with both components in the first carbon layer, the formation energy is still very low at −3.0 eV.

In terms of the electrical properties, it is known that NVH has an acceptor level when in bulk diamond, but at the surface, where there are no carbon radicals, the acceptor level is moved by around 2 eV toward the conduction band (figure 6.10),

a much greater effect than calculated for NV (figure 6.8). Indeed, it is likely that this shift reflects an absence of an acceptor level in the cases where there are no unsaturated carbon atoms.

6.3.4 N_s, NV, and NVH and the origin of polarisation

Starting with the (110) surface, where the incorporation of NV and NVH centres has been shown in experiment to be 100% polarised involving with trigonal axes of the centres along [111] and [11$\bar{1}$], and none along [1$\bar{1}$1] or [$\bar{1}$11]. This means that the vacancies and N atoms lie in different (110) planes. As shown in section 6.3.2 and section 6.3.3, the calculated formation energies seem to imply that [111] and [11$\bar{1}$] orientations are energetically less favourable, in apparent contradiction with the observations. However, these energies compare only the orientations preferred under thermodynamic equilibrium, and take no account of the sequence of events that lead to the incorporation within the lattice.

Since isolated lattice vacancies are mobile at growth temperatures, it seems most probable that in a stepwise formation process the nitrogen atom is incorporated first, and the vacancy second, during the formation of either NV or NVH. Indeed, there is some support in our calculations for such a picture in the energies of the structures where nitrogen is in the upper-most layer of the diamond, and a vacancy lies in the second layer. For both NV and NVH centre in all three surfaces, incorporation of vacancy before the nitrogen atom results in a much higher energy configuration than the reverse (figure 6.6 and 6.9). For example, in the (110) surface, nitrogen in the first carbon layer and a vacancy in the second has a calculated formation energy of around +1.7 eV (circle at a nominal depth of zero, figure 6.6(a)), whereas for the two components in the reverse order has a formation energy of around −0.9 eV (square at a nominal depth of 1.2 Å, figure 6.6(a)), a difference of 2.6 eV.

If we assume that order of incorporation of the two components is correctly described as nitrogen followed by the vacancy, by far the most stable form for the initial stage of incorporation of substitutional nitrogen is N in the surface layer with no

hydrogen bonded to it (figure 6.7(b)). This form of nitrogen is calculated to have an absolute formation energy of around −3.2 eV. Such a defect is not only the most stable form for N_s in the (110) surface, it is also much more stable than either NV (figure 6.7(d)) or NVH (figure 6.7(f)), with formation energies of −1.2 eV and −2.2 eV, respectively. It is perhaps helpful to focus upon the number of dangling bonds in each case. N_s in the surface is completely chemically satisfied, NV in the surface has a single dangling bond, and NVH has no unsaturated atoms and is therefore chemically as stable as N_s. A key difference between N_s and NVH in the upper-most layer is the steric repulsion between the H atoms saturating the vacant site. From a statistical thermodynamics perspective, the formation energies suggest that in-plane polarised NV and NVH centres are very improbable relative to N_s.

Next, suppose that another atomic layer of carbon is deposited on the (110) surface, covering the layer containing the N atom. In terms of the calculated properties presented in sections 6.3.1–6.3.3, the additional layer of carbon means we need to consider the energetics of N in the second layer. In contrast to the case with N in the surface, where N is buried by a layer of carbon N_s is much less energetically favoured. We have considered both a simple substitution of carbon by N, resulting in a P1-like centre (figure 6.7(c)), and a structure where a nearby hydrogen atom has been removed from a carbon at the surface, resulting is an on-site, ionised nitrogen donor centre, and a surface carbon site which traps the donated electron. It turns out in our calculations that both of these structures result in a formation energy of around −0.7 eV, some 2.5 eV higher in energy than N on the surface (figure 6.7(b)).

Now, suppose the addition of a vacancy. If it is to be associated with the nitrogen lying in the second layer, then it is then expected to grow into the first layer, since a vacancy pre-existing in the diamond surface is unlikely based upon its relatively high formation energy [87] and mobility at the growth temperature. The NV or NVH resulting from the addition of a vacancy to a nitrogen atom in the second layer will be polarised "out of the surface". We find such structure to have favourable formation energies in comparison to a N_s centre buried in the second layer, being around −0.9 eV

and −1.7 eV, respectively (figures 6.6 and 6.9). This is a crucial result: this means that NV is comparable in energy to N$_s$ in the second layer, with that of NVH considerably more favourable.

Finally, it is supposed that subsequent layers will bury the NV or NVH centres, leading to the polarisation, provided that the centres are unable to reorient, which is expected to be the case based upon the calculated reorientation barriers [140] and temperatures at which the centres are found to be stable in experiment [32, 109].

Indeed, although reorientation of NV in bulk diamond is thought [140] to involve processes with a barrier greater than 5 eV, we cannot entirely exclude the possibility that there are lower energy routes between the two polarisations of, say, NV when very close to the surface layers. It has been therefore calculated the barrier to reorientation between NV shown in figure 6.7(e) and a form where the vacancy lies in the second carbon layer, adjacent to N. The forward and reverse reactions are calculated to be activated by energies of 5.0 and 4.4 eV, respectively. To estimate the time scale of NV reorientation when the nitrogen atom in the second layer at growth temperature, the relationship

$$\nu_{\text{reorient}} = \nu_{\text{attempt}} \exp(-E_{\text{reorient}}/k_B T) \tag{6.3}$$

can be used, where ν_{attempt} is the attempt frequency, E_{reorient} is the reorientation barrier, k_B is Boltzmann's constant and T is the growth temperature (900-1200 K). Taking the order of magnitude of diamond phonon frequency ν_{attempt}=10 THz, the highest growth temperature T=1200 K and the lower reorientation barrier E_{reorient}=4.4 eV, the time needed to reorient is about three days. Based upon these energies, and their consistency with the bulk reorientation/diffusion energies, we conclude it is unlikely that any reorientation of this type would take place at growth temperatures.

Combining these data, we therefore have a quantitative energy description for route to formation of both NV and NVH in the (110) surface that explains the geometric polarisation. Indeed, it is a natural consequence of these incorporation stages that both vacancy containing defects *should* be present in diamond. This will happen despite their bulk formation energies being 1–2 eV higher in energy than N$_s$, which on

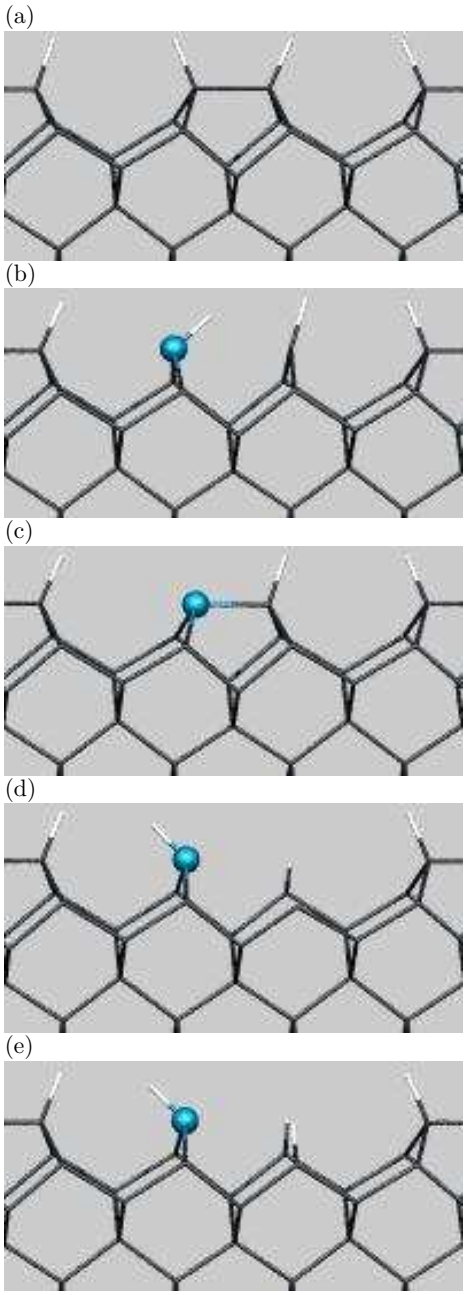

Figure 6.11: Schematics of the structures of most stable forms of (b) and (c) N_s, (d) NV, and (e) NVH in the (001) surface. (a) is the corresponding defect free section, for comparison. Colours are as in figure 6.1. [001] is vertically up, with the projection and horizontal direction being $[1\bar{1}0]$ and [110], respectively.

a simple thermodynamical basis would suggest that they should not be formed.

The energetics at each stage are summarised in figure 6.7(h), with the arrows indicating the possible steps that could take place by incremental addition of layers of carbon such that nitrogen is incorporated first, and a vacancy potentially incorporated second. The arrows exclude any sequence that would require reorientation of a vacancy containing centre, and in this case the most favourable sequences on an energy basis can only result in polarisation as seen in experiment.

Turning to (111) surfaces, a mechanism for incorporation of NV or NVH is much less clear. As with the (110) surface, initial incorporation of nitrogen seems likely to be a nitrogen substituting for a C–H group at the surface. (111) diamond growth is thought to proceed by bilayer addition, rather than the monolayer process on the (110) surface, so if nitrogen is incorporated as we suggest, one might then expect nitrogen only to appear on the odd-numbered layers in the simulations performed for this study. All NV and NVH centres with the nitrogen in odd layers (first, third, fifth...) have formation energies which are much higher than N_s, so any polarisation in the (111) growth surfaces must proceed by another mechanism.

Finally, we turn to the (001) surface. Here, there is no route to polarisation as the surface normal direction has an equal projection onto all defect orientation directions. However, as with the (110) surface, the energetics provide a route to formation of the vacancy containing centres. Initially, as with both the (110) and (111) surface orientations, the substitution of a surface C–H group by a nitrogen atom is highly energetically favourable, with a formation energy of $-3.0\,\text{eV}$. In contrast to the other surfaces, formation of NVH centres in the upper most carbon layer is comparable to N_s, with a formation energy of $-2.8\,\text{eV}$. However, this comparison has to be viewed with some caution. Figure 6.11(b)–(e) show the structures of most stable forms of N_s, NV, and NVH in the (001) surface. The low energy form of NVH can be viewed as a component of a step in the (001) surface, and might be less susceptible to encapsulation than the corresponding defects in more densely packed surfaces. Nevertheless, the formation of both NV and NVH where the N atom lies in the second layer are both

much lower in energy than N_s, and following a similar argument to that proposed for the (110) surface, this provides a mechanism for the growing in of these relatively high-energy defects.

6.4 Conclusions

N_s, NV, and NVH centres in the first few layers of (110), (111), and (001) surfaces have been modelled to investigate their energetics. The results for the (110) surface have provided a clear guide to the mechanism of incorporation of the vacancy containing centres, and the reason for their orientational polarisation. We confirm that the sequence proposed [46] for the inclusion of the vacancy containing defects correspond to an energetically favourable route, with nitrogen substituting at the surface first, and then association of a lattice vacancy and possibly a hydrogen atom with the N atom when the next atomic layer is deposited.

A second important consequence of the relative energies of the three defects lies in that the vacancy containing defects are incorporated in the diamond at all. Noting that the formation energies of the NV and NVH centres exceed that of N_s by around 2.2 eV and 1.2 eV, respectively, the statistical thermodynamic ratio of N_s to a vacancy containing centre may be obtained roughly from the factor $\exp(-\Delta E/k_B T)$, where ΔE is the energy difference noted here, k_B is Boltzmann's constant, and T the absolute temperature. This factor would suggest that $[N_s]/[NV]$ and $[N_s]/[NVH]$ would be of the order of 10^7 and 10^4, respectively at 1400°C. This admittedly crude estimate would suggest that in practice the NV and NVH centres should not be easily observed in as-grown CVD diamond. However, because the formation energies of NV and NVH centres are so much lower when in the upper two or so layers of the growing diamond, they can be incorporated, and then become fixed in the diamond in supersaturation due to the very high barriers to migration.

These results specific to the incorporation of nitrogen-containing defects is likely to have relevance to the incorporation of other impurities, with boron, silicon, and

phosphorus being particularly significant cases. We expect that the general principle of the stabilisation of vacancy-impurity complexes in the upper-most layers of a growing diamond to also be the case for these species. The evidence of the incorporation of silicon-vacancy complexes may therefore have a similar explanation to that of NV and NVH, but the B and P cases are much less obvious as there is meagre evidence for the formation of B–V or P–V complexes. These impurities will be the subject matter of a future study.

Finally, we also note that the mechanism of NV and NVH incorporation leading to orientational polarisation also provides some insight into the way in which the diamond itself is growing, and further studies to illuminate these relations will be of great importance.

Chapter 7

Polarisation of silicon split-vacancy defect in diamond

7.1 Introduction

Silicon is known to be incorporated during CVD growth due to contamination from silica components in the growth chamber, as a consequence of chemical and plasma etching [14,152]. It can be also incorporated during HPHT diamond growth by adding silicon to the graphite in the growth cell or by using silicon-carbide as a starting material [30,86]. There is no published direct evidence showing that the silicon present in diamond as substitutional impurity (Si_s^0), but it has been observed by secondary ion mass spectroscopy (SIMS) that the concentration of (Si-V)$^{0/-}$ and (Si-V:H)^0 detected by EPR does not account for the total silicon content [45, 47]. Theoretically, silicon can be stable only in its neutral charge state and may incorporate substitutionally [18,68–70]. Although vibrational spectroscopy is thought to hold the key to identifying the substitutional silicon, it is theoretically invisible to electronic-optical spectroscopy, electrical characterisation and magnetic resonance [70].

Detection of zero phonon line at 1.68 eV in luminescence or absorption usually identifies the silicon-related defects in diamond. This line has been attributed to the silicon split-vacancy defect in negative charge state (Si-V)$^-$ [30, 74]. Three EPR

defects have been observed in CVD diamond which are related to the silicon. These defects are labelled KUL1, KUL3 and KUL8 and they have spins $S = 1, 1/2$ and $1/2$, respectively. The defects were assigned to (V-Si-V)^0, (V-Si-V:H)^0 and (V-Si-V)$^-$ respectively [90–92], and they have been detected in poly-crystalline CVD diamond deposited on silicon substrates. Also, both KUL1 and KUL3 have been observed in single-crystalline CVD diamond grown on iridium [93].

As discussed in previous chapter, some defects display polarisation along specific orientations with respect to the surface. Where 100% of NV and NVH centres were polarised along the direction pointed out of (110) surface and in turn led to that these defects are growing in as a unit rather than trapping vacancies at substitutional nitrogen impurities by the migration. In the case of (V-Si-V), it seems to be more difficult to explain its polarisation, where recent experimental observation have shown that this defect was not polarised 100%, but (V-Si-V)^0 in CVD diamond grown on a [110]-oriented substrate is three times more likely to be polarised along $\langle 111 \rangle$ directions that pointed out of the (110)-growth surface. In contrast, the polarisation of (V-Si-V)^0 centre that was grown on a {100}-oriented surface can not be observed and this may refer to that all the $\langle 111 \rangle$ directions have the same angle relative to the growth plane [45]. More recently, it has been shown that the WAR3 centre, which is made up of silicon atom and divacancy complex decorated by a single hydrogen atom (Si-V2:H) with spin $S = 1/2$ and C_{1h} symmetry, displays polarisation along also $\langle 111 \rangle$ directions out of the (110)-growth surface, indicating that the complex grows in as a unit [40].

Density functional study of Si$_s$ and (V-Si-V) defects has been performed to investigate the polarisation of (V-Si-V) with respect just to (110) H-terminated surface for which the polarisation of this centre has been observed.

7.2 Method

All calculations use the method outlined in section 4.2 for bulk diamond and section 6.2 for surfaces. In particular, the wave-function basis sets for all atoms were based

on independent s and p Gaussians with four widths. For silicon atom, two sets of d Gaussians were added (constituting 40-functions per atom).

For bulk diamond, both Si_s and (V-Si-V) defects were simulated in a 216-atom supercell made up from $3 \times 3 \times 3$ conventional cell. Where Si_s in a 216-atom supercell ($C_{215}Si_1$) was used as a reference. Hyperfine interactions were modelled as outlined in chapter 4.

The (110) diamond surface has been simulated using slab-geometry approach as described in table 6.1. To study the Si_s and (V-Si-V) defect, the silicon atom was placed at lattice sites in each of the upper six layers of (110) diamond slab as shown in figure 6.1(a). For Si_s there is one possible orientation, where the silicon atom is chemically satisfied with four-fold coordination due to the similarity of silicon and carbon atoms in terms of electronic structure. In contrast, the substitutional nitrogen, as discussed in chapter 6, was modelled with three different orientations along [111], $[\bar{1}\bar{1}1]$, and either $[\bar{1}1\bar{1}]$ or $[1\bar{1}\bar{1}]$ directions due to the broken bond and the nitrogen is chemically satisfied with three-fold coordination. For (V-Si-V), the silicon atom was placed at lattice sites in some cases and at split-vacancy in the other cases. For this defect, there are two distinct orientations: one was orientated out of the (110) surface along [111] or $[\bar{1}\bar{1}1]$ which are equivalent and the second was oriented within (110) plane surface along either $[\bar{1}1\bar{1}]$ or $[1\bar{1}\bar{1}]$ directions, which are equivalent by symmetry, comparing to three different orientations of NV centre along [111], $[\bar{1}\bar{1}1]$, and either $[\bar{1}1\bar{1}]$ or $[1\bar{1}\bar{1}]$ directions.

The formation energy is calculated using the equation 6.2, where the silicon chemical potential is obtained from the condition of zero formation energy for Si_s in a 216-atom bulk diamond simulation. Also, the electrical levels (acceptors) are determined by using the same approach that used in previous chapter.

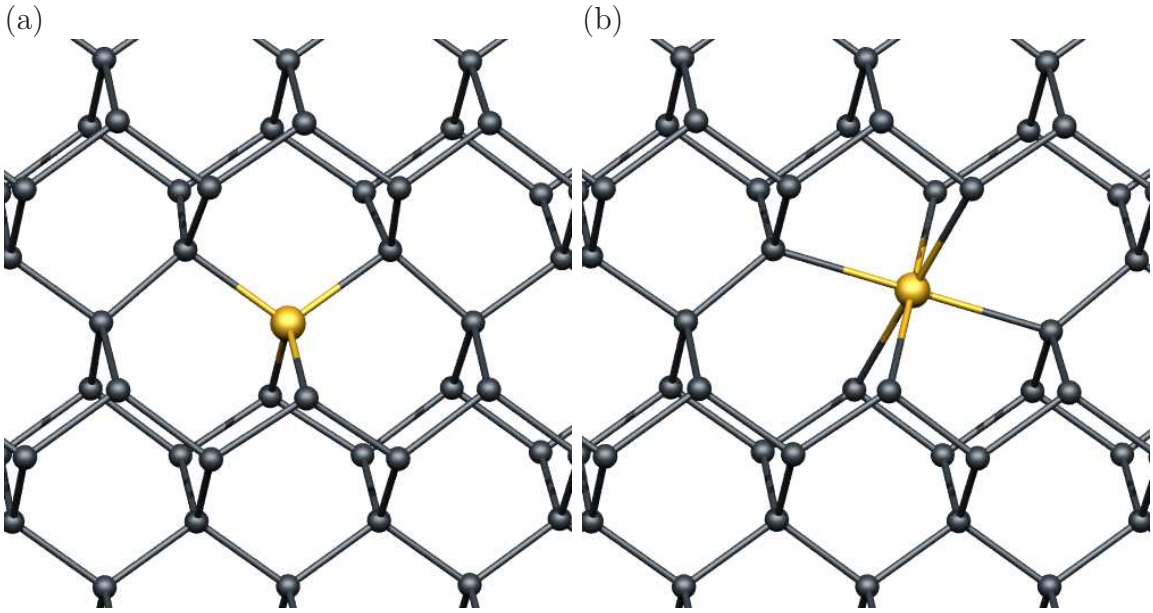

Figure 7.1: Schematic of (a) substitutional silicon (Si_s) and (b) silicon and split-vacancy (V-Si-V) in bulk diamond. The orange and gray atoms are silicon and carbon atoms, respectively. The horizontal direction is [110] and the vertical direction is [001].

7.3 Results

7.3.1 Si_s and (V-Si-V) in bulk diamond

First, substitutional silicon in bulk diamond is reviewed. Silicon has the same electronic structure to carbon atom, but the atomic radius of silicon is larger than carbon. For this reason when the structure of substitutional silicon in diamond has been optimised, the silicon atom is approximately accommodated the same position as the carbon atom, and the nearest carbon atoms move outward with increasing the bond length of Si−C to 1.74 Å, 12% greater than the normal C−C bond as illustrated in figure 7.1(a).

The band structure has been calculated and figure 7.2(a) shows that there are no levels in the host band gap. That means that there is no obvious route to obtain an unpaired electron at this defect to detect its presence in EPR, and there is no obvious

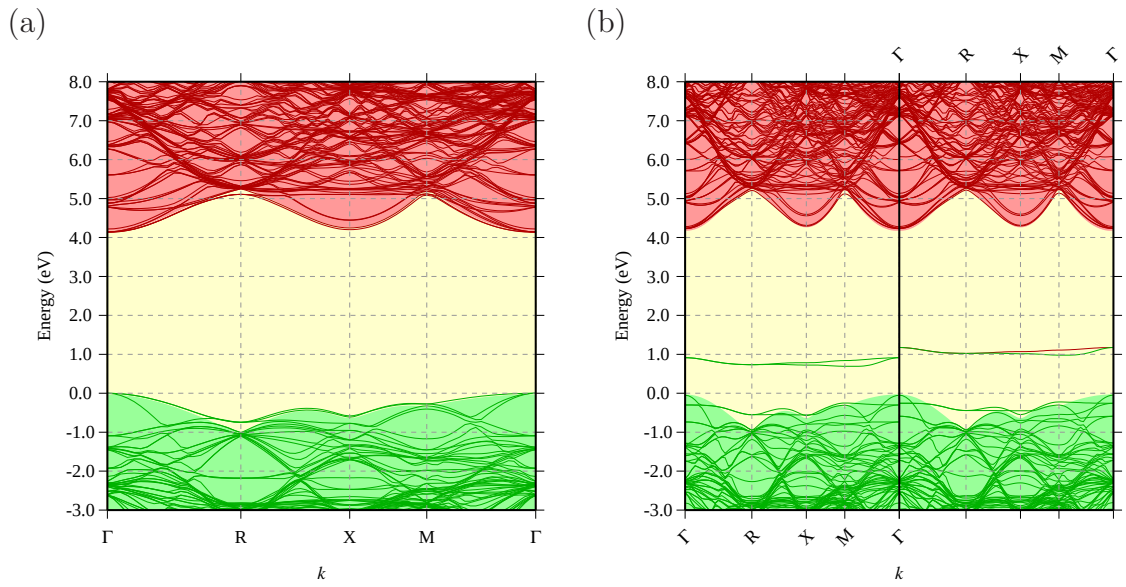

Figure 7.2: The band structure of (a) Si_s and (b) (V-Si-V) in bulk diamond. The left and right panels are spin up and spin down spectra, respectively. Shaded areas and lines represent the band structure of bulk and defective diamond, respectively. The green and red symbols show occupied and empty states, respectively. The band-structure is plotted for high symmetry branches of the simple cubic Brillouin zone using the conventional notation.

way to detect it electrically.

However, the strain in the diamond around the silicon, much like the C-centre is expected to give rise to a vibrational mode that may be detected in infrared absorption. The vibrational mode of Si_s in diamond is estimated to lie at $1338\,\mathrm{cm}^{-1}$.

Introducing a vacancy in diamond containing silicon impurity can form a new defect which is silicon-vacancy (Si-V). The Si atom in the (Si-V) defect at lattice site is unstable which in contrast to the NV centre that the defect is very stable when the nitrogen atom at its lattice site as discussed in chapter 4. A more stable structure can be formed by moving the Si atom to the split vacancy site forming a (V-Si-V) defect of D_{3d} symmetry as shown in figure 7.1(b). The negative and neutral charge states of (V-Si-V) with both $S = 1$ and $S = 0$ configurations have been modelled to calculate

Table 7.1: Hyperfine tensors (MHz) for ^{29}Si and ^{13}C in the (V-Si-V)^0 and (V-Si-V)$^-$, as shown in 7.1. Theoretical and experimental data are taken from references [?, 45]. The $A_\parallel$ and $A_\perp$ indicate to hyperfine components parallel and perpendicular to [111], respectively.

	Calculations	Theory	Experiment
		(V-Si-V)^0	
^{29}Si	$A_\parallel = 75$	78	76.3
	$A_\perp = 79$	82	78.9
^{13}C	$A_\parallel = 73$	51	66.2
	$A_\perp = 35$	12	30.2
		(V-Si-V)$^-$	
^{29}Si	$A_\parallel = 71$	74	
	$A_\perp = 75$	78	
^{13}C	$A_\parallel = 79$	61	
	$A_\perp = 40$	22	

their electronic band structures.

The band structure calculations, as illustrated in figure 7.2(b), show that two gap states u, which are created from linear combinations of the six dangling bonds whose levels are made up of bonding and anti-bonding combinations. In the neutral charge state with $S = 1$, the lower level (u_1) is occupied and the upper level (u_2) is empty, while in the negative ionised case (V-Si-V)$^-$, with $S = 1/2$ configuration, the (u_2) level is occupied. The location of u levels suggests that the (V-Si-V) can act as an acceptor in the negative charge state of (V-Si-V) and in the type-Ib or synthetic diamonds. The acceptor level of this defect has been estimated to be 1.2 eV above the valence band $(E_v + 1.2)$ eV which is in good agreement with previous LDA calculations [68].

The hyperfine interactions of (V-Si-V)^0 and (V-Si-V)$^-$ have been calculated as re-

ported in table 7.1, where the hyperfine interactions of ^{29}Si and ^{13}C in (V-Si-V)^0 centre have been predicted by LDA calculations [70] and then confirmed by experiment [45]. The hyperfine calculations show that the unpaired electrons are localised primarily upon the silicon atom ^{29}Si and the nearest neighbour carbon atoms ^{13}C, which is indicated by the relatively high hyperfine interaction magnitudes. The hyperfine tensor of ^{29}Si in (V-Si-V)^0 with one component of $A_{\parallel} = 75$ MHz and two of $A_{\perp} = 79$ MHz, which are parallel and perpendicular to [111] direction, respectively, are in accord with the values of $A_{\parallel} = 76.3$ and $A_{\perp} = 78.9$ MHz that obtained from experiment. The six nearest neighbour carbon atoms ^{13}C hyperfine interactions have the same values of $A_{\parallel} = 73$ and $A_{\perp} = 35$ MHz due to they are equivalent by symmetry and they in good agreement with the experiment values of $A_{\parallel} = 66.2$ and $A_{\perp} = 30.2$ MHz. There is no experimental data for hyperfine interactions of silicon and ^{13}C atoms in (V-Si-V)$^-$, but it has been predicted using LDA calculations [70] and the present calculations are in good agreement with them.

7.3.2 Si$_s$ and (V-Si-V) in (110)-H diamond surface

As in the previous chapter, Si$_s$ and (V-Si-V) defects have been modelled on and below (110)-H terminated diamond surface as a function of depth, as illustrated schematically in figure 6.1(a). The results of substitutional silicon are presented first, followed by (V-Si-V) including the effect of the surface upon structures, energetics, orientational anisotropy and and electrical levels. After that making comparison between the two forms including the energetic basis and statistical mechanics for existence of preferential alignment of (V-Si-V) in (110) grown samples.

7.3.2.1 Substitutional silicon

The formation energies of Si$_s$ on and below the H-terminated (110) diamond surface as a function of depth for Si$_s$ are shown in figure 7.3. There is essentially one possibility for Si$_s$ in each layer. The Si$_s$ in the uppermost carbon layer (figure 7.4(b)) is energetically favoured by around -2.0 eV. The formation energy was increased to

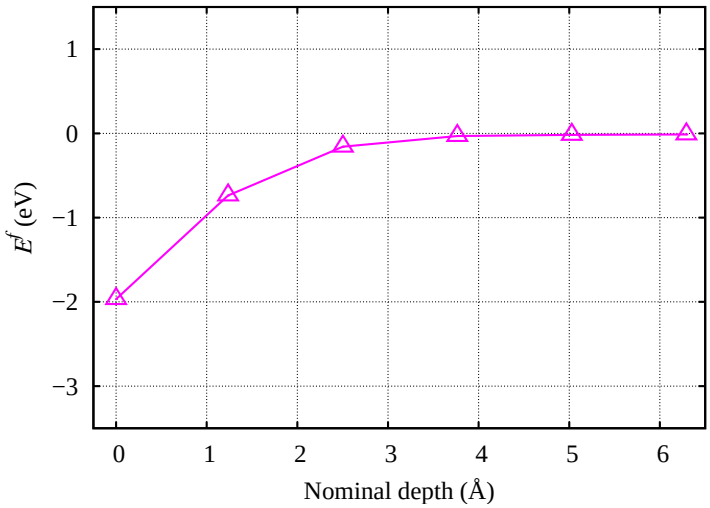

Figure 7.3: Formation energy of Si_s in (110) diamond surfaces as a function of depth of the carbon site in pristine diamond (figure 6.1), as specified by equation 6.2.

−0.8 eV when the silicon at the second layer, and it converges to zero beyond the third layer, where the approach to zero is a consequence of the definition of μ_{Si}.

The variation in energy in the first three layers is associated with the changes in geometry where strain is accommodated by displacement normal to the surface. The bond length of Si-C are increased with decreasing the energy, the bonds within the plane (along $[1\bar{1}1]$ or $[\bar{1}11]$), and into the surface along $[\bar{1}\bar{1}\bar{1}]$ are extended by about 3% and 8%, relative to Si-C length that calculated for Si_s in bulk diamond respectively. These percentages were reduced to about 0.5% and 4% when the silicon in the second layer. When silicon is in third layer, the bonds along the $[\bar{1}\bar{1}\bar{1}]$ and [111] directions were just increased by 1%, and there were no changes beyond the third layer.

Based upon the formation energy and despite both Si_s and N_s at the the first layer in the (110) surface being chemically satisfied, the difference in formation energy between the Si_s in the first layer and in bulk (figure 7.3), 2.0 eV, is lower than the difference between N_s in the first layer and in bulk as illustrated in figure 6.2(a), about 3.2 eV, which might be referred to the size of the atoms where the relaxation of silicon

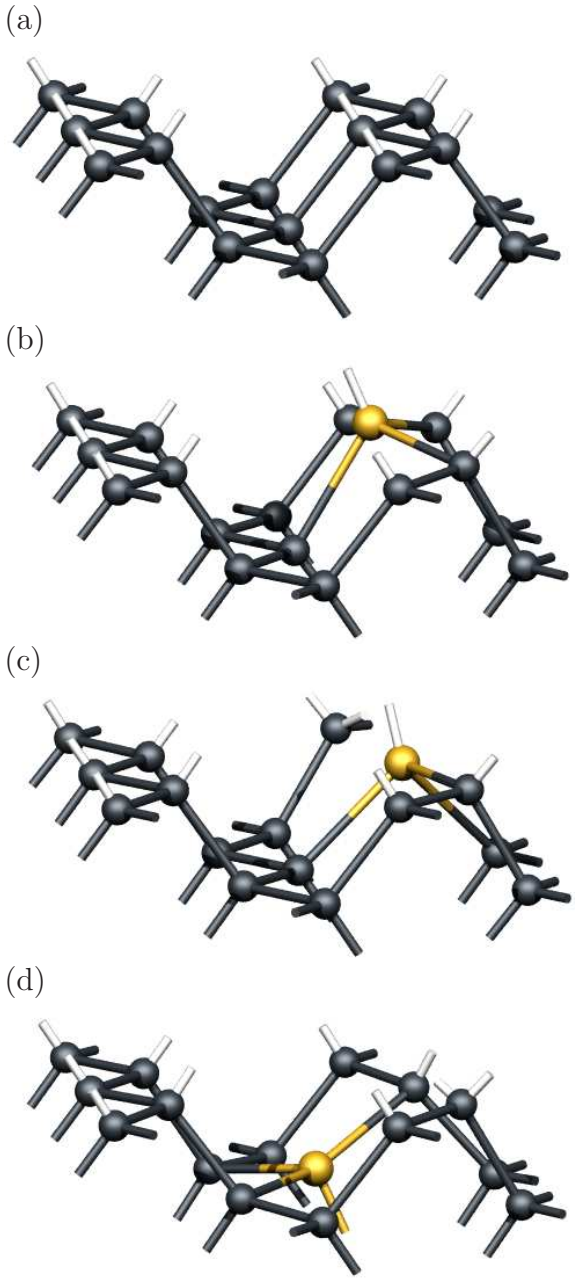

Figure 7.4: Schematic perspective structures of Si_s and (V-Si-V) defects in the (110):H surface. Black, orange and white spheres represent C, Si, and H, respectively. For clarity, surface H are not plotted but their direction is indicated by white stumps. (a) shows a section of defect free surface. (b) and (c) show Si_s and (V-Si-V) where Si lies in the upper most carbon layer, and (d) shows the (V-Si-V) where Si in the second layer.

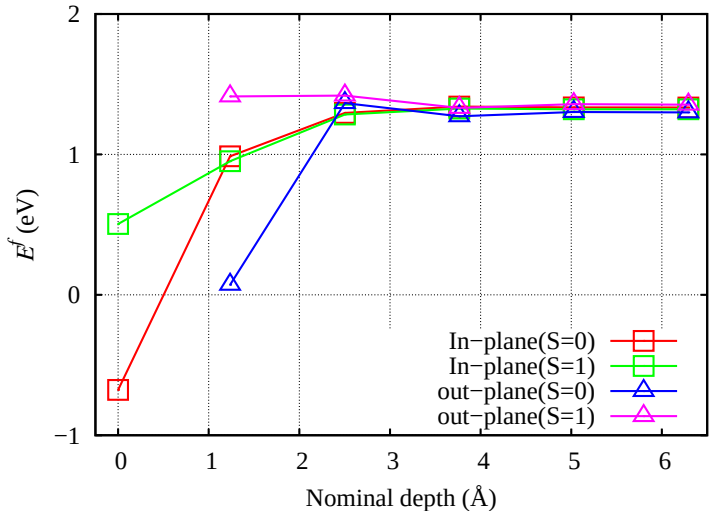

Figure 7.5: Formation energy of (V-Si-V) in (110) diamond surface as a function of depth of the carbon site in pristine diamond (figure 6.1 (a)), as specified by equation 6.2. The squares and triangles represent polarisation within the plane of the surface along $[1\bar{1}1]$ or $[\bar{1}11]$, and out of the surface along [111] and $[\bar{1}\bar{1}\bar{1}]$ directions.

atom is large comparing to nitrogen atom. This potentially means that nitrogen is easier to incorporate than silicon during diamond growth.

7.3.2.2 (V-Si-V) centre

As discussed in section 7.3.1, when the vacancy introduced in bulk diamond containing silicon, the silicon atom at the split vacancy forms a more stable structure than when the silicon on the lattice site. Figure 7.5 shows the formation energies of $(\text{V-Si-V})^0$ with $S = 0$ and $S = 1$ configurations on and below (110) surface as a function of depth. The change in formation energies with position are only significant in the uppermost two layers. Silicon and vacancy lying within the first layer (surface) along $[1\bar{1}1]$ or $[\bar{1}11]$ as shown in figure 7.4(c) is the lowest energy structure, with a value of $-0.7\,\text{eV}$. The formation energy of this structure is about $2.0\,\text{eV}$ lower compared to that in bulk diamond. To form the most stable structure when the silicon atom

and the vacancy in the first layer, the silicon atom was placed on lattice site and remove the adjacent carbon atom along $[1\bar{1}1]$ or $[\bar{1}11]$ as a starting structure. The second starting structure was the silicon atom moved to the middle of two sites (at split-vacancy position) along $[1\bar{1}1]$ or $[\bar{1}11]$. The relaxation of both structures ended up with that, the silicon atom at substitutional position (7.4(c)) is energetically more stable than when the silicon at split-vacancy position by about 1.2 eV, where all the atoms in the first structure were chemically satisfied and in the second one there is one dangling bond. Then, with silicon in the second layer and the vacancy in the first layer, which is oriented out of plane surface along [111] as shown in figure 7.4 (d), the energy rises to 0.1 eV which is lower in energy than that in bulk diamond by 1.2 eV. In this structure results from placing the silicon on the carbon site, which is lower in energy by about 1.3 eV compared to that when the silicon is placed in a split vacancy. Both (V-Si-V) structures in the first and second layers with $S = 0$ configurations are lower in energy by 1.2 and 1.3 eV, respectively, than $S = 1$ configurations due to the fact that both $S = 0$ configurations are chemically satisfied and to produce the spin triplet requires the formation of a dangling bond as in $S = 1$ configurations.

As shown in section 7.3.1, the (V-Si-V) centre has an acceptor level in bulk diamond, and it may exist in negative charge state with $S = 1/2$. The variation in the acceptor level of (V-Si-V) centre on and below (110) as a function of depth has been calculated with two orientations and it is illustrated in figure 7.6. At the surface specifically in the two most stable structure, where there are no unsaturated carbon atoms, the acceptor level is moved up to around 1.3 eV toward the conduction band. That means this shift likely reflects an absence of an acceptor level in these cases.

Thermodynamically and based upon the formation energies, it appears that the orientation of $(\text{V-Si-V})^0$ within the growth plane is more favourable than out of the surface. Furthermore, as shown in N-related defects chapter, the NV and NVH centres in a H-terminated (110) surface when the nitrogen atom in the second layer and the vacancy in the first layer pointed out of the surface were more favourable than ionised nitrogen or the P1-centre when the nitrogen in the second layer with the

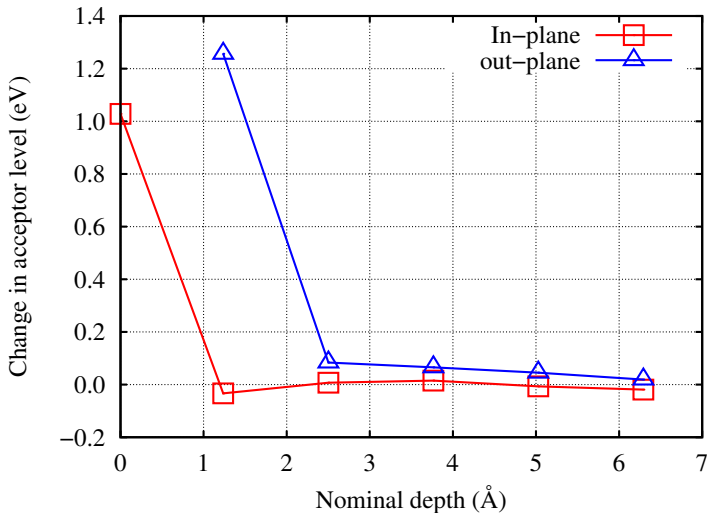

Figure 7.6: Calculated changes in acceptor level for Si-V in (110) diamond surface and as a function depth. A positive change indicates that the level is moving upward in energy, away from the valence band top. Symbols follow the definition in figure 7.5.

same orientation. This is not the case for (V-Si-V), where the Si_s in second layer is more favourable than the (V-Si-V) by about 0.9 eV when the silicon atom in the second layer and the vacancy in the first layer pointed out of the surface. That means the polarisation of (V-Si-V) out of the surface in (110) grown diamond cannot be explained, similar to the sequence obtained for NV centre in previous calculations [5]. This is inconsistent with the experiment where it has been shown that a substantial fraction of (V-Si-V) can be polarised out of the plane surface during growth and it is growing in as a unit. As mentioned for NV centre in previous chapter, the polarisation of this defect can not explained under thermodynamic equilibrium only. However, it will again be shown that this is a combination of thermodynamic layered growth does.

The preferential alignment of (V-Si-V) might be explained using statistical mechanics by calculating the ratio between the defect in the first layer and the defect in the second layer. Let us defined A as the ratio between the concentration of Si_s in the first layer and the concentration of (V-Si-V) when both Si atom and vacancy in the

first layer. This will have the $A \approx \exp(-1.3/k_BT)$ form, where $-1.3\,\text{eV}$ is the difference in formation energy between Si_s in the first layer and (V-Si-V) lie in the plane surface. k_B is Boltzmann's constant and T is the temperature Similarly, we define B as the ratio between concentration of Si_s in the second layer and the concentration of (V-Si-V) when Si atom in the second layer and the vacancy in the first layer which is oriented out of plane surface (along [111] or [11$\bar{1}$]). Thus, $B \approx \exp(-0.8/k_BT)$, where -0.8 eV is the difference in formation energy between Si_s and (V-Si-V) when Si atom in the second layer.

$$\frac{A}{B} \propto \exp(-\Delta E/k_BT) \tag{7.1}$$

Taking ΔE to be the difference in formation energy between the concentration of (V-Si-V) that oriented in the plane surface and concentration of the same defect that oriented out of the surface which is equal to $-0.5\,\text{eV}$ and the relationship 7.1 becomes $A/B \propto \exp(-0.5/k_BT)$. To predict the ratio between the two orientation concentratios, T is assumed to be diamond growth temperature which is between 900-1200 K.

This equation might tell us the possibility to form (V-Si-V) with orientation pointed out of the surface relative to the other orientation and Si_s in a system in thermal equilibrium. At lower growth temperature (about 900 K) yields $A/B = 0.0016$. That means, if one of Si_s or (V-Si-V) incorporated during growth with the orientation along [1$\bar{1}$1] or [$\bar{1}$11], hundreds of (V-Si-V) with orientation along [111] or [11$\bar{1}$] can be formed. By increasing the temperature to 1200 K the possibility to form (V-Si-V) oriented out of the surface is reduced to 20%. That means the (V-Si-V) centre can be polarised along [111] or [11$\bar{1}$] pointed out of (110) diamond surface and in turn led to that the defect is grown in as a unit. These results also can explain the experiment observation that this defect was not polarised 100%.

By considering the layer-by-layer growth of CVD diamond, it is possible to imagine incorporation of (V-Si-V) into the diamond lattice as a unit. The silicon atom is incorporated first on substitutional site. By adding the next layer, the probability for incorporation of carbon atom would be reduced forming (V-Si-V) with orientation

pointed out of (110) surface. According to the present calculations, the silicon atom on substitutional site as shown in figure 7.4 (b) with an absolute formation energy of around $-2.0\,\text{eV}$ which is also much more stable than (V-Si-V), with formation energy of about $-0.7\,\text{eV}$ which means that the formation of (V-Si-V) with in-plane orientation 7.4 (c) is less favourable relative to Si_s. In both cases Si_s and (V-Si-V) are completely chemically satisfied. Also, the Si_s when the silicon in the second layer with the formation energy of about $-0.7\,\text{eV}$ is lower in energy than (V-Si-V) when the silicon atom in the second layer and the vacancy in the first layer along [111] orientation 7.4 (d) by about $0.8\,\text{eV}$. From a statistical mechanics perspective as discussed above, covering the layer containing the silicon atom, it is likely during diamond growth that the possibility to form (V-Si-V) when the silicon in the second layer is more favourable with the formation energy of $0.1\,\text{eV}$. This result is in good agreement with experiment.

7.4 Conclusions

Si_s and (V-Si-V) defects have been modelled in the first few layers of (110) to investigate their energetics. The calculations showed that Si_s in the first layer has the lowest energy. Explanation of polarisation for (V-Si-V) centre out of the (110) growth surface was more difficult than NV centre where when the silicon atom in the first and even in the second layer, the $\text{Si}_s$is more favourable than (V-Si-V). Statistical thermodynamic ratio of Si_s to a vacancy containing centre might be obtained roughly from the factor $\exp(-\Delta E/K_B T)$, which suggests that the (V-Si-V) can be observed easily in as-grown CVD diamond. Also, it suggests that in the equilibrium system the possibility to form (V-Si-V) centre along out of (110) surface at growth temperatures is large and it can be incorporated during growth as a unit which is in agreement with experiment.

Part III

Conclusions

Chapter 8

Summary

The aim of this thesis was to study structure and incorporation mechanisms for key defect centres using density functional theory calculations to determine some of important properties in bulk diamond and diamond surfaces such as hyperfine interaction, stability, electrical and electronic structure, surface energy and electron affinity. Conclusions have been drawn at the end of each application's chapter. In this chapter the important areas are reviewed.

Some epr defects have been modelled in bulk diamond preparing to study their polarisation in different diamond surfaces later. These epr defects include two very well known ones which are P1 and nitrogen-vacancy centres and three new defects which have been observed recently via epr and labelled WAR9, WAR10 (interstitial nitrogen-related defects) and WAR2 (hydrogen-divacancy). The calculations of hyperfine interactions and electrical electronic structure showed that the results obtained for P1 and nitrogen-vacancy centres were in accord with experimental data. The hyperfine interactions of unpaired electron and ^{13}C in nearest, second and third neighbours for both centres have been calculated, where in the present calculations, some ^{13}C sites were predicted in P1 centre to be in disagreement with epr and ENDOR measurements. The proposed structures of WAR9, WAR10 and WAR2 have been modelled and the calculations showed that the results were inconsistent with the experiment. From the hyperfine interaction for proposed structure of WAR9, it

is found that the interstitial nitrogen is plausible in terms of principal values and directions, but the serious problem is the thermal stability which is very difficult to justify. For proposed structure of WAR10, which is R1-like, the principal values were consistent with experiment but the directions were not. For the proposed structure of WAR2, the calculation of hyperfine interactions showed that the results were inconsistent with observation. Also, the proposed structure was unstable thermally and there are more stable structures can be formed during diamond growth.

DFT has been used to investigate the structural and electronic properties and energies of the clean and hydrogen-terminated diamond surfaces for (110), (111) and (001) surface orientations, preparing to study the polarisation of some point defects. The calculations showed that the reconstruction and structural properties for the three surfaces are in accord with previous calculations. The calculations suggested that energetically, the (111)-2 $\times$ 1 clean surface has the lowest energy compared to other surfaces. In addition, the clean and hydrogen-terminated surfaces were confirmed to exhibit the positive and negative electron affinities, respectively, found in other theoretical work and observed in experiment. The calculation results suggested that the structures used in study, which consist of 12, 14 and 16 layers for (110),(111) and (001) surfaces, respectively, were satisfactory to study the preferential alignment of defects in CVD diamond energetically.

Substitutional nitrogen, nitrogen-vacancy and nitrogen-vacancy-hydrogen centres have been in the first few layers of (110), (111), and (001)-hydrogen terminated diamond surfaces to investigate their polarisations. The calculations showed the mechanism of the nitrogen-vacancy and nitrogen-vacancy-hydrogen centres incorporation in (110) surface and the reason for their polarisation. The sequence proposed by experiment is confirmed, with nitrogen substituting at the surface first, and then association of a lattice vacancy and possibly a hydrogen atom with the nitrogen atom when the next atomic layer is deposited. Because the formation energies of NV and NVH centres are so much lower when in the upper two so layers of the growing diamond, they can be incorporated, and then become fixed in the diamond in supersaturation due

to the very high barriers to migration.

The substitutional silicon and silicon-vacancy have been modelled to investigate their energies in the first few layers of (110). The calculations showed that Sis in the first layer has the lowest energy. Comparing to NV, polarisation of silicon-split vacancy was more difficult to explain, where even in the second layer the substitutional silicon is more favourable energetically than silicon-vacancy. Thus, polarisation of (V-Si-V) has been explained statistically, where the ratio of concentration of Sis to the concentration of vacancy containing is obtained roughly from the factor $\exp(-\Delta E/k_B T)$. This factor suggests that in the equilibrium system the possibility to form (V-Si-V) centre along out of (110) surface at growth temperatures is large and it can be incorporated during growth as a unit which is in agreement with experiment. Also, it suggested that the (V-Si-V) can be observed easily in as-grown CVD diamond.

Bibliography

[1] Adam Gali, A., et al. "Ab initio supercell calculations on nitrogen-vacancy center in diamond: Electronic structure and hyperfine tensors," *Phys. Rev. B*, *77*:155206 (2008).

[2] Alfonso, D. R., et al. "Structural, electronic, and vibrational properties of diamond (100), (111) and (110) surfaces from ab initio calculations," *Phys. Rev. B*, *51*:14669 (1995).

[3] Ammerlaan, C. A. J. *Semiconductors, Impurities and Defects in Group IV Elements and III-V Compounds*, *III41A2α*. Landolt-Börnstein, New Series. Berlin: Springer, 2002.

[4] Ashcroft, N. W. and N. D. Mermin. *Solid State Physics* (International Edition). Philadelphia: Saunders College, 1976.

[5] Atumi, M. K., et al. "Atomistic modeling of the polarization of nitrogen centers in diamond due to growth surface orientation," *Phys. Rev. B*, *88*(24):245301 (2013).

[6] Bade, J. P., et al. "Fabrication of diamond thin-film thermistors for high-temperature applications," *Diamond Relat. Mater.*, *2*:816–819 (1993).

[7] Badzian, A. and T. Badzian. "Synthesis of diamond from methane and nitrogen mixture," *Appl. Phys. Lett.*, *62*:3432 (1993).

[8] Baker, J. M., et al. "Electron paramagnetic resonance of sulfur at a split-vacancy site in diamond," *Phys. Rev. B*, *78*:235203 (2008).

[9] Balasubramanian, G., et al. "Ultralong spin coherence time in isotopically engineered diamond," *Nature Mater.*, *8*:383–387 (April 2009).

[10] Balasubramanian1, G., et al. "Nanoscale imaging magnetometry with diamond spins under ambient conditions," *Nature*, *455*:648 (2008).

[11] Balmer, R. S., et al. "Chemical vapour deposition synthetic diamond: materials, technology and applications," *J. Phys. Cond. Matter*, *21*:364221 (August 2009).

[12] Balsereschi, A. "Mean-value point in the brillouin," *Phys. Rev. B*, *7*(12):5212 (June 1973).

[13] Bandis, C. and B. B. Pate. "Electron Emission Due to Exciton Breakup from Negative Electron Affinity Diamond," *Phys. Rev. Lett.*, *74*:777 (1995).

[14] Barjon, J., et al. "Silicon incorporation in CVD diamond layers," *Phys. Status Solidi A*, *202*(11):2177–2181 (2005).

[15] Barklie, R. C. and J. Guven. "^{13}C hyperfine structure and relaxation times of the P1 centre in diamond," *J. Phys. C Solid State*, *14*:3621–3631 (1981).

[16] Baumann, P. K. and R. J. Nemanich. "Characterization of copper-diamond (100), (111), and (110) interfaces: Electron affinity and Schottky barrier," *Phys. Rev. B*, *58*(3):1643 (1998).

[17] Bergonzo, P., et al. "CVD diamond-based semi-transparent beam-position monitors for synchrotron beamlines: preliminary studies and device developments at CEA/Saclay," *J. Synchrotron Radiat.*, *13*:151–158 (2006).

[18] Bicai, P. and X. Shangda. "Formation energy and electronic structure of silicon impurities in diamond," *Phys. Rev. B*, *49*(16):11444–11447 (April 1994).

[19] Blöchl, P. E. "Projector augmented-wave method," *Phys. Rev. B*, *50*(24):17953–17979 (December 1994).

[20] Briddon, P. R. and R. Jones. "Theory of impurities in diamond," *Physica B*, *185*(1–4):179–189 (1993).

[21] Briddon, P. R. and R. Jones. "LDA calculations using a basis of Gaussian orbitals," *Phys. Status Solidi B*, *217*(1):131–171 (2000).

[22] Briddon, P. R., et al. "Theory of nitrogen in diamond – the substitutional atom, A centre, and the platelet." *Proc. International Conference on New Diamond Science and Technology*, edited by R. Messier, et al. 63. Pittsburgh: Materials Research Society, 1991.

[23] Bundy, F. P. and H. M. Strong. *Solid State Physics*, *13*. New York: Academic, 1962.

[24] Bustarret, E., et al. "Dependence of the superconducting transition temperature on the doping level in single-crystalline diamond films," *Phys. Rev. Lett.*, *93*(23):237005 (2004).

[25] Butler, J. E., et al. "Exceptionally high voltage Schottky diamond diodes and low boron doping," *Semicond. Sci. Technol.*, *18*:S67–S71 (February 2003).

[26] Cann, B. L. *Magnetic Resonance Studies of Point Defects in Diamond*. PhD dissertation, Department of Physics, University of Warwick, UK., October 2009.

[27] Chadi, D. J. and M. L. Cohen. "Electronic Structure of Hg1-xCdxTe Alloys and Charge- Density Calculations Using Representative k Points," *Phys. Rev. B*, *7*(2):692 (January 1973).

[28] Chang, X., et al. "Electron Beam Emission from a Diamond-Amplifier Cathode," *Phys. Rev. Lett.*

[29] Chrenko, R. M., et al. "Dispersed paramagnetic nitrogen content of large laboratory diamonds," *Phil. Mag.*, *23*:313–318 (1971).

[30] Clark, C. D., et al. "Silicon defects in diamond," *Phys. Rev. B*, *51*(23):16681–16688 (June 1995).

[31] Cohen, M. L. "Calculation of bulk moduli of diamond and zinc- blende solids," *Phys. Rev. B*, *32*(12):7988–7991 (1985).

[32] Collins, A. T. "Vacancy enhanced aggregation of nitrogen in diamond," *J. Phys. C*, *13*:2641–2650 (1980).

[33] Collins, A. T., et al. "Nitrogen isotope effects in synthetic diamonds," *J. Phys. D*, *20*:969–974 (1987).

[34] Cook, R. J.and Whiffen, D. H. "Electron Nuclear Double Resonance Study of a Nitrogen Centre in Diamond," *Proc. R. Soc.*, *295*(1441):99–106 (1966).

[35] Cui, J. B., et al. "Electron AfiňĄnity of the Bare and Hydrogen Covered Single Crystal Diamond (111) Surface," *Phys. Rev. Lett.*, *81*:429 (1998).

[36] Davies, G. and M. F. Hamer. "Optical studies of the 1.945-eV vibronic band in diamond," *Proc. R. Soc. London, Ser. A*, *348*:285–298 (1976).

[37] Davies, G., et al. "The 1018 meV (W or I_1) vibronic band in silicon," *J. Phys. C*, *20*(2):191–205 (1987).

[38] Davies, G., et al. "The self-interstitial in diamond," *Phys. Rev. B*, *62*(3):1528–1531 (2000).

[39] Degen, C. L. "Scanning magnetic field microscope with a diamond single- spin sensor," *Appl. Phys. Lett.*, *92*:243111 (2008).

[40] D'Haenens-Johansson, U. F. S., et al. "Optical properties of the neutral silicon split-vacancy center in diamond," *Phys. Rev. B*, *84*:245208 (2011).

[41] D'Haenens-Johansson, U. F. S., et al. "EPR of a defect in CVD diamond involving both silicon and hydrogen that shows preferential alignment," *Phys. Rev. B*, *82*:155205 (2010).

[42] Dolde, F., et al. "Electric-field sensing using single diamond spins," *Nature Phys.*, *7*:459–463 (2011).

[43] du Preez, L. PhD dissertation, University of the Witwatersrand, Johannesburg, 1965.

[44] Duke, C. B. "Surface structures of tetrahedrally coordinated semiconductors: principles, practice, and universality," *Appl. Surf. Sci.*, *65/65*:543–552 (1993).

[45] Edmonds, A. M. *Magnetic resonance studies of point defects in single crystal diamond*. PhD dissertation, The University of Warwick, July 2008.

[46] Edmonds, A. M., et al. "Production of oriented nitrogen-vacancy color centers in synthetic diamond," *Phys. Rev. B*, *86*:035201 (2012).

[47] Edmonds, A. M. and M. E. Newton. "Electron paramagnetic resonance studies of silicon-related defects in diamond," *Phys. Rev. B*, *77*:245205 (2008).

[48] Etmimi, K. M., et al. "Nitrogen-pair paramagnetic defects in diamond: A density functional study," *Phys. Rev. B*, *79*:205207 (May 2009).

[49] Etmimi, K. M., et al. "Density functional studies of muonium in nitrogen-aggregate containing diamond: the MuX centre.," *J. Phys. Cond. Matter*, *21*:364211 (August 2009).

[50] Etmimi, K. M., et al. "A density functional theory study of models for the N3 and OK1 EPR centres in diamond.," *J. Phys. Cond. Matter*, *22*:385502 (September 2010).

[51] Evans, T. and Z. Qi. "The kinetics of the aggregation of nitrogen atoms in diamond," *Proc. R. Soc. London, Ser. A*, *381*:159–178 (1982).

[52] Farrer, R. "On the substitutional nitrogen donor in diamond," *Solid State Commun.*, 7:685 (1969).

[53] Felton, S., et al. "Chemical vapour deposition synthetic diamond: materials, technology and applications," *J. Phys. Cond. Matter*, *21*:364212 (August 2009).

[54] Felton, S., et al. "Hyperfine interaction in the ground state of the negatively charged nitrogen vacancy center in diamond," *Phys. Rev. B*, *79*:075203 (February 2009).

[55] Felton, S., et al. "Electron paramagnetic resonance studies of the neutral nitrogen vacancy in diamond," *Phys. Rev. B*, *77*:081201 (2008).

[56] Frauenheim, Th., et al. "Stability, reconstruction, and electronic-properties of diamond (100) and (111) surfaces," *Phys. Rev. B*, *48*(24):18189–18202 (1993).

[57] Fukunaga, O. and N. Miyake, T. Ohashi. "Formation of diamond and graphite at high pressure using glassy carbon source," *Diamond Relat. Mater.*, *14*:160–166 (2005).

[58] Furthmüller, J., et al. "Dimer reconstruction and electric surface states on clean and hydrogenated diamond (100) surfaces," *Phys. Rev. B*, *53*(11):7334–7351 (1996).

[59] Gali, A. "Theory of the neutral nitrogen-vacancy center in diamond and its application to the realization of a qubit," *Phys. Rev. B*, *79*:235210 (2009).

[60] Gippius, A. A., et al. "Defects production and interaction in ion-implanted diamond," *Physica B & C*, *116*:187–194 (1983).

[61] Glover, C., et al. "Hydrogen Incorporation in Diamond: The Nitrogen-Vacancy-Hydrogen Complex," *Phys. Rev. Lett.*, *90*(18):185507 (2003).

[62] Glover, C., et al. "Hydrogen incorporation in diamond: the vacancy-hydrogen complex," *Phys. Rev. Lett.*, *92*:135502 (2004).

[63] Godfried, H. P., et al. "Use of CVD diamond in high-power CO2 lasers and laser diode arrays," *Proc. SPIE*, *3889*:553 (2000).

[64] Goss, J. P., et al. "Platelets and the (110) a0âĹŢ4 001 stacking fault in diamond," *Phys. Rev. B*, *73*:115204 (2006).

[65] Goss, J. P., et al. "The vacancy nitrogen hydrogen complex in diamond: a potential deep centre in chemical vapour deposited material," *J. Phys. Cond. Matter*, *15*:S2903–S2911 (2003).

[66] Goss, J. P., et al. "Interstitial nitrogen and its complexes in diamond," *Phys. Rev. B*, *70*(23):235208 (2004).

[67] Goss, J. P., et al. "Optically active point defects in high quality single crystal diamond," *Phys. Status Solidi A*, *207*(9):2049–2053 (August 2010).

[68] Goss, J. P., et al. "Vacancy-impurity complexes and limitations for implantation doping of diamond," *Phys. Rev. B*, *72*(3):035214 (July 2005).

[69] Goss, J. P., et al. "Erratum: Vacancy-impurity complexes and limitations for implantation doping of diamond [Phys. Rev. B 72, 035214 (2005)]," *Phys. Rev. B*, *73*(19):199904(E) (May 2006).

[70] Goss, J. P., et al. "Density functional simulations of silicon-containing point defects in diamond," *Phys. Rev. B*, *76*:075204 (2007).

[71] Goss, J. P., et al. "Donor and acceptor states in diamond," *Diamond Relat. Mater.*, *13*(4–8):684–690 (2004).

[72] Goss, J. P., et al. "Extended defects in diamond: the interstitial platelet," *Phys. Rev. B*, *67*(16):165208 (April 2003).

[73] Goss, J. P., et al. "Self-interstitial aggregation in diamond," *Phys. Rev. B*, *63*(19):195208 (2001).

[74] Goss, J. P., et al. "The twelve-line 1.682 eV luminescence center in diamond and the vacancy-silicon complex," *Phys. Rev. Lett.*, *77*(14):3041–3044 (1996).

[75] Graupner, R., et al. "Dispersions of surface states on diamond (100) and (111)," *Phys. Rev. B*, *55*(16):10841 (1997).

[76] Hamza, A. V., et al. "The role of hydrogen on the diamond C(111)-(2x1) reconstruction," *Surface Sci.*, *206*:L833–L844 (1988).

[77] Hartwigsen, C., et al. "Relativistic separable dual-space Gaussian pseudopotentials from H to Rn," *Phys. Rev. B*, *58*(7):3641–3662 (1998).

[78] He, X.-F., et al. "Paramagnetic resonance of photoexcited N-V defects in diamond. II. Hyperfine interaction with the ^{14}N nucleus," *Phys. Rev. B*, *47*(14):8816–8822 (April 1993).

[79] Henkelman, G. and H. Jónsson. "Improved tangent estimate in the nudged elastic band method for finding minimum energy paths and saddle points," *J. Chem. Phys.*, *113*(22):9978–9985 (2000).

[80] Henkelman, G., et al. "A climbing image nudged elastic band method for finding saddle points and minimum energy paths," *J. Chem. Phys.*, *113*(22):9901–9904 (2000).

[81] Hetényi, B., et al. "Reconstruction of frozen-core all-electron orbitals from pseudo-orbitals," *J. Chem. Phys.*, *115*(13):5791–5795 (October 2001).

[82] Himpsel, F. J., et al. "Quantum photoyield of diamond(111)A stable negative-affinity emitter," *Phys. Rev. B*, *20*:624–627 (1979).

[83] Hiscocks, M. P., et al. "Reactive ion etching of waveguide structures in diamond," *Diamond Relat. Mater.*, *17*:1831–1834 (2008).

[84] Hohenberg, P. and W. Kohn. "Inhomogeneous Electron Gas," *Phys. Rev.*, *136*(3B):864–871 (1964).

[85] Hom, T., et al. "Accurate Lattice Constants from Multiple Reflection Measurements II. Lattice Constants of Germanium, Silicon and Diamond," *J. Alloys and Compounds*, *8*:457 (1975).

[86] Hong, S. M., et al. "Cathodoluminescence of diamond synthesized from silicon-carbide," *Chinese Sci. Bull.*, *41*:208 (1996).

[87] Hood, R. Q., et al. "Quantum Monte Carlo Study of the Optical and Diffusive Properties of the Vacancy Defect in Diamond," *Phys. Rev. Lett.*, *91*(07):076403 (2003).

[88] Hunt, D. C., et al. "Identification of the neutral carbon [100]-split interstitial in diamond," *Phys. Rev. B*, *61*(6):3863–3876 (2000).

[89] Hunt, D. C., et al. "EPR data on the self-interstitial complex $O3$ in diamond," *Phys. Rev. B*, *62*(10):6587–6597 (September 2000).

[90] Iakoubovskii, K. and A. Stesmans. "Characterization of Defects in as-Grown CVD Diamond Films and HPHT Diamond Powders by Electron Paramagnetic Resonance," *Phys. Status Solidi A*, *186*(2):199–206 (2001).

[91] Iakoubovskii, K. and A. Stesmans. "Characterization of hydrogen and silicon-related defects in CVD diamond by electron spin resonance," *Phys. Rev. B*, *66*(19):195207 (2002).

[92] Iakoubovskii, K., et al. "ESR and Photo-ESR study of defects in CVD diamond," *Phys. Status Solidi A*, *193*(3):448–456 (2002).

[93] Iakoubovskii, K., et al. "Characterization of defects in monocrystalline CVD diamond films by electron spin resonance," *Diamond Relat. Mater.*, *12*(3-7):511–515 (Mar-Jul 2003).

[94] Iakoubovskii, K., et al. "Symmetry of the hydrogen-vacancy-like defect $H1$ in diamond," *Phys. Rev. B*, *66*(11):113203 (2002).

[95] Jelezko, F., et al. "Observation of Coherent Oscillation of a Single Nuclear Spin and Realization of a Two-Qubit Conditional Quantum Gate," *Phys. Rev. Lett.*, *93*(13):130501 (2004).

[96] Jin, S. and T.D. Moustakas. "Effect of nitrogen on the growth of diamond films," *Appl. Phys. Lett.*, *65*:403 (May 1994).

[97] Johnston, C., et al. "Boron doping and characterisation of diamond." *Properties, growth and applications of diamond* Number 26 in EMIS Datareviews Series, edited by M. H. Nazaré and A. J. Neves, chapter B3.3, 337–347, London: INSPEC, Institute of Electrical Engineers, 2001.

[98] Jones, R. and J. P. Goss. "Theory of aggregation of nitrogen in diamond." *Properties, growth and applications of diamond* Number 26 in EMIS Datareviews Series, edited by M. H. Nazaré and A. J. Neves, chapter A5.1, 127–129, London: INSPEC, Institute of Electrical Engineers, 2001.

[99] Jones, R., et al. "Acceptor level of nitrogen in diamond and the 270-nm absorption band," *Phys. Rev. B*, *80*(3):033205 (2009).

[100] Kajihara, S. A., et al. "Nitrogen and potential n-type dopants in diamond," *Phys. Rev. Lett.*, *66*(15):2010–2013 (April 1991).

[101] Kang, W. P., et al. "Diamond vacuum field emission devices," *Diamond Relat. Mater.*, *13*:1944–1948 (2004).

[102] Kačmarčik, J., et al. "Superconductivity in boron-doped homoepitaxial (001)-orented diamond layers," *Phys. Status Solidi A*, *202*(11):2160–2165 (August 2005).

[103] Kennedy, T. A., et al. "Long coherence times at 300 K for nitrogen-vacancy center spins in diamond grown by chemical vapor deposition," *Appl. Phys. Lett.*, *83*:4190 (2003).

[104] Kern, G and J. Hafner. "Ab initio calculations of the atomic and electronic structure of clean and hydrogenated diamond (110) surfaces," *Phys. Rev. B*, *56*(7):4203–4210 (1997).

[105] Kern, G., et al. "(2 X 1) reconstruction and hydrogen-induced de-reconstruction of the diamond (100) and (111) surfaces," *Surface Sci.*, *352-354*:745–749 (1996).

[106] Kern, G., et al. "Atomic and electronic structure of diamond (111) surfaces I. Reconstruction and hydrogen-induced de-reconstruction of the one dangling-bond surface," *Surface Sci.*, *366*:445–463 (1996).

[107] Kern, G., et al. "Atomic and electronic structure of diamond (111) surfaces: II. (2×1) and $\sqrt{3} \times \sqrt{3}$ reconstructions of the clean and hydrogen-covered three dangling-bond surfaces.," *Surface Sci.*, *366*:464–482 (1996).

[108] Kerridge, A., et al. "Quantum behaviour of hydrogen and muonium in vacancy-containing complexes in diamond," *J. Phys. Cond. Matter*, *16*:8743–8751 (2004).

[109] Khan, R. U. A., et al. "Charge transfer effects, thermo and photochromism in single crystal CVD synthetic diamond," *J. Phys. Cond. Matter*, *21*:364214 (August 2009).

[110] Kiflawi, I. and S. C. Lawson. "Aggregates of nitrogen in diamond." *Properties, growth and applications of diamond* Number 26 in EMIS Datareviews Series, edited by M. H. Nazaré and A. J. Neves, chapter A5.2, 130–133, London: INSPEC, Institute of Electrical Engineers, 2001.

[111] Kiflawi, I., et al. "Nitrogen interstitials in diamond," *Phys. Rev. B*, *54*(23):16719–16726 (1996).

[112] Kohn, W. and L. J. Sham. "Self-consistent equations including exchange and correlation effects," *Phys. Rev.*, *140*(4A):A1133–A1138 (1965).

[113] Lany, S. and A. Zunger. "Assessment of correction methods for the band-gap problem and for iňĄnite-size effects in supercell defect calculations: Case studies for ZnO and GaAs," *Phys. Rev. B*, *78*:235104 (2008).

[114] Larsson, K. "Substitutional n-type doping of diamond," *Comp. Mater. Sci.*, *27*:23–29 (2003).

[115] Liberman, D. A. "Slater transition-state band-structure calculations," *Phys. Rev. B*, *62*(11):6851–6853 (2000).

[116] Lide, D. R., editor. *CRC handbook of chemistry and physics* (75 Edition). London: CRC Press, 1995.

[117] Liggins, S., et al. "Identification of the dinitrogen ¡001¿ split interstitial H1a in diamond," *Phys. Rev. B*

[118] Lombardi, E. B., et al. "Ab initio study of the passivation and interaction of substitutional impurities with hydrogen in diamond," *Diamond Relat. Mater.*, *12*:490–494 (2003).

[119] Loubser, J. H. N. and J. A. van Wyk. "Electron spin resonance in the study of diamond," *Rep. Prog. Phys.*, *41*(8):1201–1248 (August 1978).

[120] Luszczek, M., et al. "The ab initio calculations of single nitrogenvacancy defect center in diamond," *Physica B*, *348*:292–298 (2004).

[121] Maier, F., et al. "The hydrogenated and bare diamond (110) surface: a combined LEED-, XPS-, and ARPES study," *Surface Sci.*, *443*:177–185 (1999).

[122] Maier, F., et al. "Origin of surface conductivity in diamond," *Phys. Rev. Lett.*, *85*(16):3472–3475 (October 2000).

[123] Maier, F., et al. "Electron affinity of plasma-hydrogenated and chemically oxidized diamond (100) surfaces," *Phys. Rev. B*, *64*(16):165411 (October 2001).

[124] Makov, G. and M. C. Payne. "Periodic boundary conditions in *ab initio* calculations," *Phys. Rev. B*, *51*(7):4014–4122 (1995).

[125] Maze, J. R., et al. "Nanoscale magnetic sensing with an individual electronic spin in diamond," *Nature*, *455*:644 (2008).

[126] Miller, A. J., et al. "Diamond coatings for IR window applications," *Diamond Relat. Mater.*, *6*(2):386–389 (March 1997).

[127] Mita, Y. "Change of absorption spectra in type-Ib diamond with heavy neutron irradiation," *Phys. Rev. B*, *53*(17):11360–11364 (May 1996).

[128] Mizuochi, N., et al. "Electrically driven single-photon source at room temperature in diamond," *Nature Photonics*, *6*:299–303 (2012).

[129] Monkhorst, H. J. and J. D. Pack. "Special points for Brillouin-zone integrations," *Phys. Rev. B*, *13*(12):5188–5192 (1976).

[130] Newton, M. E., et al. "Recombination-enhanced diffusion of self-interstitial atoms and vacancy interstitial recombination in diamond," *Diamond Relat. Mater.*, *11*:618–622 (2002).

[131] Pace, E., et al. "CVD diamond optics for ultraviolet," *Diamond Relat. Mater.*, *10*(3):736–743 (March 2001).

[132] Pack, J. D. and H. J. Monkhorst. "Special points for Brillonln-zone integrations"-a reply," *Phys. Rev. B*, *16*:1748–1749 (1977).

[133] Pandey, K. C. "New n-Bonded Chain Model for Si(111)-(2x1) Surface," *Phys. Rev. Lett.*, *47*(26):1913 (1981).

[134] Pandey, K. C. "New dimerized-chain model for the reconstruction of the diamond (111)-(2 ÃŮ 1) surface," *Phys. Rev. B*, *25*:4338 (1982).

[135] Pate, B. B. "THE DIAMOND SURFACE: ATOMIC AND ELECTRONIC STRUCTURE," *Surface Sci.*, *165*:83 (1986).

[136] Perdew, J. P., et al. "Generalized Gradiaent Approximation made simple," *Phys. Rev. Lett.*, *77*(18):3865–3868 (1996).

[137] Perdew, J. P. and A. Zunger. "2 theorems on the self-interaction in density functional theory," *Bull. Am. Phys. Soc.*, *26*(3):470 (1981).

[138] Pinto, H., et al. "Point and extended defects in chemical vapour deposited diamond," *J. Phys. Conf. S.*, *281*:012023 (2011).

[139] Pinto, H., et al. "Theory of the surface effects on the luminescence of the NV^- defect in nanodiamond," *Phys. Status Solidi A*, *208*:2045–2050 (2011).

[140] Pinto, H., et al. "On the diffusion of NV defects in diamond," *Phys. Status Solidi A*, *209*:1765–1768 (2012).

[141] Poferl, D. J., et al. "Growth of boron-doped diamond seed crystals by vapor deposition," *J. Appl. Phys.*, *44*:1428–1434 (1973).

[142] Polak, E. *Computational methods in optimisation: a unified approach*. Berkley, California, USA: Academic Press, 1971.

[143] Press, W. *Numerical Methods in Fortran 77*. Cambridge, UK: Cambridge University Press, 1996.

[144] Rameau, J. D., et al. "Properties of Hydrogen Terminated Diamond as a Photocathode," *Phys. Rev. Lett.*, *106*:137602 (2011).

[145] Rayson, M. J. "Lagrange-Lobatto interpolating polynomials in the discrete variable representation," *Phys. Rev. E*, *76*(07):026704 (2007).

[146] Rayson, M. J. and P. R. Briddon. "Rapid iterative method for electronic-structure eigenproblems using localised basis functions," *Computer Phys. Comm.*, *178*:128–134 (2008).

[147] Rayson, M. J. and P. R. Briddon. "Highly efficient method for Kohn-Sham density functional calculations of 500-10000 atom systems," *Phys. Rev. B*, *80*(1):205104 (Sept 2009).

[148] Ristein, J. "Electronic properties of diamond surfaces – blessing or curse for devices?," *Diamond Relat. Mater.*, *9*(3–6):1129–1137 (April 2000).

[149] Ristein, J. "Diamond surfaces: familiar and amazing," *Appl. Phys. A*, *82*:377–384 (2006).

[150] Ristein, J. "Surface science of diamond: Familiar and amazing," *Surface Sci.*, *600*:3677–3689 (2006).

[151] Robertson, J. and M. J. Rutter. "Band diagram of diamond and diamond-like carbon surfaces," *Diamond Relat. Mater.*, 7:620–625 (1998).

[152] Robins, L. H., et al. "Cathodoluminescence of defects in diamond films and particles grown by hot-filament chemical-vapor deposition," *Phys. Rev. B*, *39*(18):13367–13377 (June 1989).

[153] Rutter, M. J. ad. Robertson. J. "*Ab initio* calculation of electron affinities of diamond surfaces," *Phys. Rev. B*, *57*(15):9241–9245 (1998).

[154] Schmidt, W. G., et al. "Dimerized, buckled, or ideal chains on the diamond (111) 2 x 1 surface?," *Surface Sci.*, *351*:183–188 (1996).

[155] Scholze, A., et al. "Structure of the diamond (111) surface: Single- dangling-bond versus triple-dangling-bond face," *Phys. Rev. B*, *53*(20):13725 (1996).

[156] Shaw, M. J., et al. "Importance of Quantum Tunneling in Vacancy-Hydrogen Complexes in Diamond," *Phys. Rev. Lett.*, *95*(10):105502 (2005).

[157] Siebert, J., et al. "Diamond formation in metalcarbonate interactions," *Earth Planet. Sci. Lett.*, *229*:205–216 (2005).

[158] Singh, J. *Physics of semiconductors and their heterostructures.* New York: McGraw-Hill, 1993.

[159] Sque, S. J. *A first-principles study on bulk and transfer doping of diamond.* PhD dissertation, The University of Exeter, November 2005.

[160] Sque, S. J., et al. "Hydrogenation and oxygenation of the (100) diamond surface and the consequences for transfer doping," *Phys. Status Solidi A*, *202*:2091–2097 (2005).

[161] Sque, S.J., et al. "Structure, electronics, and interaction of hydrogen and oxygen on diamond surfaces," *Phys. Rev. B*, *73*:085313 (2006).

[162] Steckel, J. A., et al. "Structural characterization of the hydrogen-covered C(100) surface by density functional theory calculations," *Phys. Rev. B*, *66*:155406 (2002).

[163] Steeds, J. W., et al. "Photoluminescence microscopy of TEM irradiated diamond," *Diamond Relat. Mater.*, *9*(3-6):397–403 (April 2000).

[164] Steinert, S., et al. "High sensitivity magnetic imaging using an array of spins in diamond," *Rev. Sci. Instrum.*, *81*:043705 (2010).

[165] Strobel, P., et al. "Surface transfer doping of diamond," *Nature Mater.*, *430*:439 (2004).

[166] Sze, S. M. *Physics of Semiconductor Devices* (2nd Edition). New York: Wiley-Interscience, 1981.

[167] Taylor, J. M., et al. "High-sensitivity diamond magnetometer with nanoscale resolution," *Nature Phys.*, *4*:810–816 (2008).

[168] Thonke, K. "The boron acceptor in diamond," *Semicond. Sci. Technol.*, *18*:S20–S26 (February 2003).

[169] Tiwari, A. K., et al. "Calculated electron afiňĄnity and stability of halogen-terminated diamond," *Phys. Rev. B*, *84*:245305 (2011).

[170] Tiwari, A. K., et al. "Bromine functionalisation of diamond: An ab initio study," *Phys. Status Solidi A*, *209*:1703–1708 (2012).

[171] Twitchen, D. J., et al. "Electron paramagnetic resonance (EPR) and optical absorption studies of defects created in diamond by electron irradiation damage at 100 and 350 K," *Physica B*, *273–274*:628–631 (1999).

[172] Twitchen, D. J., et al. "Electron-paramagnetic-resonance measurements on the di-⟨001⟩-split interstitial center (R_1) in diamond," *Phys. Rev. B*, *54*(10):6988–6998 (1996).

[173] Ulbricht, R., et al. "Single substitutional nitrogen defects revealed as electron acceptor states in diamond using ultrafast spectroscopy," *Phys. Rev. B*, *84*:165202 (2011).

[174] Vanderbilt, D. and S. G. Louie. "Total energies of diamond (111)surface reconstructions by a linear combination of atomic orbitals method," *Phys. Rev. B*, *30*(10):6118 (1984).

[175] Vanderbilt, D. and S. G. Louie. "Total energy minimization for diamond (111) surfaces: Support for an undimerized π-bonded chain reconstruction," *Phys. Rev. B*, *29*(12):7099 (1984).

[176] von Barth, U. and L. Hedin. "A local exchange-correlation potential for the spin polarized case," *J. Phys. C*, *5*(13):1629–1642 (July 1972).

[177] Walker, J. "Otical and EPR spectroscopy of a tetragonal radiation-damage defect in diamond," *J. Phys. C*, *10*:3867 (1977).

[178] Wang, Y. M., et al. "Recent studies on diamond surfaces," *Diamond Relat. Mater.*, *9*:1582–1590 (2000).

[179] Weber, J. R., et al. "Quantum computing with defects," *Proc. Nat. Acad. Sci., USA*, *107*(19):8513–8518 (May 2010).

[180] Windischmann, H. "CVD diamond for thermal management." *Properties, growth and applications of diamond* Number 26 in EMIS Datareviews Series, edited by M. H. Nazaré and A. J. Neves, chapter C2.2, 410–415, London: INSPEC, Institute of Electrical Engineers, 2001.

[181] Wolf, D. "Should all Surfaces be Reconstructed?," *Phys. Rev. Lett.*, *70*(5):627 (1993).

[182] Wrachtrup, J. and F. Jelezko. "Processing quantum information in diamond," *J. Phys. Cond. Matter*, *18*:S807 (May 2006).

[183] Yang, W. L., et al. "Monochromatic Electron Photoemission from Diamondoid Monolayers," *Science*, *316* (2007).

[184] Ying, X., et al. "Ultra-thin freestanding diamond window for soft X-ray optics," *Diamond Relat. Mater.*, *12*(3):719–722 (March 2003).

[185] Zhang, Z., et al. "Surface structures and electron amenities of bare and hydrogenated diamond C(1OO) surfaces," *Phys. Rev. B*, *51*(8):5291 (1994).

[186] Zhou, X., et al. "Hydrogen-related defects in polycrystalline CVD diamond," *Phys. Rev. B*, *54*(11):7881–7890 (1996).

[187] Zvanut, M. E., et al. "Identification of phosphorus in diamond thin films using electron paramagnetic-resonance spectroscopy," *Appl. Phys. Lett.*, *65*(18):2287–2289 (October 1994).